



Energy &
Environmental
Science

**Designing CO₂ Reduction Electrode Materials by Morphology
and Interface Engineering**

Journal:	<i>Energy & Environmental Science</i>
Manuscript ID	EE-REV-03-2020-000900.R1
Article Type:	Review Article
Date Submitted by the Author:	07-May-2020
Complete List of Authors:	Pan, Fuping; University of Central Florida, NanoScience Technology Center Yang, Yang; University of Central Florida, NanoScience Technology Center

SCHOLARONE™
Manuscripts

Designing CO₂ Reduction Electrode Materials by Morphology and Interface Engineering

Fuping Pan^a, Yang Yang^{a,b,c*}

^a NanoScience Technology Center, University of Central Florida, Orlando, Florida 32816, United States

^b Department of Materials Science and Engineering, University of Central Florida, Orlando, Florida 32816, United States

^c Energy Conversion and Propulsion Cluster, University of Central Florida, Orlando, Florida 32816, United States

* Corresponding Author E-mail: Yang.Yang@ucf.edu

Abstract

Electrochemical reduction of CO₂ into value-added fuels and chemicals driven by renewable energy presents a potentially sustainable route to mitigate CO₂ emissions and alleviate the dependence on fossil fuels. While tailoring the electronic structure of active components to modulate their intrinsic reactivity could tune CO₂ reduction reaction (CO₂RR), their use is limited by the linear scaling relation of intermediates. Due to the high susceptibility of CO₂RR to local CO₂ concentration/pH and mass transportation of CO₂/intermediates/products near the gas-solid-liquid three-phase interface, engineering catalysts' morphological and interfacial properties holds great promises to regulate CO₂RR, which are irrelevant with linear scaling relation and possess high resistance to the harsh reaction condition. Herein, we provide a comprehensive overview of recent advances in tuning CO₂ reduction electrocatalysis via morphology and interface engineering. The fundamentals of CO₂RR and design principles for electrode materials are presented firstly. Then, approaches to build the efficient three-phase interface, tune surface wettability, and design favorable morphology are summarized; the relationship between properties of engineered catalysts and their CO₂RR performance is highlighted to reveal activity-determining parameters and underlying catalytic mechanisms. Finally, the challenges and opportunities are proposed to suggest the future design of advanced CO₂RR electrode materials.

Keywords

CO₂ reduction; electrode materials; morphology, interface, wettability

Contents

1. Introduction	4
2. Fundamentals and challenges	11
2.1 Activity descriptors	11
2.2 Thermodynamics of CO ₂ reduction	11
2.3 Kinetics of CO ₂ reduction	13
2.4 Large overpotential	16
2.5 Competition with hydrogen evolution	18
2.6 Produce C ₂₊ products	18
2.7 Product separation	19
2.8 Linear scaling relation	20
3. Classification of catalysts	22
4. Catalysts design principles	30
4.1 Local CO ₂ concentration	31
4.2 Interfacial alkalinity	33
4.3 Management of mass transportation	34
4.4 Density of active sites	35
4.5 Enhancement in kinetics	37
5. Approaches to engineer electrodes and their performance	38
5.1 Constructing favorable three-phase interface	39
5.1.1 Interface under neutral media	40
5.1.2 Interface under alkaline electrolyte	42
5.1.3 Interface under electrolyte-free condition	47

5.2 Surface wettability engineering	52
5.3 Morphology-induced activity tuning	59
5.3.1 Nanoneedles	60
5.3.2 Nanocavity.....	63
5.3.3 Mesopores	65
5.3.4 Hierarchical porous nanocage	71
5.3.5 Crystalline porous frameworks	73
5.3.6 Porous thin film	77
5.3.7 Other morphology	82
6. Summary and perspectives.....	84

1. Introduction

Since the 19th century, a tremendous amount of fossil fuels such as coal, oil, and natural gas have been consumed as the main energy source to sustain the rapid economic development and population growth. Consequently, the level of as-emitted carbon dioxide (CO₂) in the atmosphere increases drastically, which may reach 570 ppm by 2100 and has raised big concerns on numerous environmental issues due to their potential contributions to the global warming.^{1,2} While previous efforts to reduce atmospheric CO₂ concentration mainly focused on CO₂ capture and storage (CCS),^{3,4} current attention has moved on CO₂ capture and utilization (CCU) due to its merits of effectiveness and sustainability.⁵⁻¹⁰ Among various proposed routes for CO₂ conversion, the electrochemical transformation of CO₂ into value-added chemicals and fuels holds the greatest promise because it can be carried out at the mild ambient condition and could directly store electricity and CO₂ into transportable liquid fuels in a relatively high rate.^{1,11-13} Further, CO₂ from CO₂-generated fuels-powered electronic vehicles could be recaptured and recycled, resulting in an effective carbon cycle. As the growing abundance of renewable electricity from solar, wind, and geothermal energy and the decrease in its price,^{14,15} renewable energy-powered CO₂ electrolysis technology shows the closest gap to the large-scale commercialization.

A full CO₂ electrolysis setup includes a cathode, an anode, an electrolyte, and a membrane, similar to the overall water splitting.⁷ The water oxidization, namely oxygen evolution reaction (OER), occurs at the anode, producing the gaseous O₂, electron, and proton. The electron travels to the cathode through the external circuit, and the proton passes through the membrane and electrolyte to the cathode under the electric field. At the cathode, CO₂ reduction reaction (CO₂RR)

takes place at the gas-solid-liquid three-phase interface, where CO_2 combines with electrons and protons generating products (**Figure 1A**). The separation of OER and CO_2RR by the membrane is to prevent the cathodic CO_2RR -generated products from being re-oxidized at the anode and mixture of O_2 with CO_2RR -products. CO_2RR electrocatalysis is a multi-step process involving multiple proton-coupled electron transfer (PCET) processes, which is at the cornerstone of CO_2 electro-conversion technology because of the stable nature of the linear CO_2 molecule. This situation necessarily requires the use of CO_2RR catalysts (cathode) to activate CO_2 and implement the CO_2 reduction process. Theoretically, CO_2RR could generate a variety of products, such as C_1 (carbon monoxide, formic acid, methane, methanol, etc.), C_2 (ethylene, ethanol, acetate, and ethylene glycol), and C_{2+} products (propanol and propionaldehyde).^{16, 17} The distribution of products and conversion efficiency depend highly on cathodic electrode materials. It is ideally expected that CO_2RR electrode materials could produce a single targeted product with 100% Faradaic efficiency and at a low overpotential with a large current density and long-term durability (**Figure 1B**). Besides enhanced performance, catalysts should be made of earth-abundant cost-effective elements to enable the large-scale application.

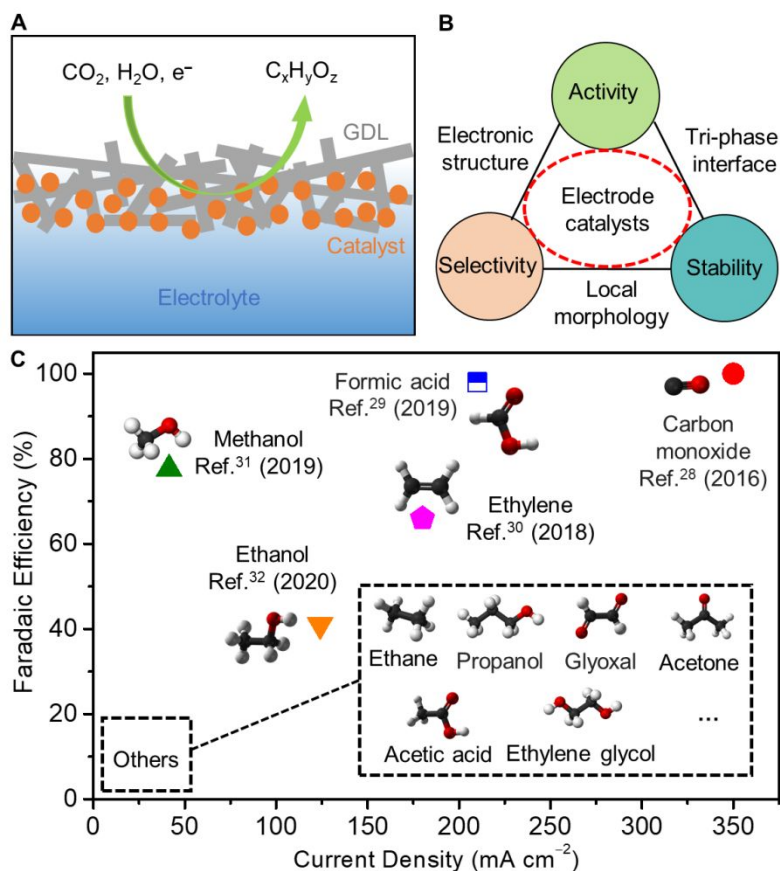


Figure 1. (A) Schematic of homogeneous CO₂ electroreduction at the gas (CO₂)-solid (catalyst)-liquid (aqueous electrolyte) three-phase interface. Reproduced with permission from Ref.⁷. Copyright © 2019 Springer Nature Group. (B) Requirements for a CO₂RR catalyst including activity, selectivity, and stability, which are collectively governed by catalysts' electronic structure, local morphology, and three-phase interface. (C) FEs and partial current densities achieved for different products from CO₂ reduction over state-of-the-art catalysts. The data reported in Ref.²⁸,^{29,30} were collected in flow cells with a three-electrode configuration; The data reported in Ref.³¹ were collected in H-type cell with a three-electrode configuration. The data reported in Ref.³² were collected in fuel cells with a two-electrode configuration.

A large variety of electrocatalytic materials have been developed to produce various compounds from CO₂RR. For example, Pd, Bi, Sn are active for formic acid production,^{7, 18-20} Au, Au, Zn, and single-atom Fe/Ni for CO generation,²¹⁻²⁴ Cu and Cu-based composites for C₂ and C₂₊ hydrocarbons and oxygenates.^{16, 25-27} The highest FE and corresponding current density achieved so far were summarized in **Figure 1C**. Reducing CO₂ to CO and HCOOH reached partial current densities of 350/210 mA cm⁻² and Faradaic efficiencies of 99%/98% on the Ag layer coated on carbon nanotubes²⁸ and defected bismuth oxide nanotubes²⁹ at -0.8/-0.58 V vs. RHE in alkaline flow cells, respectively. For C₂H₄ generation, a Faradaic efficiency of 66% and a partial current density of 180 mA cm⁻² was achieved on a modified Cu electrode at -0.55 V vs. RHE in the alkaline flow cell.³⁰ The CO₂RR performance to form CH₃OH and C₂H₅OH is relatively poor, showing Faradaic efficiencies of 78%/41% and partial current density of 42/124 mA cm⁻² on copper selenide at -0.28 V vs. RHE in the H-type cell³¹ and 5,10,15,20-tetraphenyl-21H,23H-porphine iron(iii) chloride (FeTPP[Cl])-Cu hybrid catalysts (FeTPP[Cl]-Cu) in the fuel cell at 3 V,³² respectively. The reported stability of these catalysts is less than 100 h and energy efficiencies are below 80% (without consideration of overpotentials at the anodic OER). Reducing CO₂ to other economically desirable high-order products faces considerably big challenges due to the lack of suitable catalysts. Techno-economic modeling shows that a practically feasible catalyst should be able to produce a single product with an FE > 90%, a partial current density > 200 mA cm⁻², and stability > 1000 h at a potential more positive than -0.6 V.^{33, 34} Obviously, it is still far away for the current systems to simultaneously meet these thresholds for the practical application.

With the extensive investigation of CO₂RR mechanisms, it turns out that CO₂ reduction is highly governed by electrode materials' electronic structure, local morphology, interfacial properties, and reaction conditions (**Figure 1B**).^{7, 35} Among these factors, engineering electronic structure of active sites has been extensively studied to tune CO₂RR. The basic principle is that heterogeneous CO₂RR typically involves the adsorption of intermediates on catalysts' surface.³⁶ Thereby, modulating atomic and/or nano scale electronic properties of catalysts, such as defecting,^{37, 38} doping,³⁹⁻⁴¹ alloying,^{25, 42} straining,^{43, 44} faceting,¹²³ grain boundary,¹⁸⁰ atom locations (edge, corner, terrace),^{181, 45, 46} and surface distortion,⁴⁷⁻⁴⁹ could modulate binding strength between intermediates and active sites, in turn the adsorption/desorption of intermediates, and finally the distribution and generation rate of products. Reaction conditions, such as temperature and pressure, can also govern CO₂ reduction via adjusting CO₂ concentration, solution pH, and reduction kinetics, etc.,⁵⁰ which are more relevant to technological manipulation. A succinct overview of both electronic properties engineering and reaction condition selection have been summarized in the recently published Perspectives and Reviews.^{5, 9, 11, 37, 51-54}

While modifying the electronic structure to alter intrinsic reactivity has been demonstrated, there exist big challenges to sustain catalytic stability because the chemical components of catalysts tend to be changed in the harsh reaction condition.⁵⁵ For example, Cu-based catalysts with positively charged species (Cu^{δ+}) have been demonstrated to possess higher catalytic selectivity for the production of C₂H₄ than metallic Cu. However, the Cu^{δ+} is prone to be reduced to Cu⁰ under negative applied potentials in the real condition, resulting in the activity deactivation.^{56, 57} More challengingly, linear scaling relation,^{58, 59} which states the linearly related

adsorption energies of various CO₂RR-involved intermediates on catalysts' surfaces, limits the design of specifically active catalysts because tuning the adsorption of one intermediate will similarly affect that of others. This makes that the Sabatier design principle is hard to be realized in the multi-step CO₂RR process, which presents that binding energy of the key intermediate should be neither too strong nor too weak to reduce the activation barriers and to achieve a high generation rate of the targeted product.^{20, 60-62}

Besides the aforementioned electronic structure and reaction condition, recent findings demonstrated that CO₂RR is very sensitive to the local CO₂ concentration and electrolyte pH at the electrode-electrolyte interface and the mass transportation of CO₂RR-involved species.^{30, 63-65} Modifying the electrode catalysts' morphology and interface properties could tune product selectivity, overpotential, current density, productivity, charge transfer resistance, mass transportation, reaction kinetics, and stability, despite the atomic and/or nano level electronic structure on various morphology remains to be the same. Different from engineering electronic properties of active components, constructing the suitable morphology and interface is not limited by linear scaling relation, which appears to be promising strategies to achieve efficient CO₂ electro-conversion. However, there is a lack of in-depth overviews on this emerging topic to provide general principles for future design. To this end, we particularly set our focus on reviewing recent achievements to explore the relationship between morphology and interface of electrode materials and their electrocatalytic CO₂RR performance. We first presented fundamentals and challenges in the field of CO₂RR, followed by providing principle interpretation on how the morphological and interfacial properties could govern CO₂RR, including local CO₂ concentration,

interfacial alkalinity, management of mass transportation, the density of active sites, and enhancement in kinetics. Further, we reviewed recently developed approaches for constructing favorable three-phase interfaces, engineering surface wettability, and fabricating activity-dependent morphology. The relationship between engineered catalysts and their catalytic performance was also comprehensively discussed to provide an insightful understanding of catalytic mechanisms. Finally, we pointed out challenges and provided suggestions to the future design of advanced CO₂RR electrode materials. We expect that this Review could open up new opportunities to address challenges faced by CO₂ reduction and other energy-related electrocatalysis.

2. Fundamentals and challenges

CO₂RR takes place at a complex three-phase interface of solid catalyst-liquid electrolyte-gaseous CO₂. As suggested by both theoretical simulation and experimental investigation,^{54, 66-68} the electrocatalytic CO₂RR mainly includes CO₂ activation, surface reaction, and product desorption processes. In this section, we will introduce the fundamentals and challenges of CO₂RR.

2.1 Activity descriptors

To evaluate the performance of electrocatalysts and catalytic systems for CO₂RR, several fundamental parameters need to be considered, mainly including Faradaic efficiency (FE, the product selectivity of targeted products), overpotential (η , the potential difference between the thermodynamic standard potential and the experimental potential), energy efficiency (EE, the ratio between the output energy from CO₂RR and the input energy), current density (J, the production

rate), and stability (capability for long-term use). The definition of these parameters is described in detail in the Supplementary Information (Note 1). It is worth mentioning that all these descriptors should be considered jointly to assess the overall performance of an electrocatalyst. Ideally, a high-performance catalyst should be engineered to have enhanced FE, J, EE, and stability while working at a low η .

2.2 Thermodynamics of CO₂ reduction

CO₂ is a fully oxidized and thermodynamically stable molecule with linear geometry. The dissociation energy of the C=O bond in CO₂ is about 750 kJ mol⁻¹, indicating large activation energy and huge energy input for direct C=O bond dissociation.⁶⁹⁻⁷¹ To facilitate CO₂ reduction, activation has been considered to be the first step, in which the linear CO₂ structure will be transformed into bent configurations to weaken the C=O bond by forming chemical bonds between CO₂ and catalytic sites on the catalyst's surface. It is generally proposed that there are four types of mechanisms in CO₂ activation (labeled as ①, ②, ③, ④ in **Figure 2**).

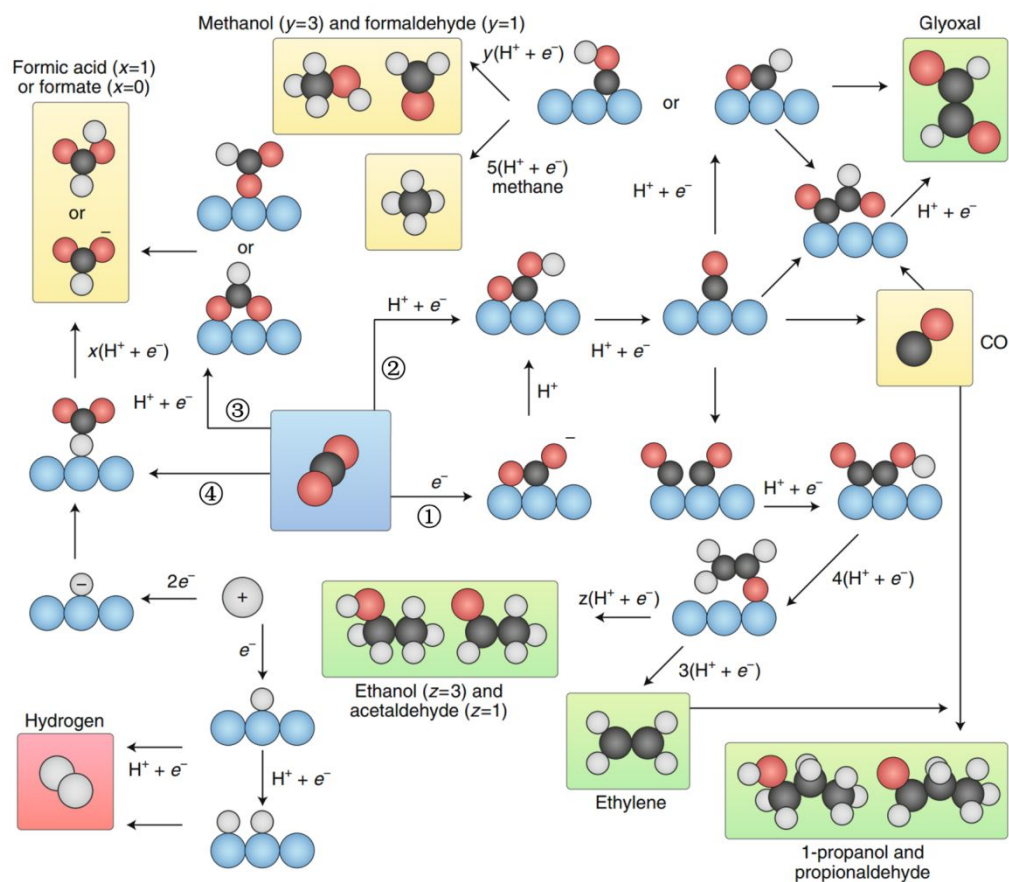


Figure 2. Summary of CO₂RR reaction pathways towards different products. Black, red, white, blue spheres refer to carbon, oxygen, hydrogen, and catalyst, respectively. Adapted with permission from Ref.³⁵. Copyright 2018 Nature Publishing Group.

In mechanism ①, CO₂ is transformed into an anionic radical with one electron ($* + \text{CO}_2 + e^- \rightarrow * \text{CO}_2^{\cdot-}$),⁷²⁻⁷⁴ which requires a negative redox potential of -1.9 V versus normal hydrogen electrode (NHE). It is generally considered that the stabilization of adsorbed CO₂^{•-} by electron coupling between CO₂^{•-} and right electrocatalysts can initiate CO₂RR at many positive potentials, resulting in low overpotentials experimentally.^{35, 75-77} Besides selecting suitable catalysts, previous findings also demonstrate that employing proper additives in the electrolytes can also lower the

initial reduction barrier, in which the additives function as co-catalysts to stabilize the $*\text{CO}_2^{\cdot-}$ on the catalyst surface by forming a complexation interaction, resulting in the decrease in the free energy of the $*\text{CO}_2^{\cdot-}$ formation (**Figure S1**).^{78, 79} For instance, Rosen et al. found that adding 18 mol% of 1-ethyl-3-methylimidazolium tetrafluoroborate (EMIM-BF₄) in aqueous solution results in the generation of CO at an applied potential of 1.5 V in the two-electrode cell, about 0.6 V smaller than that observed on the same system without adding EMIM-BF₄.

Unlike mechanism ① which forms high-energy $*\text{CO}_2^{\cdot-}$ radical, the PCET process has been widely considered to reduce the activation energy, leading to the occurrence of CO₂RR at low overpotentials.⁸⁰ There are two pathways for the PCET route: mechanism ② and ③ in **Figure 2**, in which CO₂ is transformed into C-bound $*\text{COOH}$ ($* + \text{CO}_2 + \text{H}^+ + \text{e}^- \rightarrow *\text{COOH}$) and O-bound $*\text{OCHO}$ intermediates ($* + \text{CO}_2 + \text{H}^+ + \text{e}^- \rightarrow *\text{OCHO}$),^{66, 81, 82} respectively. These mechanisms have been widely employed in DFT calculation to explain experimental results on various catalysts. In mechanism ④, it is proposed that an anionic hydride species is formed via $* + \text{H}^+ + 2\text{e}^- \rightarrow *\text{H}^-$, which attacks CO₂ generating $*\text{OCHO}$ intermediate.⁸³⁻⁸⁶

2.3 Kinetics of CO₂ reduction

Electrode kinetics correlate directly to the selectivity and generation rates of final products. To accurately describe the electrode kinetics, the plot of current as a function of potential is generally used. **Figure S2** shows the behavior of Butler–Volmer’s model of electrode kinetics.⁸⁷ It can be seen that, at the low overpotential range, the cathodic current (i_c) increases with increasing overpotentials, suggesting that the reaction is limited by the heterogeneous kinetics. However, at

the large positive overpotentials, the i_c reaches a plateau, namely limiting-current ($i_{l,c}$), which is independent with the overpotential but limited by mass transfer. Therefore, analyzing the nature of the limiting step could help to understand the actual relationship between the current and the overpotential. In the past few decades, extensive efforts have been made to explore the fundamental processes and influencing factors governing the kinetics of CO₂ reduction, which are discussed below.

CO₂RR undergoes multiple pathways. Upon CO₂ activation, subsequent PCET process initiates a series of surface reactions involving the cleavage of C–O bond, the coupling of C–C bond, and the formation of C–H bonds, which eventually lead to the generation of different products.⁸⁸ The *OCHO, formed through mechanism ③, is considered to be the intermediate for forming formic acid (**Figure 2**), which adsorbs on catalysts surface via bonding between O atom of *OCHO and catalysts without the breakage of the C=O bond of CO₂. By contrast, *COOH is the intermediate to generate adsorbed *CO with the cleavage of C=O.²⁰ The *CO can either desorb from catalyst surface to generate gaseous CO as the final product or couple to form high-order intermediates for C₂ products through the *CO dimerization and subsequent PCET processes. Also, the formation of *COH intermediate by *CO hydrogenation yields CH₄ or CH₃OH,^{89, 90} and the coupling between C₂H₄ and CO yield C₃ product.³⁵ Note that the desorbed gaseous CO could serve as reactant being further reduced to various hydrocarbons and oxygenates via CO reduction reaction (CORR).⁹¹⁻⁹³ However, none of these processes have been fully confirmed experimentally due to the difficulty in capturing intermediates. The adsorption/desorption of intermediates in any

step could considerably influence the overall performance, of which the rate-limiting step is still not well established.

Moreover, CO₂RR involves multiple electron transfer processes, such as 2 e⁻ for CO, 6 e⁻ for CH₃OH, 8 e⁻ for CH₄, and 12 e⁻ for C₂H₄. Thereby, the electron transfer affects not only the CO₂ reduction rate but also the selectivity of products. Electrochemically, charge transfer resistance (R_{ct}) can be used to estimate the capability of electron transmission from catalyst surface to the reactant as well as intermediates. A lower R_{ct} means a faster electron transfer process, which can be determined by electrochemical impedance spectroscopy (EIS). Asadi et al.⁹⁴ demonstrated that nanoflakes could enable much faster electron transfer than bulk materials, delivering a R_{ct} of ~180 ohms at an overpotential of 150 mV on tungsten diselenide (WS₂) nanoflakes in CO₂RR, much smaller than ~420 ohms of bulk MoS₂ plate. The enhanced electron transmission contributes to a larger current density on WS₂ nanoflakes as compared to MoS₂ plate.

Mass transportation is another important factor influencing CO₂RR kinetics. CO₂ reduction involves the transportation of many species, such as the dissolution of CO₂ into solution, the approach of CO₂ from the bulk electrolyte to the boundary layer and the electrode surface, the transportation of intermediates in the heterogeneous electrocatalytic interface, and the movement of the product away from the reaction interface into bulk solution (**Figure S3**).^{95, 96} Reported studies show that CO₂RR on polycrystalline Ag exhibited a Tafel slope of 132 mV dec⁻¹ at low overpotentials,⁹⁷ suggesting that the rate-determining step is the initial electron transfer to CO₂ forming a surface adsorbed *COOH intermediate. This indicates that the transport process of CO₂ does not interfere with the supply of CO₂ due to the low consumption rate. By contrast, when CO₂

reduction was conducted on curved Ag surface, which has enhanced intrinsic capability for CO₂RR, a smaller Tafel slope of 58 mV dec⁻¹ was observed, indicating that the rate-limiting step probably relates to the issues of the diffusion of CO₂ and products out of/into the catalyst nanopores.^{97, 98}

Besides the above-described factors, the kinetics of CO₂ reduction can also be governed by electrolyte, temperature, and pressure, which are presented in the Supplementary Information (Note 2). With these analyses, it can be inferred that CO₂RR is a very complex process with numerous inherent drawbacks. Such a situation arises a few challenges in CO₂RR electrocatalysis, which will be given in detail next.

2.4 Large overpotential

Theoretically, CO₂ reduction has thermodynamic equilibrium potentials toward various products near 0 V vs. RHE (**Table 1**). However, more negative potentials are commonly applied to initiate CO₂RR and achieve high current density due to inert thermodynamics and sluggish kinetics. More challengingly, CO₂RR is highly dependent on the applied potential, and products' FEs follow the tendency of increasing, reaching the maximum value, and then decreasing when sweeping potential negatively. Thereby, the actual potentials needed to drive CO₂RR at maximum product selectivity are considerably more negative than the equilibrium ones. For example, the state-of-the-art Au and Ag catalysts showed overpotentials more than 250 mV to reach FEs larger than 90% for CO production;^{98, 99} Cu-based catalysts exhibited overpotentials larger than 600 mV to achieve the highest FE for ethylene and alcohol production.^{25, 30, 31} The large overpotential implies supernumerary energy input beyond thermodynamically determined energy, thus resulting

in a low energy conversion efficiency.^{35, 88}

Table 1. Electrochemical reactions with equilibrium potentials.⁵¹

Reactions	E^0 (V vs. RHE)
$2\text{H}_2\text{O} \rightarrow \text{O}_2 + 4\text{H}^+ + 4\text{e}^-$	1.23
$2\text{H}^+ + 2\text{e}^- \rightarrow \text{H}_2$	0
$\text{CO}_2 + 2\text{H}^+ + 2\text{e}^- \rightarrow \text{CO} + \text{H}_2\text{O}$	-0.11
$\text{CO}_2 + 2\text{H}^+ + 2\text{e}^- \rightarrow \text{HCOOH}$	-0.21
$\text{CO}_2 + 4\text{H}^+ + 4\text{e}^- \rightarrow \text{HCHO} + \text{H}_2\text{O}$	-0.1
$\text{CO}_2 + 6\text{H}^+ + 6\text{e}^- \rightarrow \text{CH}_3\text{OH} + \text{H}_2\text{O}$	-0.03
$\text{CO}_2 + 8\text{H}^+ + 8\text{e}^- \rightarrow \text{CH}_4 + 2\text{H}_2\text{O}$	-0.17
$2\text{CO}_2 + 8\text{H}^+ + 8\text{e}^- \rightarrow \text{CH}_3\text{COOH} + 2\text{H}_2\text{O}$	-0.26
$2\text{CO}_2 + 10\text{H}^+ + 10\text{e}^- \rightarrow \text{CH}_3\text{CHO} + 3\text{H}_2\text{O}$	0.06
$2\text{CO}_2 + 12\text{H}^+ + 12\text{e}^- \rightarrow \text{C}_2\text{H}_4 + 4\text{H}_2\text{O}$	0.07
$2\text{CO}_2 + 12\text{H}^+ + 12\text{e}^- \rightarrow \text{C}_2\text{H}_5\text{OH} + 3\text{H}_2\text{O}$	0.09
$2\text{CO}_2 + 14\text{H}^+ + 14\text{e}^- \rightarrow \text{C}_2\text{H}_6 + 4\text{H}_2\text{O}$	0.14
$3\text{CO}_2 + 18\text{H}^+ + 18\text{e}^- \rightarrow \text{C}_3\text{H}_7\text{OH} + 5\text{H}_2\text{O}$	0.09

2.5 Competition with hydrogen evolution

In CO_2RR , the proton is necessary to serve as a reductant and source for both reduction and hydrogenation processes, but it can be also readily reduced by themselves generating hydrogen, so-called hydrogen evolution reaction (HER).^{7, 100} Since equilibrium potentials of CO_2RR are close

to that of HER (**Table 1**), HER becomes a parasitic reaction competing with CO₂RR, which potentially lowers current efficiency for CO₂RR.^{88, 101-103} In HER, the first step is the reduction of a proton on catalyst surface to generate adsorbed *H ($* + \text{H}^+ + \text{e}^- \rightarrow * \text{H}$, Volmer step).^{100, 104} CO₂RR and HER share the same catalytic sites (eg., metal atoms), and the binding energy between metal sites and *H/*C/*O determines the catalyst's capability to suppress HER. If a catalytic site binds *H stronger than *C (or *O), the adsorption of *H will be promoted while the adsorption of *COOH (or *OCHO) will be suppressed, favoring HER instead of CO₂RR. Thereby, a suitable CO₂RR catalyst should have a properly strong binding strength with *C (or *O) but a weak binding strength with *H. Single-atomic unsaturated Fe/Ni^{102, 105-107} and polycrystalline Au^{108, 109} show weak adsorption with *H and thus enhanced selectivity to CO₂RR.

2.6 Produce C₂₊ products

CO₂RR can produce a broad variety of products. Reducing CO₂ with two electrons to first-order products is the simplest pathway,²⁰ and the highly active and selective generation of CO and HCOOH with FEs more than 98% and partial current more than 200 mA cm⁻² has been achieved (**Figure 1C**). Compared to C₁ product, C₂₊ products are more valuable because their larger energy density, market size, and contributions to reduce net carbon emission.^{1, 2} However, the current reported performance of C₂₊ products is far away from the practical application (**Figure 1C**). The main reason is that the CO₂-to-C₂₊ process involves multiple PCET steps and elemental pathways. For example, synthesizing C₂H₄, C₂H₅OH, C₃H₇OH consumes 12, 12, and 18 electrons and protons, making the overall process very complex and hard to be finely manipulated. Also, reducing CO₂

to C_{2+} products needs not only the formation of adsorbed $*CO$ but also C–C coupling ($*CO$ dimerization) and hydrogenation,³⁵ and there is a lack of understanding on the elementary steps and catalytic mechanisms. Designing a catalyst that can meet all these requirements is very challenging. So far, only copper,⁵¹ N-functionalized carbon,¹¹⁰ NiP,¹¹¹ and MoS₂¹¹² were demonstrated to be able to generate C_{2+} products, but with unsatisfactory performance, especially for C_{3+} products. For instance, Cu mesh¹¹³ and edge-deficient MoS₂¹¹² were found to show low FEs of 13% and 3.5% for isopropyl alcohol generation, respectively.

2.7 Product separation

In CO₂RR, gaseous CO₂ is hard to be fully converted, and a broad distribution of products commonly co-exist. Such a situation results in a mixture of gaseous products with CO₂ in the gas phase and the dissolution of liquid products in the electrolyte. Therefore, the separation of products is generally imperative and critical for down-stream utilization. For the gas-phase product separation, membrane (organic, ceramics, and metals)-based separation technology, which selectively permits the passage of wanted gas while rejecting the unwanted species, could finally solve this problem as it is considered to be less energy-intensive than traditional pressure-enabled separation technologies.¹¹⁴ However, membrane-enabled separation of high-value species from CO₂, such as C₂H₄/C₂H₆/C₃H₆/C₃H₈, is still very challenging and at the early stage of research.¹¹⁵ Hybrid materials, such as metal-organic frameworks (MOFs), are considered as promising membranes due to their tunable structure and composition.¹¹⁶ Regarding the liquid-phase products, the dissolution of products in the aqueous electrolyte leads to the formation of salt (such as formate

instead of HCOOH) and the low concentration. The distillation technology has been widely applied to separate liquid-phase products from solution based on the difference in the boiling point, which achieves phase separation through temperature modulation. However, distillation requires high heat inputs and cannot fully separate the species with close boiling points. Reactor engineering could be a bright method to produce high-purity liquid products with variable concentration for direct use (such as catholyte-free electrolyzer) which will be discussed in section 5.1.3.

2.8 Linear scaling relation

An ideal catalyst should have free-energy barriers for all elemental pathways close to zero according to the Sabatier principle.^{20, 60-62} This requires that catalyst surface should bind with intermediates neither too strong nor too weak. However, this is hard to be realized because the adsorption energy of one intermediate scales linearly with that of the subsequent intermediates caused by the same adsorption site, namely linear scaling relation.^{58, 59} It is worth noting that heterogeneous CO₂RR electrocatalysis is different from the biomimetic catalysis. The latter is a predominantly homogeneous process and the catalytic process is driven by the reaction between coenzyme and reactant,¹¹⁷ in which the overall process is not governed by the adsorption of intermediates and thus the linear scaling relation is commonly not evident.

Nørskov et al.^{7, 59} calculated adsorption energy of *CO, *COH, *CHOH, and *CHO, clearly showing a linear relation on Ag, Au, Cu, Pd, Pt surface (**Figure 3**). The linear scaling relation cannot be even avoided in the design of catalysts for CO generation, which requires a catalyst to

strongly bind $^*\text{COOH}$ to facilitate the CO_2 activation. However, such a case will lead to the strong adsorption of $^*\text{CO}$ too, which ultimately results in the poor CO desorption and thus low production rate. In other words, CO_2 activation and CO desorption are non-optimal unless scaling relation can be broken. This yields a volcano-shaped plot between the current density and adsorption energy of key intermediates.²⁰ In the reduction of CO_2 to C_{2+} products, the limitation of linear scaling relation becomes more protruding because more intermediates are involved and their adsorption energies scale linearly with each other.

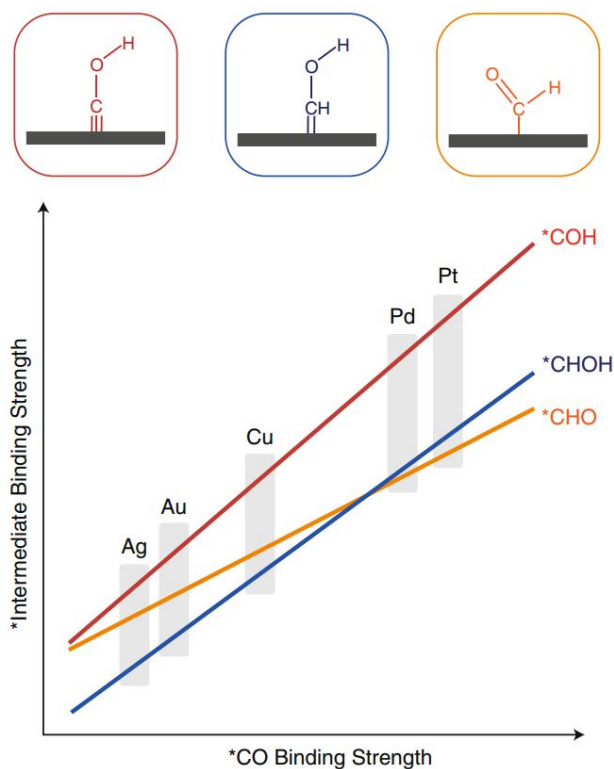


Figure 3. Calculated adsorption energies for $^*\text{COH}$ (red), $^*\text{CHOH}$ (blue) and $^*\text{CHO}$ (orange) as a function of the adsorption energy of $^*\text{CO}$ for Pt, Pd, Cu, Au, and Ag. Adapted with permission from Ref.⁷. Copyright 2019 Springer Nature.

3. Classification of catalysts

According to the Sabatier principle, a good catalyst should have an optimal binding strength with the key reaction intermediates and surface sites of catalysts. Therefore, the electronic structure of materials strongly determines their intrinsic reactivity toward CO₂RR as the binding energy of key intermediates involved in CO₂RR, such as *H, *OCHO, *COOH, *CO, *CHO, is mainly governed by the surface electronic properties of catalysts, which has been widely used as a key descriptor to classify catalysts based on the categories of products. Theoretically, the adsorption of these intermediates species on the different metal surfaces has been extensively investigated through DFT calculation to distinguish catalysts,^{20, 62, 118} and the theory-guided tendency are mostly in good agreement with experimental results. In this section, we will introduce both typically well-known catalysts and state-of-the-art catalysts for some common products from CO₂RR, and corresponding advantages and disadvantages will be discussed as well.

1) CO. The carbon-bound *COOH and *CO are key intermediates for the reduction of CO₂ to CO, during which the formation of *COOH is the potential-limiting step and the desorption of *CO governs the current density. Noble metals Ag and Au are the most active catalysts for CO generation due to their optimal binding strength with *COOH and weak adsorption with *CO, allowing facile CO₂ activation and CO desorption (**Figure 4A, B**).^{21, 28} They achieved maximum FEs larger than 95% and high EE above 80% at small overpotentials (< 300 mV, **Table 2**). However, the inherent drawbacks of prohibitive cost and scarcity limit the large-scale application. Metallic Fe, Ni, Co are not good catalysts for CO₂RR due to their strong binding with *H, thus favoring proton reduction to hydrogen. Zn and ZnO also show high activity for CO with large

current density but commonly need large overpotentials owing to the poor adsorption of $^*\text{COOH}$.⁶⁶

¹¹⁹ Besides, atomically dispersed nitrogen-coordinated transition metal (Fe, Co, Ni) supported on carbons (M-N/C) has attracted numerous attentions by advantage of the rich reserve, chemical stability, and good conductivity.^{102, 103, 120, 121} Among them, Ni-N/C commonly shows higher current density but need larger overpotentials as compared to Fe-N/C and Co-N/C. The catalytic properties of active M-N sites are highly sensitive to the coordinated N number and carbon supports architecture, which has not been fully understood and needs further investigation. A report shows that highly active Fe^{3+} of Fe-N/C can be reduced to the less active Fe^{2+} when the applied potential is negative than -0.5 V vs. RHE,²⁴ which challenges the electrochemical stability.

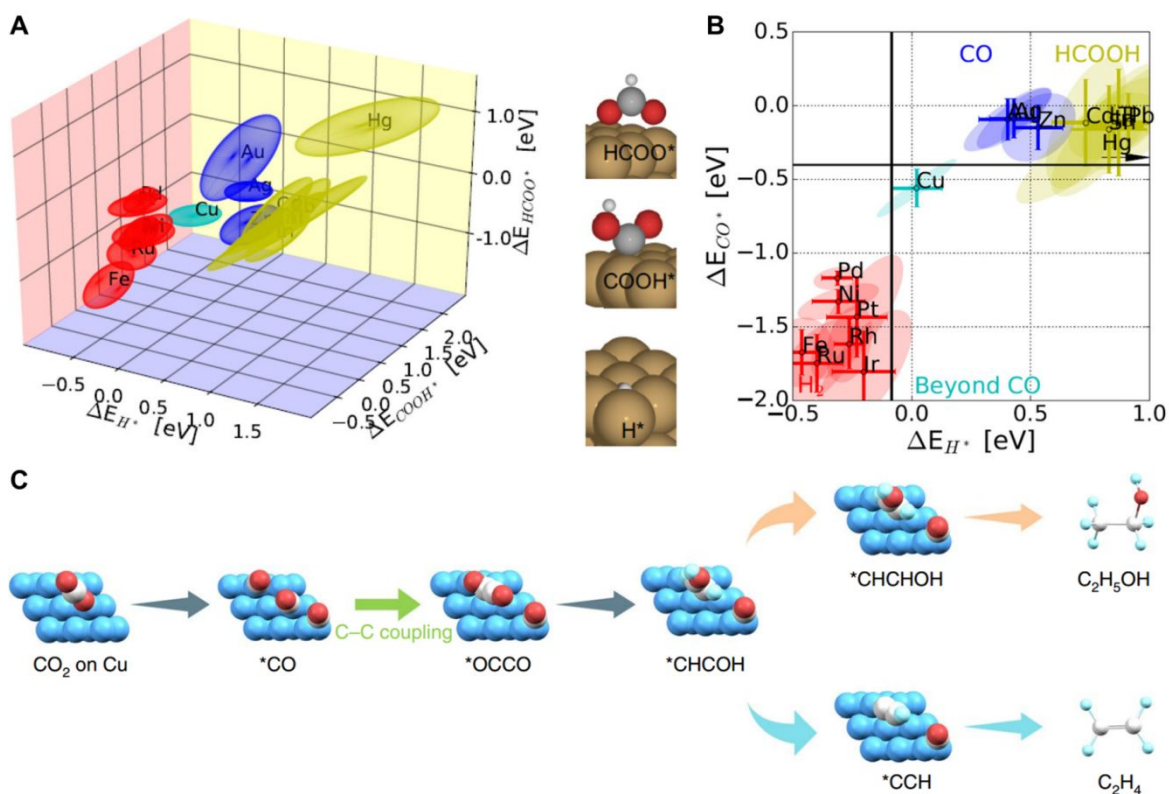


Figure 4. (A) Binding-energy plots between $^*\text{H}$, $^*\text{OCHO}$ (HCOO^*), and $^*\text{COOH}$, (B) The binding energies of the intermediates $^*\text{CO}$ and $^*\text{H}$ on the various metal surface. Adapted with permission

from Ref.⁶². Copyright 2017 Wiley. (C) Key reaction pathways for CO₂RR to C₂H₄ and C₂H₅OH. Adapted with permission from Ref.³². Copyright 2019 Springer Nature. Blue (or brown), grey, red, and light blue (or white) represent to Cu, C, O, and H, respectively.

2) HCOOH. The oxygen-bound *OCHO is considered to be the key intermediate for HCOOH generation, and metallic Sn with near-optimal binding strength with *OCHO is highly selective for HCOOH (**Figure 4A, B**). This observation is in good agreement with the findings obtained by Feaster et al.,²⁰ where the volcano plot of HCOOH partial current densities at -0.9 V vs RHE versus *OCHO binding energies was observed. Au, Ag, Pt, and Cu were found to have weak binding with *OCHO, while Ni and Zn bind *OCHO too strong to produce HCOOH. Similarly, S-doped Sn,¹²² CuSn₃ alloy,¹²³ metallic Bi,¹⁹ defective Bi₂O₃ nanotubes,²⁹ ultrathin Co,¹²⁴ atomic Co₃O₄ layers¹²⁵ with stabilized *OCHO show enhanced activity for HCOOH production with higher FEs, smaller overpotentials, and larger EEs as compared to Sn (**Table 2**). Particularly, a high FE of 98%, a current density of 210 mA cm⁻², and an EE of 78% has been reported on defective Bi₂O₃ nanotubes,²⁹ whereas the performance of other catalysts still needs to be improved.

3) CH₃OH. For CH₃OH generation, a key step is the transformation of C-bound *CO to C-bound *CHO intermediate via the PCET-assisted hydrogenation process (*CO + H⁺ + e⁻ → *CHO).³⁵ Cu₂O was found to show a FE of 47.5% at a negative potential of -1.6 V, implying a large overpotential of around 1.6 V and a poor EE of 21% given the standard equilibrium potential of -0.03 V.¹²⁶ Copper selenide³¹ and FeP Nanoarray¹²⁷ possess unique electronic properties to facilitate the formation of *CHO with decreased energy barriers, showing high FEs above 75%

and EE above 60%. Especially for FeP, it exhibits the highest FE of 80% and EE of 69% at a low overpotential of 197 mV, despite the current density remains low ($< 0.96 \text{ mA cm}^{-2}$). In addition, Pd nanoparticles supported on SnO_2 nanosheets⁶ and isolated CoPc anchored on CNT¹²⁸ also exhibit promising FE above 40%. Overall, the reported performance remains much below the requirements for practical application.

4) C_2H_4 . Different from C_1 products, the dimerization of $^*\text{CO}$ to form C–C bond is the essential step for C_2 products (**Figure 4C**), followed by the hydrogenation forming C_2H_4 . Cu was found to have unique properties to yield C_2H_4 due to the unfavorable desorption of $^*\text{CO}$ and capability to form the C–C bond.⁵¹ The catalytic properties of Cu depend strongly on the facet with (100) showing higher selectivity than (111).³⁵ Generally, Cu shows a low selectivity in the neutral media with FEs commonly less than 40% and EEs less than 25%.¹²⁹ Using alkaline media was discovered to be able to promote the C–C coupling with C_2H_4 FEs above 60% and EEs above 50%.³⁰ In addition, positively charged Cu species ($\text{Cu}^{\delta+}$) shows intrinsically enhanced capability to boost the C–C formation than Cu^0 , achieving 60% FEs on both Cu oxide and Cu_3N in the natural solution.^{130, 131} The drawback is that the $\text{Cu}^{\delta+}$ species tend to be reduced to Cu^0 under negatively applied potentials, causing the decrease in electrochemical stability.³⁹

5) $\text{C}_2\text{H}_5\text{OH}$. Cu-based materials have been extensively investigated for $\text{C}_2\text{H}_5\text{OH}$. However, the mechanistic discovery demonstrates that Cu sites favor the formation of $^*\text{CCH}$ instead of $^*\text{CHCHOH}$ intermediates, preferentially resulting in C_2H_4 rather than $\text{C}_2\text{H}_5\text{OH}$ (**Figure 4C**).³² As a result, metallic Cu and Cu(I) oxide show poor selectivity with FEs below 20% and EEs as low as 5%.^{132, 133} Very recently, a tandem catalyst ($\text{FeTPP}[\text{Cl}]-\text{Cu}$), composed of molecular $\text{FeTPP}[\text{Cl}]$

and metallic Cu, was discovered to show a high FE up to 41%.³² The authors attributed the enhanced selectivity to the addition of molecular FeTPP[Cl] co-catalyst, which yields a high local CO concentration and facilitates the formation of *CHCHOH intermediates (**Figure 4C**). In addition to metal-based catalysts, metal-free carbon has been demonstrated to be able to reduce CO₂ to C₂H₅OH. A typical example is ordered mesoporous N-doped carbon, in which the pyridinic N was theoretically confirmed to serve as catalytic sites and possess better reactivity than pyrrolic N.¹³⁴ Remarkably, a high FE of 77% and an EE of 45% were realized at -0.7 V.¹³⁴ However, the current density remains very low (<1 mA cm⁻²), requiring further improvement.

Table 2. Summary of typical catalysts and their performance to produce CO, HCOOH, CH₃OH, C₂H₄, and C₂H₅OH.

Product	Catalysts	Reactor	Electrolyte	FE ^a (%)	Partial J ^b (mA cm ⁻²)	E ^c (V vs. RHE)	EE ^d (%)	Stability (h)	Ref.
CO	Oxidized Au	H-type cell	0.5 M	99	8	-0.4	81	8	21
	Au Nanoneedle		KHCO ₃	95	15	-0.35	80	8	99
	Bilayer Au/PE			92	25.5	-0.6	67	33	135
	Porous Ag			95	15	-0.35	80	8	99
	Ag-IO		0.1 M KHCO ₃	90	N/A	-0.6	66	N/A	136
	Zn plates		0.5 M KHCO ₃	80	10	-0.85	52	30	119
	ZnO		0.1 M	80	16	-1.1	46	8	66

	N, F-HCL		KHCO ₃	90	1.9	-0.6	66	40	137	
	NC-27			75	1.5	-0.71	52	1.2	138	
	F-CPC			88	33	-1	53	12	139	
	Fe-N/C			95	2.67	-0.58	70	20	103	
	Ni-N/C		0.5 M	99	28.6	-0.81	65	30	102	
	Vertically aligned NiN/CNT		KHCO ₃	97	49	-1	58	40	140	
	Co-N/C			94	16.7	-0.63	68	60	120	
	Organics-modified Cu			76	0.24	-0.7	53	10.1	141	
	MWNT/PyP BI/Au		Flow cell	2 M KOH	90	108	-0.44	72	8	142
	Ag layer on CNT			1 M KOH	99	350	-0.8	65	N/A	28
	Porous Zn foam			84	166	-0.64	60	6	22	
Ni-NCB	MEA fuel cell	Water vapor	99	85	2.46 (cell)	54	20	143		
Cobalt phthalocyanine			95	175	2.5 (cell)	51	100	144		
HCOOH	Sn dots/graphene	H-type cell	0.1 M KHCO ₃	85	21	-1.13	52	50	18	
	S-doped Sn			93	55	-0.75	68	40	122	
	mp-SnO ₂		0.5 M	83	15	-0.9	56	12	145	
	Bi Nanosheets		NaHCO ₃	95	14	-0.89	64	10	19	
	CuSn ₃ alloy		0.1 M KHCO ₃	95	33	-0.5	79	50	123	

	Atomic Co Layers		0.1 M NaSO ₄	90	10	-0.88	61	60	124
	Organics-modified Cu		0.05 M KHCO ₃	62	1.5	-0.7	46	10.1	141
	Defective Bi ₂ O ₃ nanotubes	Flow cell	1 M KOH	98	210	-0.58	78	13	29
	Commercial Sn	MEA fuel cell	Water vapor	93	52	2.2 (cell)	61	50	146
CH ₃ OH	Cu ₂ O particles	H-type cell	0.1 M KHCO ₃	47.5	3.7	-1.6	21	0.83	126
	Copper selenide		[Bmim]PF ₆ -CH ₃ CN-H ₂ O	78	41.5	-2.1 (vs. Ag/Ag ⁺)	61	25	31
	FeP Nanoarray		0.5 M KHCO ₃	80	0.96	-0.20	69	36	127
	Pd/SnO ₂ Nanosheets		0.1 M NaHCO ₃	55	0.82	-0.24	48	8	6
	CoPc-NH ₂ /CNT		0.1 M KHCO ₃	40	10	-0.94	23	11	128
C ₂ H ₄	Porous Cu foam	H-type cell	0.5 M NaHCO ₃	35	2	-0.7	25	1	147
	Porous copper foil		0.1 M KHCO ₃	35	20	-1.3	19	1.4	129
	Cu ₃ N			60	101	-1.6	30	20	131
	Cu oxide			60	10.8	-0.9	39	5	130

	Cu NPs on GDL	Flow cell	10 M KOH	66	184	-0.55	52	Not stable	³⁰	
	Graphite/NPs/Cu/PTFE			70	52~70	-0.55	55	150	³⁰	
	AgCu wire			1 M	55	175	-0.68	40	N/A	⁴⁴
	Porous Cu			KOH	39	160	-0.66	28	0.22	¹⁴⁸
	Ionomer-modified Cu				48	126	3 (cell)	22	10	¹⁴⁹
	Cu/PTFE			MEA fuel cell	Water vapor	50	100	3.9 (cell)	18	24
C ₂ H ₅ OH	polycrystalline Cu	H-type cell	0.1 M KHCO ₃	9.8	0.98	-1.08	5.0	1	¹³²	
	Cu ₂ O			16	7.68	-0.99	8.2	1	¹³³	
	Ordered Mesoporous N-C			77	~0.15	-0.7	45	24	¹³⁴	
	AgCu wire	Flow cell	1 M KOH	30	80	-0.68	18	N/A	²⁵	
	Porous Cu			17	114	-0.66	10	0.22	¹⁴⁸	
	NGQDs			12	22	-0.78	7	N/A	¹⁵¹	
	Ionomer-modified Cu			21	90	~3 (cell)	8	10	¹⁴⁹	
	Cu/FeTPP[Cl]			MEA fuel cell	Water vapor	41	124	~3.4 (cell)	23	12
Cu/PTFE			17	34	3.9 (cell)	5	24	¹⁵⁰		

^a Maximum FE;

^b Partial current density at the potential where the maximum FE is obtained;

^c Potential at which the maximum FE is obtained;

^d The applied potential at the anode was assumed to be 1.23 V because most reports did not collect potential when doing CO₂RR measurement in three-electrode H-type cell configuration and flow cell except for two-electrode configuration MEA fuel cell, which shows applied cell potential.¹⁵² Note that the actual EE might be smaller than the results calculated here since the anodic side should also show an overpotential for OER.

4. Catalysts design principles

The above-mentioned limitations and challenges largely retard the development of highly active, selective, and stable CO₂RR catalysts. Engineering the electronic structure of catalysts to adjust their inherent reactivity is largely limited by linear scaling relation. Recent advances demonstrate that, in addition to the electronic properties, morphological and interfacial properties of electrode materials can also drastically influence the electrocatalytic CO₂RR selectivity and reactivity, which are non-relevant to linear scaling relation. Therefore, fine engineering of morphology, surface, and interface could be a promising route to eventually fabricate advanced catalyst systems for high-efficiency CO₂ electro-conversion. In this section, we provided design principles on how these properties affect CO₂RR behaviors.

4.1 Local CO₂ concentration

CO₂ reduction needs a high concentration of local gaseous CO₂ at the electrode surface to achieve a large production rate. However, CO₂ has poor solubility in aqueous solution with the ratio of CO₂ to H₂O molecules being ~1:1,300 at 1 atm pressure. Along with the reaction between CO₂ and OH⁻ that consumes CO₂,¹⁵³ the availability of CO₂ molecules that can reach the electrode

surface is largely limited. Therefore, increasing local CO₂ concentration is considerably challenging but crucial. The traditional strategies to improve CO₂ concentration include increasing reaction system pressure⁵⁰ and employing alkaline metal ion;¹⁵⁴ their use, however, is hindered by the incompatibility with easy operation and limited solubility of alkaline salts. Alternatively, porous materials have been widely employed to capture CO₂ by utilizing pore as CO₂ storage space.^{3, 155} Thereby, the porous architecture could be suitable to store CO₂ and enhance the local CO₂ concentration when the catalyst's surface is hydrophobic for preventing electrolyte flowing into the pores. Besides, the hydrophobic surface itself can keep water away from the electrode surface,¹⁵⁶ leaving water-free space to store gaseous CO₂. On the other hand, gas diffusion electrode (GDE) mounted in flow cells and fuel cells can utilize hydrophobic gas diffusion layer (GDL) to quickly deliver CO₂ into the catalyst's surface while avoiding a long transportation distance in the electrolyte (**Figure 5A**).^{24, 144, 153, 157, 158} Therefore, constructing pores, employing GDL, and modifying wettability could increase local CO₂ concentration.

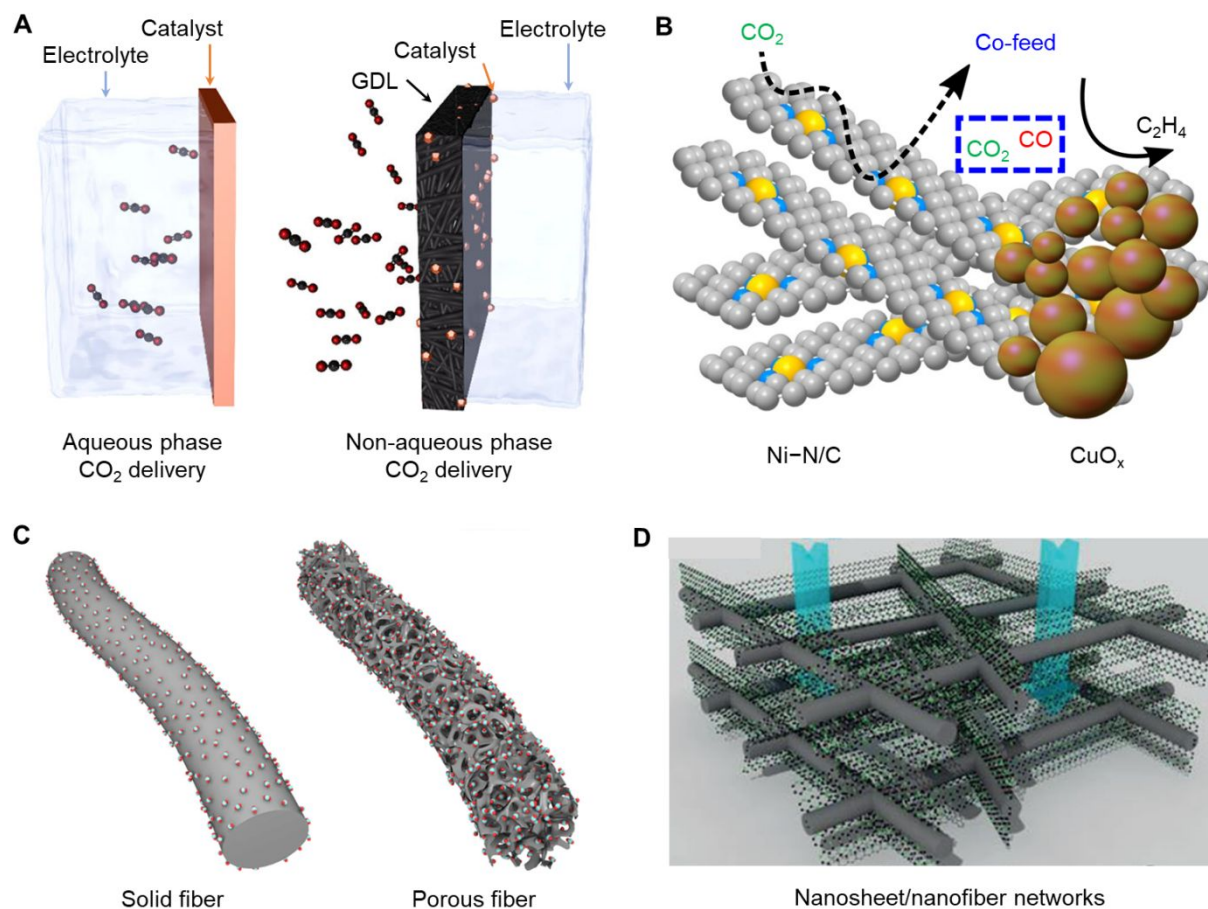


Figure 5. (A) Illustration showing CO_2 delivery modes in the aqueous phase and GDL-enabled non-aqueous phase. Adapted with permission from Ref.¹⁵³ Copyright 2019 American Chemical Society. (B) The tandem catalyst combining Ni-N/C as a CO producer and CuO_x for C–C bond coupling. Grey, blue, yellow spheres refer to C, N, and Ni atoms, respectively. Adapted with permission from Ref.¹⁵⁹ Copyright 2019 Springer Nature Group. (C) Morphological illustration of active species supported on solid fiber and porous fiber. Adapted with permission from Ref.¹⁶⁰ Copyright 2020 Elsevier. (D) Scheme of 3D networks composed of 2D nanosheet and 1D nanofiber to facilitate mass transportation. Adapted with permission from Ref.¹⁶¹ Copyright 2014 Wiley.

4.2 Interfacial alkalinity

The pH at the electrode and electrolyte interface plays key roles in CO₂RR. In 1989, Hori et al.¹⁶² found that a locally high pH near a Cu electrode could facilitate the further reduction of the *CO intermediate to C₂H₄, which was recently revealed to be from the favorable *CO dimerization at an alkaline environment.^{163, 164} In addition, a high pH circumstance can give a low concentration of proton and thus restrain HER. Note that even CO₂ reduction is conducted under a neutral pH electrolyte, the local alkalinity near the electrode surface could be gradually elevated since both CO₂RR and HER consume protons.¹³⁵ However, the high alkalinity is hard to be maintained because the local electrolyte will quickly blend with the bulk electrolyte and reduce such effect. The hydrophobic electrode can promote the preservation of high alkalinity due to insufficient contact between bulk and local electrolytes. Compared to the flat electrode, the high-porosity one is conducive to yield an enhanced local pH due to the convection inside of pores.¹³⁶

Although alkaline media can provide high alkalinity near the electrode surface, it is undesirable to use alkaline electrolytes in the H-type cell as OH⁻ can react with CO₂ and hinder the travel of CO₂ molecules to the electrode surface. Using hydrophobic GDL makes the use of alkaline electrolyte in the flow cell practicable because GDL can suppress the overlaid contact between CO₂ and KOH solution while permitting CO₂ to penetrate GDL and reach the electrode-electrolyte interface.¹⁵⁸ However, GDL tends to lose hydrophobicity in long-term use limiting its lifespan. Inserting catalyst in between polytetrafluoroethylene (PTFE)-based GDL and carbon NPs/graphite layer has been demonstrated to be able to prevent the overflowing,³⁰ where carbon NPs/graphite serves as stabilizing layer to maintain the hydrophobicity of GDL.

4.3 Management of mass transportation

If an electrocatalytic reaction involves only a single diffusing species and a single product, speeding up or lowering species transportation can only accelerate or slow down the reaction rate.⁶⁴ CO₂RR has diverse reaction intermediates/partners and compete over parasitic HER in concurrent reaction paths simultaneously. If the susceptibility of the desired reaction pathway to transport limitation is less than the unwanted one, retarding the species transportation can decrease the reaction rates of undesired reactions while the reaction rates of the reactions interested can keep unchanged. Therefore, managing the mass transportation of reaction species could control the product generation rates. For example, the desorption of CO becomes easier on a superaerophobic surface than that on a superaerophilic surface due to the poor adhesion strength between bubbles and the superaerophobic surface.¹⁴⁰ The facile detachment of CO bubbles can thus enable a higher current density.¹⁶⁵ Moreover, CO₂RR was demonstrated to have better resistance to transport limitations than HER evolution on polished polycrystalline gold.⁶⁴ This phenomenon implies that HER can be suppressed by high-porosity thin films electrode as it can amplify the influence of diffusional gradients, posing severe mass transportation limitation to HER.

In CO₂RR, the intermediate products near the electrode can act as reactants being reduced further. Thus, proper management of intermediates transportation could be an effective way to tune final product distribution. For instance, if CO cannot run off quickly, there is a higher chance that CO could further participate in the C–C bond coupling by increasing CO surface coverage.^{159,}
¹⁶⁶ It has been demonstrated that C₂H₄ generation can be improved through co-feeding CO₂ and CO by combining a CO generation-active catalyst with a catalyst having enhanced capability for

C–C coupling.¹⁵⁹ For instance, integrating single-atom Ni-N/C with CuO_x to build the tandem system can promote C₂H₄ generation (**Figure 5B**),¹⁵⁹ in which Ni-N/C function as local CO producer and CuO_x works for the *CO dimerization. Similarly, if C₂ products could be preserved near the catalyst surface, the formation of the C₃ products could be promoted because of the improved C₂–C₁ coupling. In general, the flow of desorbed products from the catalyst surface to the bulk solution depends on the catalysts' morphology. For example, a flat surface may accelerate the flow of products away from the catalyst surface, while a cavernous electrode may trap the products and increase the possibility to further participate in CO₂RR.¹⁶⁷ Therefore, designing a catalyst with special morphology that can govern the outflow or reservation of intermediates can tune the final product distribution.

4.4 Density of active sites

The overall performance of a catalyst is governed collectively by both the electronic properties of active components and the number of available active centers.^{36, 168} The former determines the inherent catalytic reactivity (such as selectivity and stability), while the latter governs the total reaction rates, namely turnover number (TON), which directly reflects the overall current density and product generation rate in CO₂RR. As aforementioned, tuning electronic structure is restricted by linear scaling limitation, which is not the aim of this Review. Fortunately, the number of active sites can be modulated by engineering the topography of electrode materials. It should be noted that only the centers where the reactant/ions can reach to them are catalytically effective sites and

can contribute to the reaction, while the species that is not accessible to reactant/ions are "inactive" and will not make difference to the reaction.

Generally, there are two ways to increase the number of effective active sites. One is to improve surface area. A large surface area can enhance the dispersion and exposure of active sites throughout the catalysts, such as ultra-thin two-dimensional (2D) materials that have a high surface-to-bulk ratio.¹⁶⁹ Another approach is to construct a porous morphology to facilitate the delivery of reactants/ions to active sites. Taking 1D fiber material as an example, atomically dispersed nickel atoms supported on solid carbon fiber has been demonstrated to exhibit a CO₂-to-CO partial current density four times smaller than that supported on porous carbon fiber,¹⁷⁰ despite the actual amount of nickel on them are the almost same. As for solid fiber, only the active species anchored on the outermost surface can contact with CO₂ and reduce it, whereas the species embedded in the fiber cannot do so due to its inaccessibility. The porous fiber can thus significantly improve the effective number of active sites as pore improves the accessibility of catalytic sites to reactants (**Figure 5C**).¹⁶⁰ Therefore, a catalyst with a high surface area and porous architecture can build an efficient three-dimensional (3D) electrochemically active interface and significantly enhance the exposure of active sites.

4.5 Enhancement in kinetics

CO₂ reduction shows slow kinetics, partially due to the poor mass transportation and multiple electron transfer process. In the aqueous condition, delivering CO₂ to electrode surface at a high flux is challenging because of its low solubility and reactions with electrolyte.¹⁵³ Especially under

a larger overpotential, where the reaction rate is fast, the mass transportation of CO_2 becomes more crucial due to the quick consumption of CO_2 . As discussed in subsection 4.1, using hydrophobic GDL can efficiently deliver CO_2 to the electrode-electrolyte interface, and porous thin films can inhibit the competitive HER kinetics due to the transportation limitation of protons from the bulk electrolyte into the pores. In the case of the electrode being composed of solid spherical powder catalysts, the transportation of CO_2 through electrode surface to internal catalysts is difficult, while the hollow porous spherical catalysts can enable efficient transportation as the reactant can pass through the inside of the hollow sphere.¹³⁹ Two-dimensional (2D) nanosheets tend to stack owing to the strong electrostatic interaction between interlayers resulting in poor mass delivery, anchoring 2D nanosheets on 1D fibers to reticulate a porous network can enable smooth mass transportation (**Figure 5D**).¹⁶¹ On the other hand, the fast electron transfer is needed to boost CO_2 kinetics for producing high-order products since multiple electrons are required (**Table 1**). Using conductive support to load active materials could be an effective way to do so. It has been shown that employing carbon nanotube to anchor phthalocyanine (CoPc) can drastically boost the six electrons reduction of CO_2 to CH_3OH thanks to accelerated electron transfer,¹²⁸ while CoPc alone shows two electrons reduction of CO_2 to CO. In view of these arguments, building desirable electrode catalysts' configuration could drastically boost their CO_2RR kinetics.

5. Approaches to engineer electrodes and their performance

As stated in the previous sections, catalysts' morphology and electrode-electrolyte boundary play key roles in governing CO_2RR . In this section, we summarized recently developed strategies

to fabricate engineered electrode materials and their CO₂ reduction performance. Particularly, we focused on constructing favorable three-phase interfaces, engineering surface wettability, and designing special local morphology. It is noting that these aspects have their unique influences in tuning CO₂RR behaviors. In the meantime, they have relevance in most cases, governing CO₂RR in a mutual way. As we have discussed the category of catalysts based on products, we will not group this section by products. Instead, we will pay much attention to discuss the influences of the modified interface, surface, and morphology on CO₂RR, pointing to find out the activity-determining factors and gain insight into catalytic mechanisms.

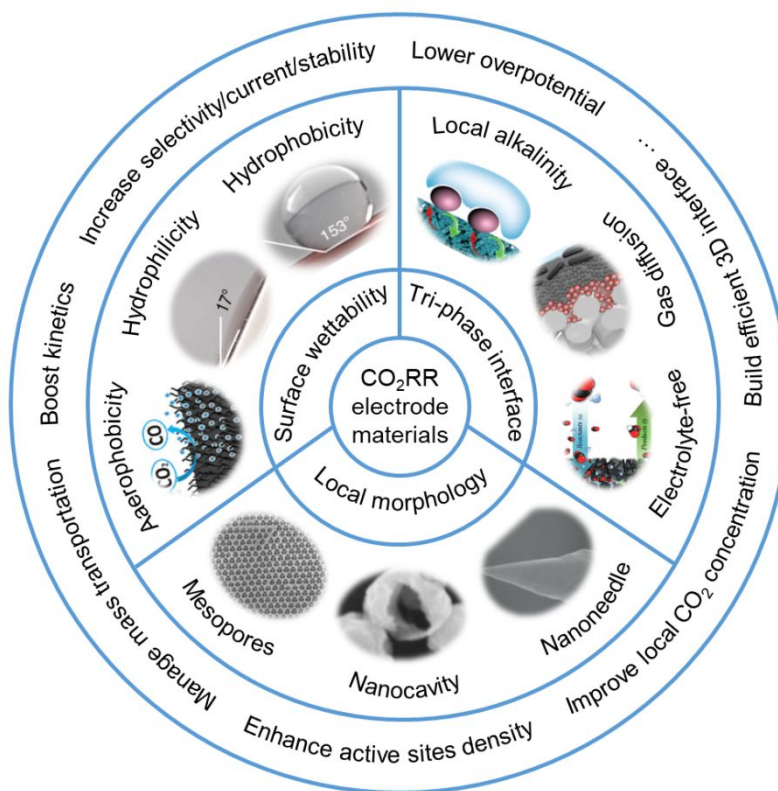


Figure 6. Morphology, three-phase interface, and surface wettability impacting CO₂ reduction.

5.1 Constructing favorable three-phase interface

The interface at gaseous CO₂-solid electrode-liquid electrolyte is at the cornerstone of CO₂ electrocatalysis, where CO₂ encounters with electrons and protons and is reduced. Therefore, the properties of electrochemical interfaces govern CO₂RR behaviors to large content. Designing an electrode with efficient contact of CO₂, H₂O, and catalysts could provide opportunities to achieve high accessibility of concentrated CO₂ molecules to the catalyst surface while reducing the efficiency of HER. In this subsection, we will present the advancements of building highly active three-phase boundary in the neutral, alkaline, and electrolyte-free conditions.

5.1.1 Interface under neutral media

The neutral electrolyte is one of the most used media in CO₂ reduction because it can provide the necessary proton source for CO₂RR and suppress the unwanted reaction between OH⁻ and CO₂. However, due to the inherent drawbacks of low CO₂ solubility and inevitable HER, CO₂RR under neutral electrolyte suffers low efficiency with poor selectivity and current density. To solve these limitations in the neutral solution, Cui et al.¹³⁵ developed a bilayer pouch-type alveolus-like electrode made of a highly flexible nanoporous polyethylene (nanoPE) membrane covered with a layer of Au catalyst on one side to achieve a sufficient amount of catalytic active sites at the three-phase interface. This design is inspired by the mammalian lung, which is an evolutionary compartment (around 200 μm in diameter) enclosed by many ultrathin waterproof membranes (~1 μm thick) with enhanced gas diffusibility but low water permeability. The basic working mechanism is that the gas can penetrate the multilayered membranes and be quickly exchanged

between the alveoli and blood capillaries, while the liquids stay separated. The configuration of the natural lung is similar to the electrode architecture needed for CO₂ reduction where CO₂ is expected to be transported quickly while the water should be kept away from electrode to maintain high CO₂ concentration near the electrode.

The Au/PE was fabricated by rolling the nanoPE membrane deposited with Au nanoparticles (**Figure 7A**). Because of the hydrophobic nature of the nanoPE allowing gas diffusion but not water, the central sealed compartment can be separated from the external electrolyte. Therefore, CO₂ can diffuse into the pores of the nanoPE and subsequently throughout the whole nanoporous framework to form an efficient contact between Au, H₂O, and CO₂ (**Figure 7B, C**), resulting in abundant accessible active sites at the three-phase interface. Another merit of Au/PE is that it allows a high local pH in the interlayer of Au/PE. It was found that the local pH increases from an initial 7 to 9.6 within the first 50 min and then keep stable during a 5 h test, which was attributed to the consumption of protons during the CO₂RR and HER processes. Such a high local alkalinity significantly inhibits HER and promote CO₂ reduction. Regarding the conventional flat electrode, it can only utilize the CO₂ dissolved in the electrolyte, leading to an insufficient three-phase interface and low-density of exposed active sites. The direct contact of bulk electrolyte to the flat electrode surface also results in a low-pH environment, which is favorable to the competitive HER.

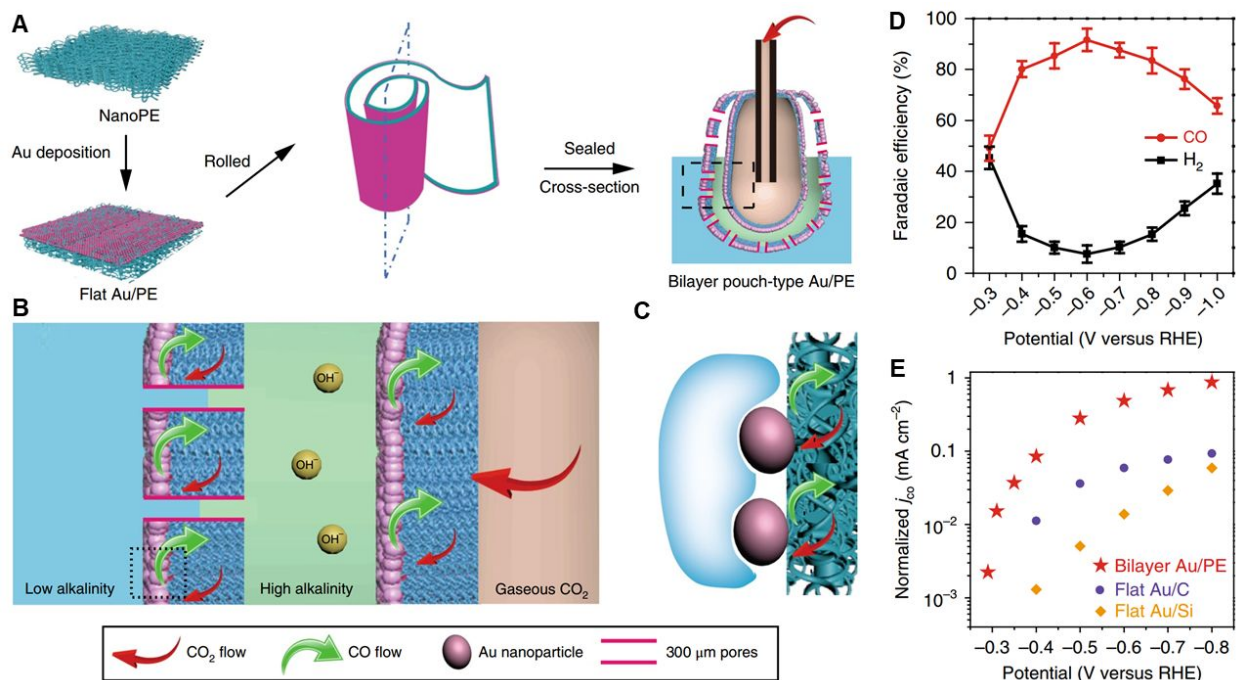


Figure 7. (A) Schematic of the synthesis procedure for Au/PE electrode. (B) Schematic of the detailed structure of Au/PE (dashed line in Figure 7A). Brown shows the inner CO₂; green refers to high-alkalinity electrolyte and blue presents low-alkalinity bulk electrolyte. (C) Enlarged image of the dotted square in Figure 7B showing more details of the three-phase interface. (D) FEs for CO and H₂ achieved in CO₂-saturated 0.5 M KHCO₃. (E) ECSA-normalized current densities of CO on bilayer pouch-type Au/PE, flat Au/C, and flat Au/Si. Adapted with permission from Ref.¹³⁵. Copyright 2018 Springer Nature Publishing Group.

With these advantages, the bilayer Au/PE exhibited a maximum FE for the reduction of CO₂ to CO reaching 92% at -0.6 V (**Figure 7D**), better than those of the flat Au/C (60%) and Au/Si (20%). The CO partial currents normalized by electrochemical active surface area (ECSA) on Au/PE are also significantly larger than flat Au/C and Au/Si (**Figure 7E**). Because Au catalysts

on these electrodes were prepared using the same magnetron sputtering method, the influence of electronic structure can be excluded, and the enhanced activity suggests the more active and selective nature of Au/PE's interface as compared to that of the flat electrode. We found that the CO FE and current density of Au/PE (92% and 25.5 mA cm^{-2} at -0.6 V) are even better than reported Au nanorod (60%, 3.7 mA cm^{-2})⁹⁹ and mesoporous Au film (78%, 5.7 mA cm^{-2}) under the similar testing condition.⁶⁴ However, whether this bilayer configuration could be employed to efficiently produce other products needs further investigation, for example replacing Au by Cu⁵¹ and SnO₂¹⁷¹ for producing C₂ and HCOOH products, respectively.

5.1.2 Interface under alkaline electrolyte

Alkaline environment is beneficial to increase CO₂RR selectivity since the reaction rate of the HER can be suppressed in the base solution owing to the sluggish kinetics of the Volmer step in HER.^{172, 173} However, dissolving CO₂ in a strong base solution is not feasible since CO₂ will be consumed quickly through the reaction between CO₂ and OH⁻ generating carbonate. Dinh et al.³⁰ achieved CO₂ reduction under extremely alkaline conditions in flow cells, in which CO₂ is separated from the KOH solution but can penetrate hydrophobic GDL with a short diffusion length to reach the interface of the Cu catalyst and KOH electrolyte (**Figure 8A**). This abrupt interface also provides a feasible way to study the effect of OH⁻ on CO₂RR. They discovered that the CO₂RR onset potentials shifted positively when increasing KOH concentrations. Notably, CO can be formed at a potential of -0.14 V vs. RHE in 10 M KOH, very close to the thermodynamic equilibrium potential (-0.11 V vs. RHE); the formation of C₂H₄ took place at -0.165 V vs. RHE,

meaning an onset overpotential of 235 mV given that the equilibrium potential for CO_2 -to- C_2H_4 is 0.07 V vs. RHE (**Table 1**). Utilizing density functional theory (DFT) calculation, they found that the presence of OH^- help to adsorb OCCO intermediate from the $^*\text{CO}$ dimerization on the Cu surface. This is because OH^- increases the charge imbalance between carbon atoms in OCCO, which stabilizes OCCO through a stronger dipole attraction. Such a benefit decreases the energy barrier for the $^*\text{CO}$ dimerization to form OCCO and further C_2H_4 under a more alkaline condition, supporting their experimental finding that a concentrated KOH solution gives rise to a decreased onset overpotential for C_2H_4 formation.

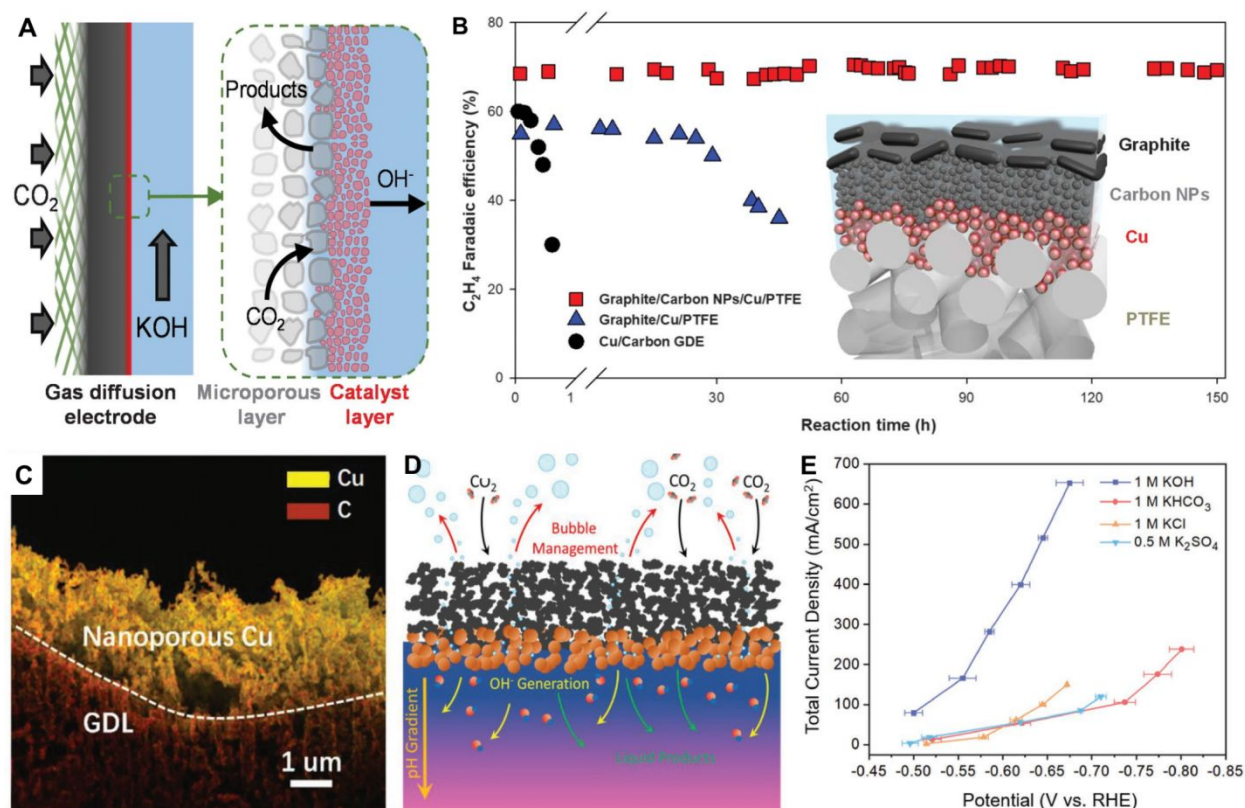


Figure 8. (A) Schematic of the GDE cathode. (B) Long-term stability of CO_2 RR in 7 M KOH on graphite/carbon NPs/Cu/PTFE electrode and a traditional carbon-based GDE. Insets show the

illustration of the graphite/carbon NPs/Cu/PTFE electrode. Adapted with permission from Ref.³⁰. Copyright 2018 American Association for the Advancement of Science. (C) A cross-sectional SEM image of the porous copper. (D) Illustration of the electrode-electrolyte interface. (D) Total current density at different potentials calculated based on the surface pH. Adapted with permission from Ref.¹⁴⁸. Copyright 2018 Wiley.

In addition, the penetration distance of CO₂ into the electrolyte was shorter in a concentrated KOH electrolyte, which facilitates the CO₂ diffusion to the interface and thus the electrokinetics of CO₂ reduction. Accordingly, the high CO₂-to-C₂H₄ performance with an FE of 66%, a total current density of 275 mA cm⁻², and an EE of 52% was achieved in 10 M KOH on copper using traditional carbon-based GDL. However, the stability is poor due to the loss of hydrophobicity of GDL in 1 hour. The flooded surface blocks the CO₂ transfer pathway and decreases reaction current.

To address the surface hydrophilization, they designed a new electrode by sandwiching Cu catalysts in between the polytetrafluoroethylene (PTFE) and carbon nanoparticles (NPs), forming a graphite/carbon NPs/Cu/PTFE configuration (**Figure 8B**). The hydrophobic PTFE layer could prevent flooding, and the protected effect by outer carbon NPs/graphite layer could stabilize Cu catalyst and maintain the abrupt reaction interface. With this design, a stable FE of 70% for C₂H₄ was achieved without decay in 150 h continuous operation. This result is the highest FE and stability reported so far in the reduction of CO₂ to C₂H₄. However, this design results in an inefficient contact between CO₂, Cu, and KOH, lowering the current density from 275 mA cm⁻²

on carbon-based GDL to 100 mA cm^{-2} on graphite/carbon NPs/Cu/PTFE electrode. Further research on designing both high current and stability is highly required.

In another study, Jiao et al.¹⁴⁸ applied a highly porous Cu catalyst in the alkaline flow cell (**Figure 8C**) to enable efficient mass transportation. The highly porous Cu affords a diffusion pathway facilitating CO_2 delivery across the electrode-electrolyte interface, which also promotes the flow of gaseous products away from catalyst surface and leaving a large number of available catalytic sites for CO_2 reduction (**Figure 8D**). They also studied the influence of electrolyte (1 M KOH, 1 M KHCO_3 , 1 M KCl, and 0.5 M K_2SO_4) on the catalytic CO_2RR properties. One role of adding supporting electrolytes is to increase the conductivity of the aqueous electrolyte, which has a positive effect to enhance total current density because it can help to increase the diffusional flux of ions.²⁸ The authors discovered that the electrolyte conductivity follows the order of $\text{KOH} > \text{KCl} > \text{K}_2\text{SO}_4 > \text{KHCO}_3$, in a good agreement with the tendency of total current density observed (**Figure 8E**). Another role of electrolytes is to tune the pH of the electrolysis environment. The pH of the electrode surface is slightly lower than that of the bulk electrode in 1 M KOH owing to the formation of carbonate near the catalyst surface. By contrast, in the non-buffering electrolytes with Cl^- and SO_4^{2-} as anions, the pH of the electrode surface is considerably larger than that of the bulk electrode due to the production of a large amount of OH^- during high-rate CO_2 electrolysis, changing pH by 4 units. As for KHCO_3 , there is only a slight increase in surface pH due to the buffering capability of HCO_3^- anion. The surface pH thus follows the order of $\text{KOH} > \text{KCl} \sim \text{K}_2\text{SO}_4 > \text{KHCO}_3$, which is approximately consistent with the C_{2+} product selectivity. This agrees with both experimental and theoretical findings reported by Dinh et al.³⁰ that a high near-surface

OH^- concentration is favorable for C–C coupling. Accordingly, this porous Cu exhibited a CO_2 reduction current density of 653 mA cm^{-2} with a C_{2+} product selectivity of 62% at -0.67 V in the KOH electrolyte. Short-term stability working at 653 mA cm^{-2} for 800 s and 200 mA cm^{-2} for more than 2 h were also demonstrated (**Table 2**).

Besides reducing CO_2 to C_2 products, converting CO_2 to CO in alkaline flow electrolyzer was also demonstrated by Kenis et al.¹⁴² showing a high CO production rate of 158 mA cm^{-2} at a small cell overpotential of 0.94 V with an energy efficiency of 63.8% on the Au catalyst. More notably, a record-high current density of 350 mA cm^{-2} and EE of 65% was achieved using 1 M KOH as the electrolyte at a cell whole potential of 3 V on the Ag/carbon nanotubes catalysts.²⁸ Despite the high efficiency of CO_2 -to-CO on noble metals, their prohibitive cost and limited reserve preclude the massive use. Developing highly advanced non-precious CO_2RR catalysts is more desirable. Using a porous electrodeposited Zn as a low-cost free-standing electrode, Züttel et al.²² achieved high-rate CO_2 reduction in alkaline flow cell delivering a CO current density of 164 mA cm^{-2} , FE of 84%, and EE of 60% at a moderate potential of -0.64 V . In addition, reducing CO_2 to HCOOH was also achieved in the flow cell by Li et al.²⁹ exhibiting a high FE of 98% at a current density of 210 mA cm^{-2} for 13 h at a cathodic potential of -0.58 V on defected bismuth oxide nanotubes.

Despite these exciting advancements achieved in the past few years, it should be noted that achieving high-efficiency stable CO_2 reduction at a high current density above 200 mA cm^{-2} for more than 1000 h still faces great challenges in the alkaline flow cells. One reason is that the accumulation of carbonate salt from the reaction between CO_2 and OH^- at the electrode-electrolyte interface will block the pores of the GDL,¹⁵³ causing a gradual decrease in electron conductivity

(voltage losses) and inefficient mass transportation. Also, long-term use will lead to the loss of hydrophobicity and thus flooding of GDL,³⁰ which in return reduces the capability of GDL to prevent overlaid contact between CO₂ and the alkaline electrolyte. Future innovations on engineering reactor and catalyst are still highly needed to address these issues.

5.1.3 Interface under electrolyte-free condition

In aqueous CO₂ reduction, the catholyte plays a key role in serving as a media to transfer ions. However, using electrolytes leads to a low concentration of CO₂ because of poor CO₂ solubility in the aqueous solution. When applying large overpotential, the hydrogen evolution will also be maximized in the aqueous condition. The best way to circumvent these limitations is to avoid the use of liquid catholyte. In 2015, Lee et al.¹⁷⁴ proposed CO₂ reduction in fuel cells by directly feeding gaseous CO₂ at the cathode. However, the FE towards formic acid was only 5% with a very poor partial current density of less than 0.5 mA cm⁻² due to the absence of efficient contact between CO₂, catalysts, and proton.

In 2018, Park et al.¹⁴⁶ proposed an effective approach to solve the above issues by feeding water vapor with gaseous CO₂ to the membrane electrode assembly (MEA) at cathode using a compact fuel cell configuration (**Figure 9A**). The water vapor functions as a carrier to deliver CO₂ to the electrode catalyst surface, generating a CO₂-saturated thin liquid film on the electrode surface. After consuming CO₂ in the film during the reduction process, it can be quickly supplemented from the gas stream. This configuration not only achieves the efficient three-phase interface with improved CO₂ concentration and mass transfer but also provides an approach to

obtain the concentrated liquid product with an extremely small amount of water, which cannot be realized in aqueous CO_2 reduction condition. As a result, a significantly high formic acid concentration of 41.5 g L^{-1} was achieved under a partial current density of 51.7 mA cm^{-2} , a FE of 93.3%, and an EE of 61% at a low cell voltage of 2.2 V using commercial Sn catalyst.

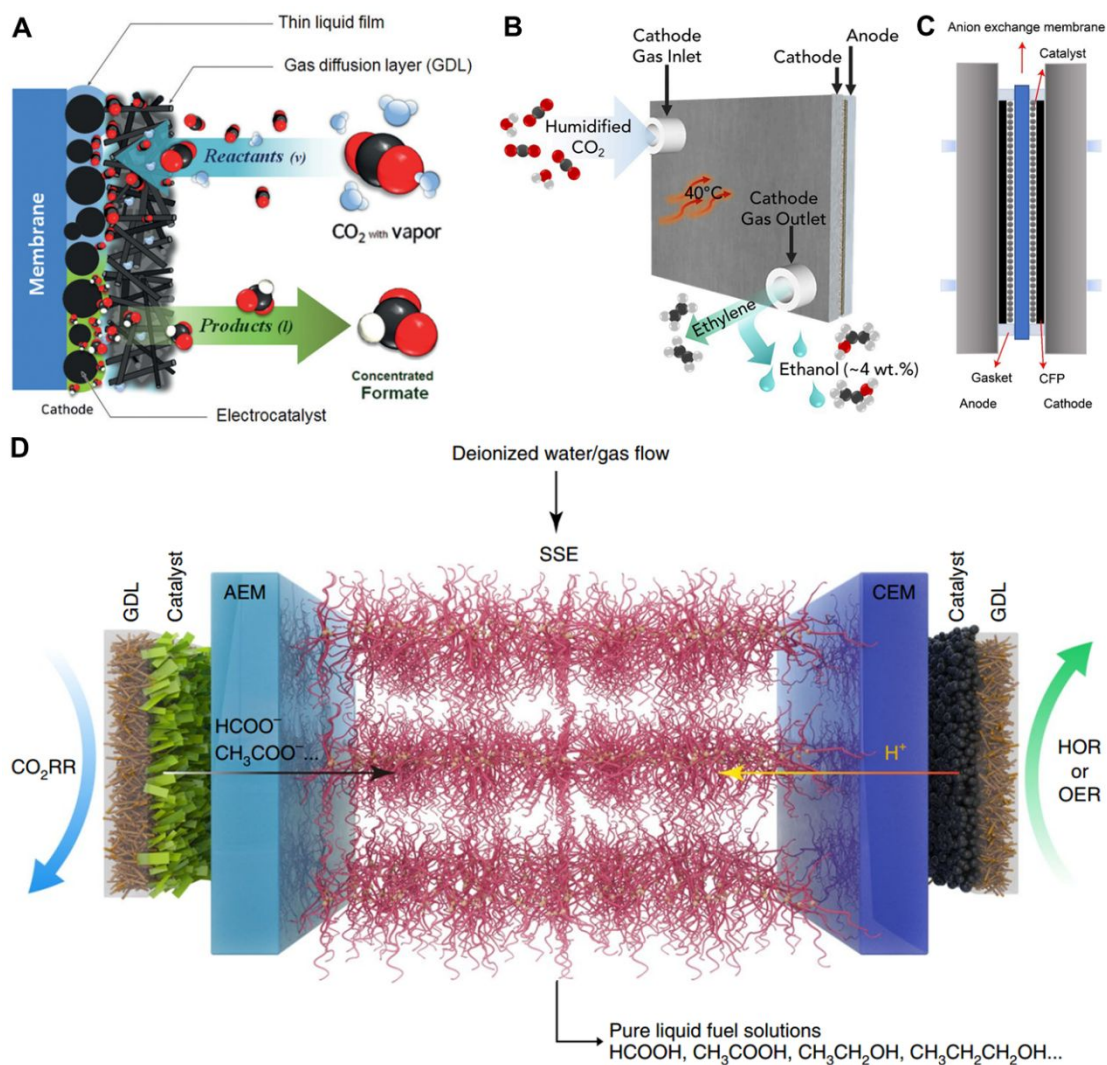


Figure 9. (A) Schematic of CO_2RR under a catholyte-free interface for formate synthesis. Adapted with permission from Ref.¹⁴⁶. Copyright 2018 Wiley. (B) Schematic of the MEA fuel cell electrolyzer. Adapted with permission from Ref.¹⁵⁰. Copyright 2018 Elsevier. (C) Schematic of

cross-section details of the MEA. Adapted with permission from Ref.¹⁴³. Copyright 2018 Elsevier.

(D) Schematic illustration of the CO₂ reduction using a solid electrolyte to produce pure liquid products. Adapted with permission from Ref.¹⁷⁵. Copyright 2018 Nature Publishing Group.

Different from flow cells, the cathodic GDE is compressed directly with the ion exchange membrane in the fuel cells (**Figure 9B, C**), which is conducive to give low ohmic resistance. More importantly, issues associated with the side reaction between electrolyte and CO₂, GDL fouling, and decreased liquid concentration in the flow cells can also be eliminated under electrolyte-free MEA. Sinton et al.¹⁵⁰ systemically compared the performance of flow cell and MEA fuel cell, revealing that MEA mounted with an anion exchange membrane (AEM) shows higher performance. The high FEs of 50% and 80% for C₂H₄ and C₂₊ products, respectively, were achieved with an ethylene concentration up to 30% and an ethanol concentration reaching 4 wt % under a high current density of more than 100 mA cm⁻² for continuously stable operation of 100 h. However, the system requires a cell voltage of 3.9 V, resulting in a low EE of 18%. Using similar MEA configuration, a high-efficiency conversion of CO₂ to CO was achieved using low-cost single atomic Ni supported on commercial carbon black, reaching a current density of 85 mA cm⁻², a FE of almost 100%, and an EE of 54% over 20 h continuous operation.¹⁴³ Note that in MEA, it is better to use an AEM instead of a proton exchange membrane (PEM) because the later yields a high proton concentration at the cathode, which increases proton reduction and decreases CO₂ reduction efficiency.

To obtain ultrahigh-purity liquid products, Wang et al.¹⁷⁵ have proposed a combination of solid-state electrolyte (SSE) with MEA (**Figure 9D**). In the SSE-assisted electrolyzer, the cathode and anode were separated by AEM and PEM, respectively. In between the two membranes, there is a porous solid ion conductor, which contacts closely with membrane to transport the ions formed from both cathode and anode. The humidified CO₂ gas is supplied at the cathode and reduced to negatively charged species such as HCOO⁻, which transports across the AEM to SSE. Similarly, the protons generated by water oxidation at the anode can move through the PEM to the SSE for compensating the charge simultaneously. At the SSE, the ionic recombination yields high-purity HCOOH, which can be readily collected by washing the SSE with slow water or purging with humidified gas. As a result, the production of 12 M HCOOH with a high FE above 90% was achieved using a bismuth nanosheet catalyst. Employing the same cell design, they also synthesized concentrated high-purity hydrogen peroxide solution with a concentration of up to 20 wt%.¹⁷⁶ The SSE-enabled electrolyzer presents a promising prototype to produce high-purity liquid products in the practical application, and future works are suggested to further improve the ion conductivity and stability of the solid electrolyte to improve the energy efficiency and durability of the electrosynthetic cell.

In the field of the high-rate flow cells or MEA fuel cells, one concern that has been widely ignored is the difference of CO₂ flow rate at the inlet and outlet. Currently, the FEs reported in the most GDEs-type electrolyzers were calculated based on the inlet CO₂ flow, and only a few works on CO₂ reduction to CO employed outlet flow rate.^{177, 178} Ma et al.,¹⁷⁹ studied the effects of current density and type of electrolytes on the CO₂ flow rate and found that the outlet CO₂ flow rate is

lower than that of the inlet. Such a situation is much worse at larger current density and KOH electrolyte due to the quick consumption of CO₂ during reduction and the severe side consumption from reacting with OH⁻. For instance, the CO₂ rate after the electrolyzer is around 34 ml min⁻¹ at 300 mA cm⁻² in 5 M KOH, much smaller than that of 45 ml min⁻¹ before reaction. Such a difference results in the overestimation of FEs when the initial flow rate was employed. We here call for the attention to this situation and recommend using the outlet flow rate to calculate FEs in the case of high-rate CO₂ electrolysis.

5.2 Surface wettability engineering

CO₂ reduction depends strongly on the concentrations of protons and CO₂ near the electrode surface, both of which can be tuned by engineering electrode surface wettability. Thereby, exploring relationships between surface wettability and CO₂RR activity could establish useful design guidelines for developing active and selective electrocatalysts. Buckley et al.¹⁴¹ employed organic modifiers to alter surface wettability of Cu catalysts and achieved the tuning of CO₂RR selectivity for H₂, CO, and HCOOH. It was discovered that protic, hydrophilic, and hydrophobic species could enhance selectivity for H₂, CO, and HCOOH production, respectively. More typically, the hydrocarbon contents of organics also affect selectivity with a larger hydrocarbon content (eg., modifier 8 in **Figure 10A**) improving CO selectivity and a less hydrocarbon content (eg., modifier 9 in **Figure 10A**) improving formic acid selectivity.

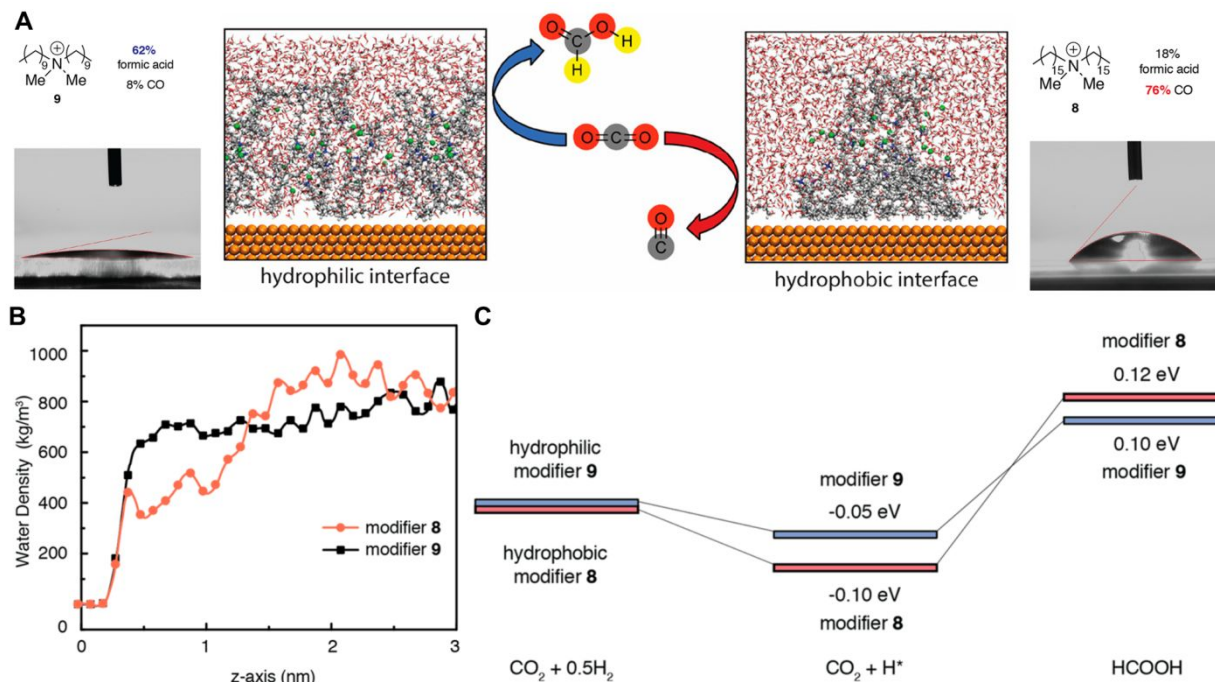


Figure 10. (A) Modulated interfacial snapshots and contact angles between water and hydrophilic modifier 9 and hydrophobic modifier 8 decorated Cu surfaces. Blue, gray, red, white, and green spheres present N, C, O, H, and Br, respectively. (B) Water density along the z-axis on Cu surfaces decorated with 8 and 9 species. (C) HCOOH formation energies on modifier 8 and 9-decorated Cu surface. Adapted with permission from Ref.¹⁴¹. Copyright 2019 American Chemical Society.

The molecular dynamics simulations show that the modifier 9 is well distributed on the Cu surface with enhanced solvation, reticulating a dispersed network and hydrophilic surface with a smaller water contact angle. While the modifier 8 tends to assemble into larger clusters on the Cu electrode, forming a hydrophobic surface with a larger contact angle. Accordingly, water density near the Cu surface decorated by modifier 9 is higher than that adorned by modifier 8 (**Figure 10B**), which influences the binding strength of hydride species (M–H) on the Cu surface.¹⁸⁰

Specifically, the hydride species can be stabilized on 8-modified Cu in comparison with that decorated by 9. A previous study demonstrates that HCOOH formation proceeds through the direct reaction between CO₂ and a surface M–H producing HCOO[−], followed by the addition of H from H₂O.¹⁸¹ Therefore, the weakened M–H species could promote HCOOH generation on the hydrophilic surface, whereas a hydrophobic surface having strong M–H bonds suppresses HCOOH formation and allows dominant CO (**Figure 10C**). These findings reveal that product selectivity is sensitive to the wettability of catalyst surface, which opens up a new direction to design CO₂RR catalysts by appropriately engineering surface hydrophilicity. However, we note that the reported activity is still low. The hydrophobic Cu surface shows an FE of 76%, a partial current density of 0.24 mA cm^{−2}, and an EE of 53% at −0.7 V for CO generation. The hydrophilic Cu surface exhibits an FE of 62%, a partial current density of 1.5 mA cm^{−2}, an EE of 46% at −0.7 V for HCOOH generation. The reported stability is around 10 hours. More efficient modifiers are expected to be developed to further improve CO₂ reduction performance.

More recently, Wakerley et al.¹⁵⁶ designed hierarchical hydrophobic Cu dendrites to trap CO₂ at the electrode-electrolyte interface (**Figure 11A**) and achieve enhanced selectivity for C₂ products. This design was inspired by plastron that has hydrophobic hairs to trap air, thereby allowing the spider to breathe underwater. The Cu dendrite electrode was prepared by electrodeposition, followed by submerging the dendritic Cu into liquid 1-octadecanethiol to form an alkanethiol layer with a thickness between 2 and 3 nm (**Figure 11B**). With the surface treatment, the wettability of the Cu dendrite was changed from hydrophilicity on the pristine surface to

superhydrophobicity on the modified surface with the contact angle increased from 17 to 153° (Figure 11C, D). A stable 12 hours electrolysis on the hydrophobic dendrites was demonstrated.

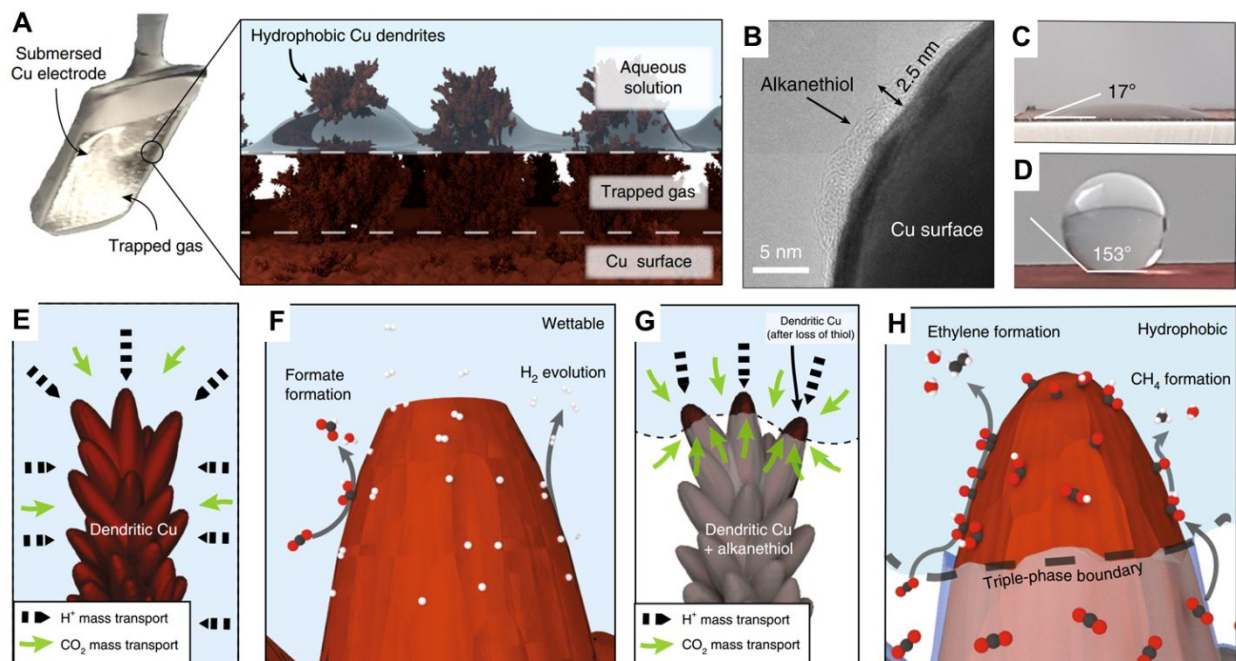


Figure 11. (A) Schematic of using a hydrophobic dendritic Cu to trap gas at the electrode-solution interface. (B) High-resolution TEM images of a 1-octadecanethiol-treated Cu dendrite. (C,D) Contact angles of the wettable (C) and hydrophobic Cu (D). (E, F) Schematic of product formation and mass transport on the hydrophilic dendrite electrode. (G, H) Schematic of enhanced CO_2 mass transport at the hydrophobic dendrite electrode. Adapted with permission from Ref.¹⁵⁶. Copyright 2019 Springer Nature Group.

CO_2 reduction testing shows that H_2 evolution on the hydrophobic surface was slower as compared to that on the pristine wettable counterpart, while CO_2 reduction efficiency was significantly enhanced. Notably, at -30 mA cm^{-2} , the hydrophobic dendrite exhibits a FE of 74%

for C_2 products, which is comparable to the GDL-enabled systems in the base media. The authors proposed that, under CO_2 reduction condition, the dendrites can react with either CO_2 or H^+ to form $Cu-COOH^*$ and $Cu-H^*$ intermediates at highly cathodic potentials.¹⁸² The hydrophilic dendrite possessing a large water content around the electrode interface could enable an accelerated H^+ transportation from the bulk electrolyte to Cu surface, thus promoting the proportion of $Cu-H^*$ groups and H_2 formation (**Figure 11E, F**). By contrast, the electrolyte is relatively far away from the hydrophobic dendrite, leaving large space in the pore of hierarchical Cu dendrites to trap CO_2 gases for boosting CO_2 mass transportation. Thereby, the $Cu-COOH^*$ concentration is greatly enhanced, which further yields high-density distribution of $Cu-CO^*$ intermediates after the dissociation of $COOH^*$, accelerates C-C coupling and the efficiency of C_2 products (**Figure 11G, H**).

Flue gas containing 5-15% v/v CO_2 could be a cheap feedstock in the application as it is the primary source of anthropogenic CO_2 emissions from the combustion of fossil fuels (**Figure 12A**).^{183, 184} However, the O_2 impurities in flue gas potentially causes a decrease in CO_2RR efficiency since the thermodynamic potential of oxygen reduction reaction (ORR) is more positive than that of CO_2RR (**Figure 12B**).^{185, 186} For instance, at a cell voltage of 2.5 V, 90% of the electrons supplied to the reaction were diverted to the parasitic ORR. To solve the above problem, Sinton et al.¹⁴⁹ developed an ionomer-assisted strategy with wettability engineering to selectively impedes O_2 but allows CO_2 transport to the electrode to be reduced on the Cu catalyst. In the hydrophobic gas diffusion channels, the gases must undergo the degas from the around solution film before entering the nanopores (**Figure 12C**). By contrast, hydrophilic ionomers nanopores

can be filled with electrolyte, which can deliver gaseous reactants to reach catalysts in the dissolved form.

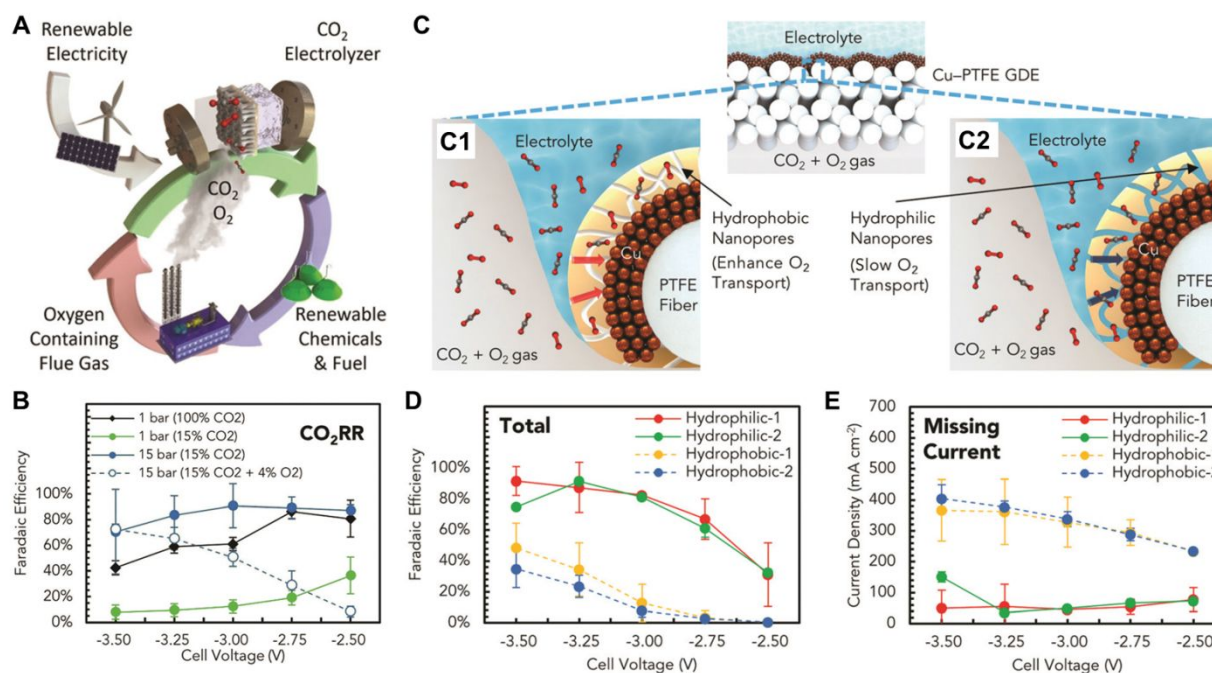


Figure 12. (A) Schematic of electrochemical CO₂ recycling using flue gas. (B) CO₂RR FEs for 15% CO₂ (v/v) with and without O₂ in the stream. (C) Schematic illustration of the ionomers-coated Cu-PTFE GDE. (C1) Schematic of the GDE decorated with the hydrophobic nanoporous ionomer. (C2) Schematic of the GDE modified with the hydrophilic nanoporous ionomer. (D) The total FEs of CO₂RR and (E) missing current density for the different ionomers. Adapted with permission from Ref.¹⁴⁹. Copyright 2020 RSC.

Because of the high volatility of O₂, it has a relatively high degassing rate in the aqueous media, thus enabling a much higher mass flux in the hydrophobic nanopore networks as compared to that in the hydrophilic channels. As for CO₂, it has low volatility, and the hydrophobicity of

nanopore shows an ignorable impact on CO₂ mass flux. Therefore, hydrophilic nanopores were proposed to reduce O₂ mass transportation but facilitate CO₂ diffusion into the catalyst surface. Experimentally, the modification of copper with hydrophilic ionomers achieved much higher FEs saving more than 70% FEs and lower missing currents saving more than 300 mA cm⁻² at 3.25 V as compared to hydrophobic ionomers-modified ones (**Figure 12D, E**). This finding implies that wettability engineering in the supporting layers presents a powerful approach to address the challenges for the flue gas. However, whether this concept could be applied to other catalysts and to avoid the interferences from other impurities (SO_x, NO_x, CO) needs further investigation.

In the above-mentioned works, the enhanced CO₂ reduction activity and selectivity were mainly attributed to the ionomer-induced surface wettability contribution. However, there are a few concerns. Firstly, these organic ionomers are composed of S, N, or F-containing carbon chains, which may potentially bring electronic effects because heteroatoms-containing groups may modify the electronic properties of surface Cu atoms. Indeed, a previous report shows that coating polyethyleneimine (PEI) over N-doped carbon nanotubes can lower overpotential and increase selectivity for reducing CO₂ to HCOOH as PEI overlayer serves as a co-catalyst to stabilize CO₂⁻ intermediate by H-bond interaction.¹⁸⁷ Besides, the findings show that incorporating high-electronegativity S and F into nitrogen-functionalized carbon can enhance CO₂RR selectivity over HER because the S- and F-induced charge redistribution could alter the interaction between catalytically active N sites and *COOH intermediate.^{137, 188, 189} Therefore, the use of organic modifiers may impact the adsorption or desorption of CO₂RR-generated intermediates by electronic effects. Secondly, reported works show stability testing less than 15 hours, far wavy

from the practical application. Whether the organic-modified system can last for a few hundred hours remains unknown. One challenge is that the ionomers may be decomposed under high cell voltage during a long-term period, which is potentially harmful for the lifetime of catalysts. Thirdly, covering organic modifiers on catalysts may block their active sites and reduce their accessibility to the electrolytes and reactants. Especially for the hydrophobic modifiers, coating them on catalysts has been demonstrated to largely decrease the ECSA due to the poor wettability of the catalyst surface to electrolytes.¹⁵⁶ We thus suggest that the electronic effects, long-term electrochemical stability, and the diminution of accessible active sites for organics-decorated systems should be further explored.

5.3 Morphology-induced activity tuning

The morphological architecture of electrode materials has been identified to be a crucial factor in determining heterogeneous electrocatalytic performance. Catalyst's morphology could affect the catalytic process on different length scales from the nanoscale, microscale, to macroscale. At the nanoscale, morphology may affect the local electronic structure, such as facet,¹²³ grain boundary,^{180,} edge,¹⁸¹ corner,^{45, 46} surface distortion.⁴⁷⁻⁴⁹ At the microscale to macroscale, modifying morphology may change local CO₂ concentration,⁹⁹ adsorption/desorption of species,^{140,190} pH gradients,¹³⁶ wettability,^{191, 192} and mass transportation.^{193, 194} As indicated before, nanoscale electronic influences are not the scope of this Review. In this subsection, we will focus on morphology-induced non-electronic contributions on CO₂RR performance. Therefore, we

selected model catalysts having the similar electronic structure of active sites as much as possible, and we pointed out their possible effects on apparent performance if they may do so.

5.3.1 Nanoneedles

The poor solubility of CO₂ in the aqueous solution results in a low concentration of available CO₂ surrounding catalysts, impeding the increase in the CO₂RR efficiency. An approach to overcome this limitation is to use alkali metal cations with enhanced interactions with adsorbed species.^{154, 195} However, their contributions are limited by the solubility of relevant salts. Applying large electrode potentials has also been demonstrated to be able to improve CO₂ adsorption,¹⁹⁶ but the negative potentials will increase hydrogen evolution. A recent report shows that engineering electrode morphology presents a viable method to achieve this goal without sacrificing CO₂RR selectivity. Sargent et al.⁹⁹ studied the effects of Au electrode morphology (needle, rod, and particles) on CO₂ reduction and discovered that nanoneedle can significantly enhance CO₂RR performance than others. The contribution was ascribed to the enhanced local electric fields created by the concentrated electrons on the tip electrode (**Figure 13A**), which shows an order of needles > rods > particles, as confirmed by the Kelvin probe atomic force microscopy (**Figure 13B**). Such an electrostatic field increases the density of surface adsorbed K⁺ ion in the Helmholtz layer around the Au needle (**Figure 13C**), which is proposed in turn to increase the local concentration of CO₂ through non-covalent interactions. However, direct experimental evidence remains lacking; developing methods to measure the local CO₂ concentration is highly needed. With an increase in the local CO₂ concentration, the limitation of CO₂ transportation from the bulk

electrolyte to the surface of Au needle can be significantly diminished. In addition, the locally concentrated electron density also results in an acceleration of charge transfer in CO₂RR, as reflected by the smallest R_{ct} on Au needle.

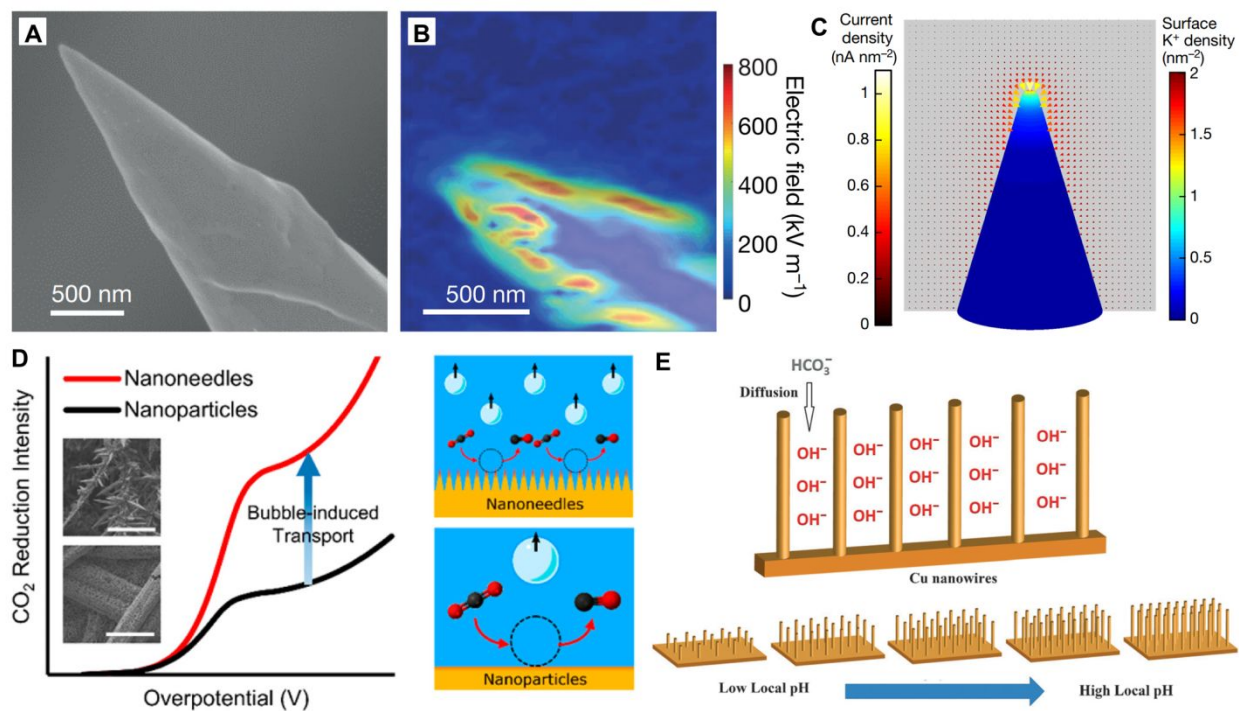


Figure 13. (A) SEM image, (B) Electric field distribution, and (C) Surface K⁺ distributions and corresponding current on Au needles. Adapted with permission from Ref. ⁹⁹. Copyright 2016 Springer Nature Publishing Group. (D) Illustration of the influence of nanoneedles and nanoparticle electrodes on CO bubble departure diameter. Adapted with permission from Ref. ¹⁶⁵. Copyright 2017 American Chemical Society. (E) Schematic of the diffusion of electrolytes into Cu nanowire arrays. Adapted with permission from Ref. ¹⁹⁷. Copyright 2017 American Chemical Society.

The combination of both enhanced mass and charge transfer dominantly boosts the CO₂ reduction kinetics on the Au tip, delivering a Tafel slope of 42 mV dec⁻¹, which is much smaller than 80 mV dec⁻¹ on Au rod and 96 mV dec⁻¹ on Au particle. As for specific activity, the Au needle delivers an ECSA-normalized CO partial current density 63 times and 122 times larger than that on rods and particles, respectively. Thermodynamically, the adsorbed K⁺ ions lower the energy barrier for the formation of *COOH, the potential-limiting step in CO₂-to-CO on Au, resulting in the positive shift of onset potential. Accordingly, Au nanoneedle shows an FE of 95%, a partial current density of 15 mA cm⁻², and an EE of 80% at a low overpotential of 240 mV, which is among the highest result reported to data for Au catalysts (**Table 2**). This suggests that nanoneedle-induced effect might have a larger contribution to CO₂RR than the modification of surface composition²¹ and constructing efficient three-phase interface¹³⁵ and porous structure.⁶⁴ Further, this concept was also successfully confirmed on palladium nanoneedle for reducing CO₂ to HCOOH, suggesting its universality. The control experiments, including annealing, etching, surface coating, plasma treatment, exclude the benefits of the surface faceting and atomic-scale structure to CO₂RR. Thus, it is the morphology that plays key roles in enhancing CO₂RR activity. Future CO₂ reduction is suggested to consider the morphological effects if the catalysts used have locally tip-like feature.

Besides influencing the local reactant concentrations, a study by Sinton et al.¹⁶⁵ revealed that catalysts morphology can also affect gas transport in a long-range (**Figure 13D**). They investigated the CO evolution on Au nanoneedles, nanorods, and nanoparticles surface using a dark field microscope, which points to an interesting phenomenon that CO bubbles on Au nanoneedles show

a smaller diameter (23 μm) than that on nanorod (31 μm) and nanoparticle surfaces (97 μm). Due to the small bubble-induced rapid releasing of CO, sharper Au needle exhibits a 4-fold larger current density than the nanoparticle counterpart. In another study, Smith et al.¹⁹⁷ found that adjusting the length and density of Cu nanoneedle (nanowires, NW) could regulate the local pH. The longer and denser Cu NW arrays can slow down the transportation of HCO_3^- into the Cu NW arrays and the flow of OH^- out of the Cu NW arrays (**Figure 13E**), which leads to a high local pH near the Cu NW surface. The enhanced interfacial alkali environment improves the selectivity for generating C_2 and C_3 products (C_2H_4 , C_2H_6 , $\text{C}_2\text{H}_5\text{OH}$, and $\text{C}_3\text{H}_7\text{OH}$) via a preferred CO dimerization pathway, whereas shorter and sparser arrays had a low local pH favoring H_2 evolution.

5.3.2 Nanocavity

CO_2 reduction proceeds through multiple elemental reaction steps, involving different intermediates being generated and consumed. Thereby, the local concentration of intermediates could serve as a parameter to tune product selectivity, which, however, is difficult to be well controlled. Zhuang et al.¹⁶⁷ demonstrated a nanocavity-induced synthesis of C_3 alcohol fuels from electrochemical CO reduction. Given that the C_3 formation takes place via C–C coupling between C_2 and C_1 intermediates (**Figure 14A**), they proposed that a nanocavity could potentially concentrate C_2 species via steric confinement and thereby limit the desorption of C_2 intermediates and promote the C–C coupling between C_2 and C_1 intermediates to increase C_3 production (**Figure 14B**). The finite-element simulations indicate that the cavity efficiently inhibits the outflow of C_2 species produced from CO reduction (**Figure 14C**, arrows), resulting in a higher local C_2

concentration inside the cavity. Because of the increased surface coverage of C_2 intermediates, the chance for the combination of C_2 and CO was increased, generating a heightened C_3 production rate inside the cavity (**Figure 14D**). With the preparation of Cu with the same surface compositions but varied morphology from solid, Cavity I (with small cavity opening angles about 30°), and Cavity II (with large cavity opening angles about 60°) (**Figure 14E**), it was demonstrated that Cavity II shows the highest FE for C_3H_7OH generation compared to others (**Figure 14F**). The lowest FE of C_2H_4 on Cavity 2 confirms that C_2H_4 acts as the intermediate being transferred into C_3H_7OH inside of the cavity. Also, the experimental C_3/C_2 ratio is in good agreement with theoretical simulation (**Figure 14G**). Note that although this work focused on CO reduction, it might be applicable for CO_2 reduction as CO is a first-order product in CO_2RR . Considering that reducing CO_2 into C_3 products is more valuable but faces grand challenges, this nanocavity approach may provide a viable route to achieve this goal.

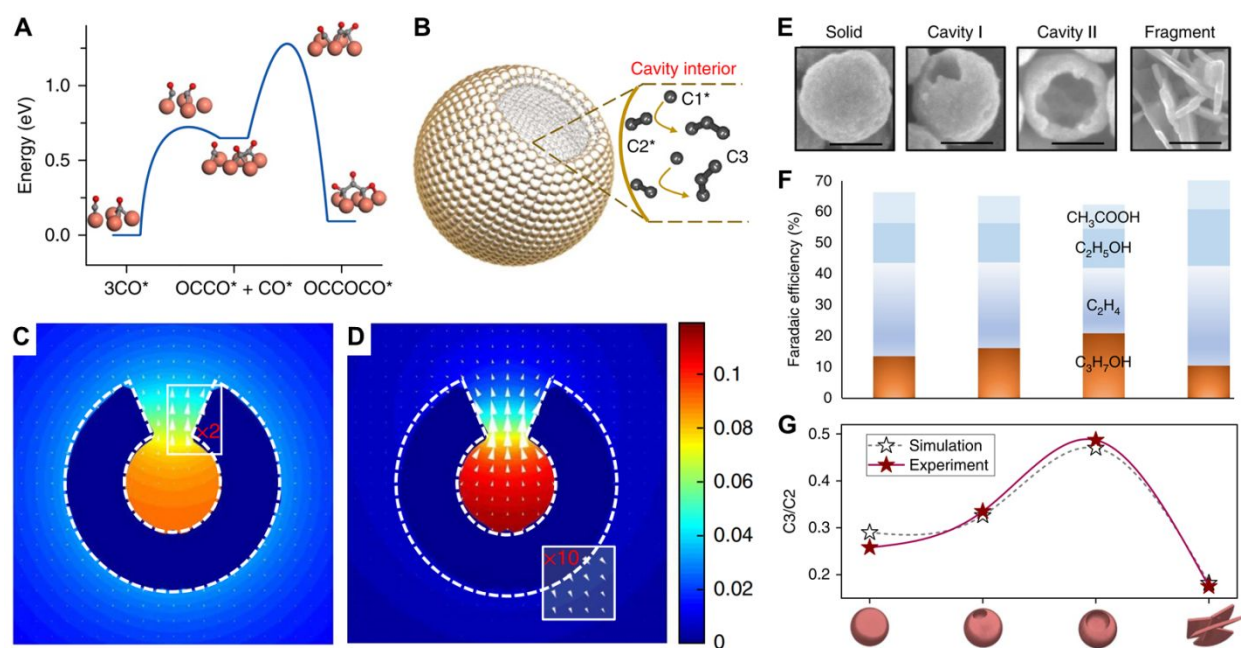


Figure 14. (A) Energy profile for the formation of C_3 intermediate. Red, grey, and orange balls present O, C, and Cu, respectively. (B) Schematic showing that the cavity confinement effect boosts C_2 species binding and further conversion to C_3 . (C, D) C_2 and C_3 concentrations and flux distributions in the cavity. (E) SEM images of model catalysts with variable morphologies. Scale bars, 100 nm. (F) FEs of C_2 and C_3 products on model catalysts at -0.56 V vs. RHE. (G) The experimental and FEM simulation results of C_3/C_2 product selectivity. Adapted with permission from Ref.¹⁶⁷. Copyright 2018 Nature Publishing Group.

5.3.3 Mesopores

Mesopores possess many intriguing features, such as large surface area and continuous porous channel, which could potentially increase the accessibility of active sites and mass transportation for reactant, intermediates, and products.¹⁹⁸⁻²⁰⁰ These unique properties make mesoporous materials suitable electrodes for electrochemical reactions, such as mesoporous carbon. The existing findings show that pristine carbon is inert toward CO_2RR due to the electroneutrality. Chemical doping is an effective way to transform carbon into active catalysts for CO_2 reduction by incorporating heteroatoms (such as N, B, F, S) to break electronegativity to create charged sites for the adsorption of CO_2RR intermediates. The transitional ways to tune CO_2RR activity of heteroatoms-doped carbon rely on tuning the atomic contents, heteroatoms type, and dopant configurations.²⁰¹⁻²⁰³

Remarkably, Janaky et al.¹³⁸ discovered that morphological attributes (e.g. porosity, pore size) can influence the CO_2 reduction performance of nitrogen-doped carbon (NC) catalysts (**Figure**

15A). A sacrificial hard-templating method was used to prepare porous NC having pore size varying from 13 nm to 27 nm and 90 nm (**Figure 15B**), and the pore-deficient NC was also prepared without using hard templates as a reference control. The exact synthetic condition leads to the close atomic contents of N atoms, N dopant configurations, carbon graphitization degree, and defects on both porous and pore-deficient NC. This guarantees that the difference in CO₂ reduction performance can be mainly attributed to the pore-induced morphological effect. It was found that flat NC dominates hydrogen evolution, while porous NC presents significantly higher selectivity and production rates for CO generation. Among them, CO₂ reduction activity follows the sequence of NC-27 > NC-13 > NC-90 (27, 13, and 90 refer to the pore size).

The difference in catalytic behaviors has been attributed to the wettability, CO₂ adsorption, exposure of N dopants, and curvature effects, all of which are highly dependent on porous structure. Firstly, mesopore decreases the surface energy. Mesoporous NC shows surface energy of 2 mJ m⁻², three times smaller than that of the flat surface, generating a more hydrophobic surface on mesoporous NC. This prevents NC from being overflowed, which helps to maintain a high local pH (a low concentration of proton) and thus suppress HER.¹³⁵ Secondly, CO bubble residence time on porous N-C is drastically lower as compared to the nonporous N-C. Both the diameter and stay time decrease with reducing the pore size. The small bubbles, which depart from the electrode surface quickly, can readily expose the fresh surface leading to a high current density. Thirdly, mesopore could significantly increase the effective number of active sites by exposing N dopants and their accessibility to CO₂. Lastly, porous NC exhibited higher CO₂ adsorption than flat NC, showing a higher desorption temperature on porous NC relative to that on pore-free NC, as

manifested by the temperature-programmed desorption (TPD) (Figure 15C). Such effect was proposed to be from the curved surface-induced strain, which increases CO₂ adsorption strength on porous NC. The effect has also been manifested by computational modeling.²⁰⁴ Besides CO₂ adsorption, the importance of curved adsorption site in ORR was also observed on NC, suggesting that building pores could be a general method to tune electrocatalytic behavior of NC materials for a broad application. These benefits collectively contribute to the enhanced CO generation on porous NC as compared to the pore-free counterpart. Note that curved pores may also contribute to a higher ratio of edge versus plane locations in comparison with the flat surface, of which N dopants may have various intrinsic reactivity. However, whether the curvature affects the catalytic nature of N dopants remains controversial and yet unresolved.

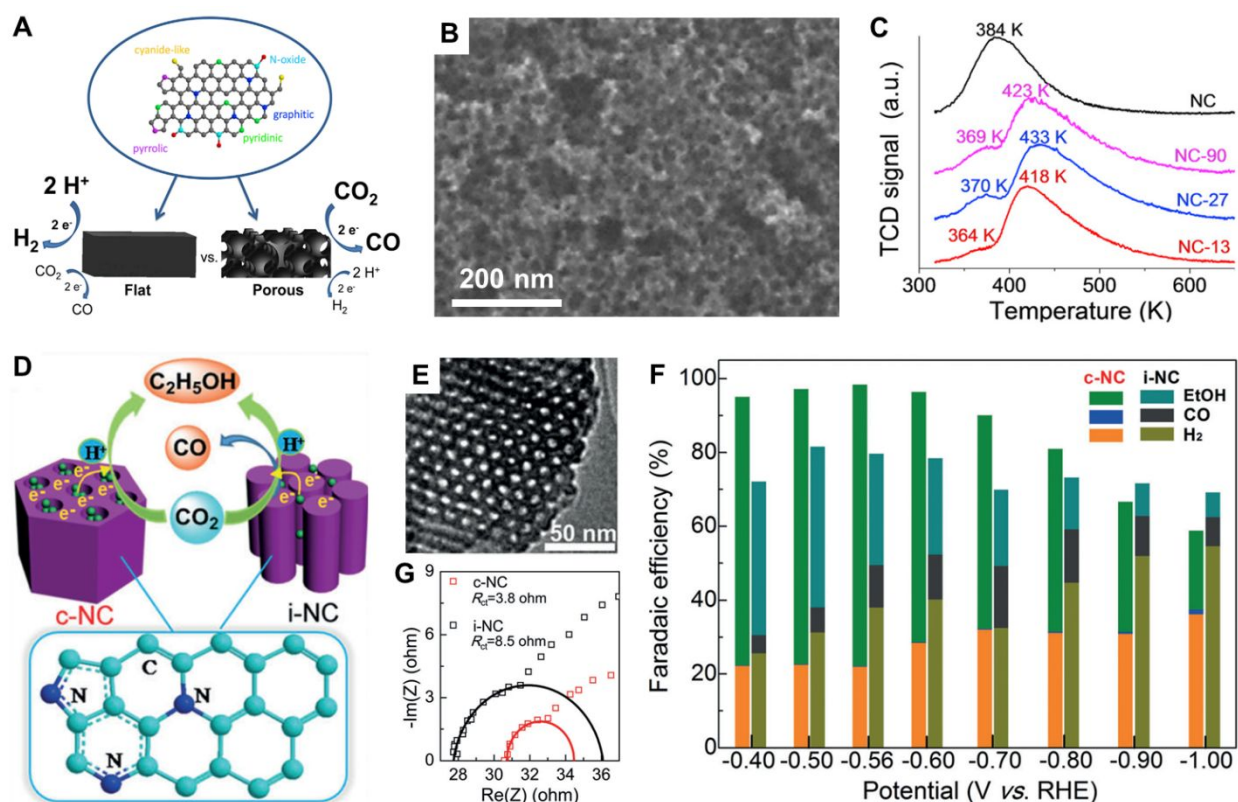


Figure 15. (A) Schematic showing activity difference on flat and porous NC. (B) TEM image of NC-27. (C) TPD profiles for CO₂. Adapted with permission from Ref.¹³⁸. Copyright 2018 Elsevier. (D) Schematic of c-NC and i-NC for CO₂RR. (E) TEM images for c-NC. (F) FEs and (G) EIS at -0.56 V in CO₂RR over c-NC and i-NC. Adapted with permission from Ref.¹³⁴. Copyright 2017 Wiley.

Generally, NC materials were merely found to produce C₂ products because the binding strength of CO on the N dopant sites is too weak to adsorb on NC.¹³⁷ This leads to the facile desorption of CO from the catalyst surface and reduces the possibility for *CO dimerization, thus permitting enhanced CO selectivity while impeding further transformation into C₂₊ products. Surprisingly, ordered mesoporous NC was found to be able to generate C₂H₅OH with high FEs (**Figure 15D**). In specific, Sun et al.¹³⁴ demonstrated that the ordered mesoporous NC with a cylindrical channel (denoted as c-NC, **Figure 15E**) primarily yields C₂H₅OH in terms of high FEs ranging between 73% and 77% under the potential region of -0.40 V ~ -0.56 V and negligible FE of CO. Moreover, c-NC exhibited improved stability, maintaining an FE of 77% and an EE of 45% in 24 hours reaction at an overpotential of 0.63 V. It should be pointed out this was the first work achieving such high C₂ product selectivity on NC materials, despite the low current density of 0.15 mA cm⁻² that should be further improved.

The authors also found that the selectivity of C₂H₅OH depends largely on the shape of mesopore. The cylindrical c-NC performs better than i-NC which possesses inverse channels; i-NC shows a larger FE for CO (16%) but a lower FE (44%) for C₂H₅OH as compared to those of

c-NC (**Figure 15F**). The superiority of c-NC stems from its unique cylindrical channels configuration, which do much better to electron transfer than the inverse channels, as manifested by smaller R_{ct} on c-NC than i-NC (**Figure 15G**). Therefore, the transfer of electrons to the active N species of c-NC was dramatically elevated, yielding high-density electrons on the surface of the porous channel over c-NC. Such an electron-rich surface made a considerable contribution in stabilizing $*CO$ intermediate and inhibiting its desorption to generate gaseous CO, thereby facilitating the dimerization of $*CO$ intermediates into $OC-*CO$ and subsequent multiple PCET processes to generate $OC-*COH$ intermediate and final C_2H_5OH on N dopants sites. The pore shape-induced promotion of C_2 selectivity paves a visible way to boost the C–C bond formation in CO_2RR . However, how pore shape influences the mass transportation of intermediates, bubble behaviors, and surface wettability needs to be further investigated, all of which could make a huge difference to the final product distribution, as discussed in the previous sections.

In another study, Ajayan et al.¹⁵¹ reported that the nanometer-sized N-doped graphene quantum dots (NGQDs) can electrochemically reduce CO_2 into C_2H_4 and C_2H_5OH with a total FE of 45% at -0.75 V, whereas N-doped reduced graphene oxide (NRGOs) with micrometer size cannot do so. The virtue of NGQDs was mainly ascribed to the high density of pyridinic N sites for facilitating the C–C bond formation. However, the high percentage of pyridinic N may not be the sole reason for switching CO_2RR selectivity between NGQDs and NRGOs because Tan et al.²⁰⁵ found that the pyridinic N prefers to reduce CO_2 to $HCOOH$, instead of C_2 products. Inspired by aforementioned pores-induced selectivity tuning,¹³⁴ it is possible that the size effects could be additional causes accounting for enhanced C_2 selectivity on NGQDs.

In addition to tune catalytic selectivity, mesopores can also help to preferentially increase the density of edge-located sites because they can create a large number of edge locations when placing them throughout the 2D plane. In the 2D graphene, N dopants mostly accommodate at the basal plane forming graphitic N owing to a high bulk-to-edge ratio;^{203, 206, 207} selectively incorporating edge-hosted pyridinic N in graphene is a grand challenge. Pan et al.¹³⁷ developed N,F-codoped holey carbon layers to load a dense distribution of pyridinic N (NF-HCL) (**Figure 16A**). In NF-HCL, the through-plane holes provide abundant edges to preferentially host pyridinic N while suppressing the formation of graphitic N. This was confirmed by N 1s X-ray photoelectron spectroscopy (**Figure 16B**), in which NF-HCL shows an overwhelming percentage of 72% for pyridinic N and a low portion of 23% for graphitic N, while the hole-free N-doped carbon layer (N-CL) shows a dominant graphitic N (52%). The dense F-activated pyridinic N endows NF-HCL with a CO FE of 90% at a low overpotential of 490 mV for 40 h without decay, significantly surpassing the pore-deficient N-C counterpart. This concept has also been demonstrated on the SnO₂ layer for HCOOH generation (**Figure 16C**). When mesopores are introduced into the SnO₂ layers, the formation of grain boundaries (GBs) between nanoparticles can be improved as mesopores inhibit the growth of large grains (**Figure 16D**).²⁰⁸ The close contact between small SnO₂ nanoparticles forms dense GBs, giving rise to significantly larger current on mp-SnO₂ than Sn foil.

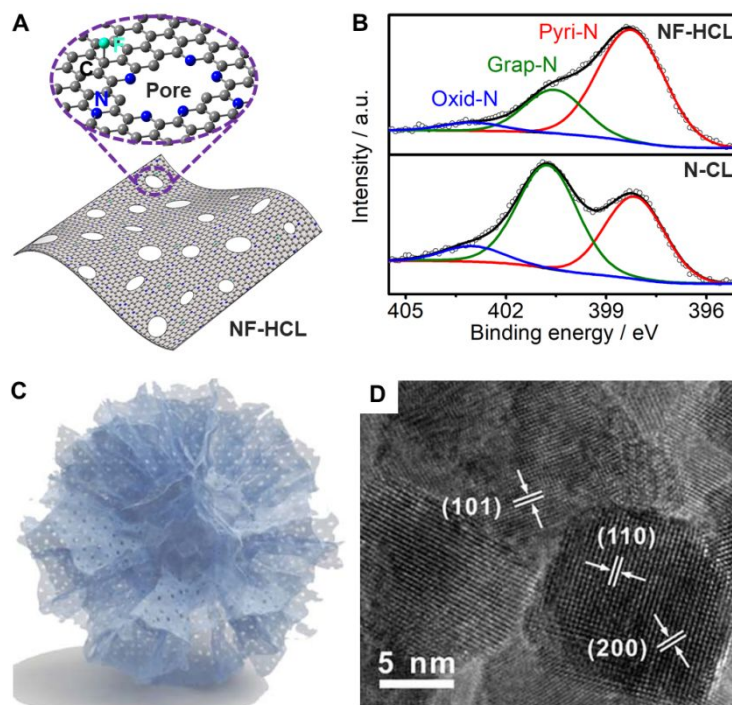


Figure 16. (A) Schematic of NF-HCL with dense pyridinic N on the edges of mesopore. (B) N 1s XPS spectra of NF-HCL and N-CL. Adapted with permission from Ref.¹³⁷. Copyright 2019 American Chemical Society. (C) Schematic and (B) high-resolution TEM image of mp-SnO₂. Adapted with permission from Ref.¹⁴⁵. Copyright 2019 RSC.

5.3.4 Hierarchical porous nanocage

Due to the low solubility of CO₂ and poor electron/mass transportation in the CO₂ reduction process, CO₂RR commonly has slow kinetics and exhibits poor selectivity and low partial current density at large overpotentials, where HER heavily competes with CO₂RR. An efficient CO₂ reduction catalyst should be engineered to have both highly exposed active sites and fast electron and mass transport. Generally, it is challenging to achieve these requirements in one catalyst. Hierarchical porous morphology could achieve this goal due to the following merits of hierarchical

pores. Macropores can provide a high-volume buffer for electrolyte ions, beneficial to shorten the ion diffusion distance; mesopores can serve as diffusion channels for the fast mass transport; micropores can enhance the specific surface area.^{171, 209-211} Ni et al.¹³⁹ synthesized F-doped hierarchically porous nanocage (F-CPC) to realize the above-mentioned merits. As shown in **Figure 17A**, F-CPC shows a cage-like feature with a mesopore-rich thin carbon shell. As controls, (F-CS) without shell, and were also prepared. Notably, F-HCS achieves a maximum FE of 88%, a high current density of 37 mA cm^{-2} , and an EE of 53% for CO generation at an overpotential of 890 mV (**Figure 17B**), much better than those observed on F-doped solid carbon spheres F-CS, F-doped hollow carbon spheres without mesopores on the carbon shell (F-HCS), and F-doped commercial carbon (F-PC) with irregular pores (F-PC).

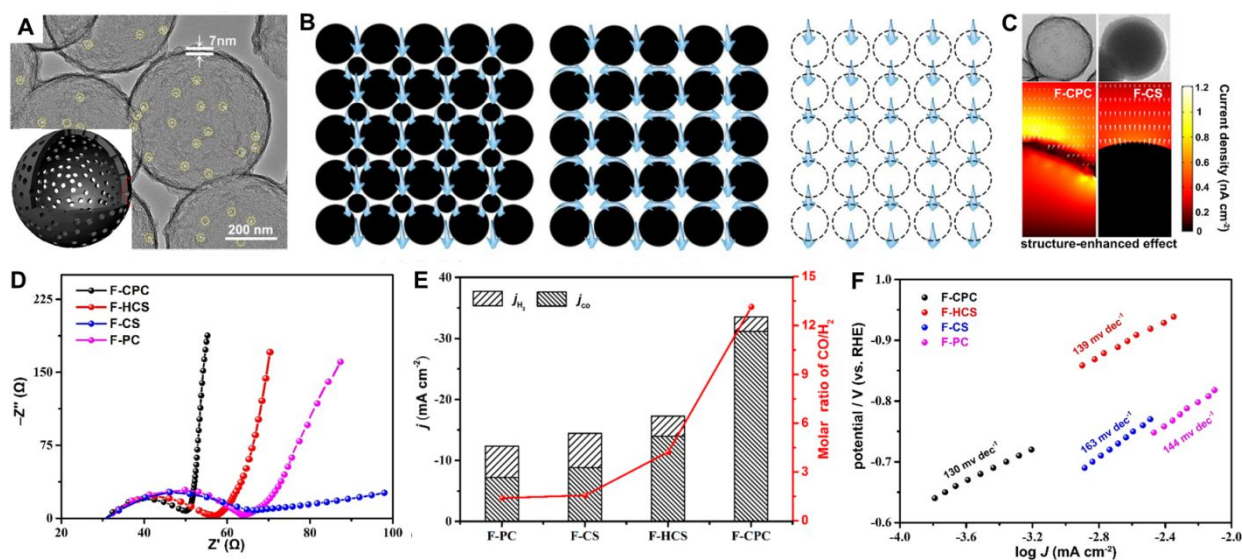


Figure 17. (A) TEM image of F-CPC. Insert shows the schematic structure. (B) CO₂RR performance of various catalysts at -1.0 V . (C) Nyquist plots. (D) Schematic illustration of concentrated K⁺ cations on F-CPC. (E) Schematic diagrams of possible CO₂ migration pathways

on F-CS and F-CPC. (F) Tafel plots in CO₂-saturated KHCO₃ electrolyte. Adapted with permission from Ref.¹³⁹. Copyright 2020 American Chemical Society.

The enhanced CO₂RR performance was proposed to be resulted from CPS-induced enhanced CO₂ reduction kinetics at large overpotentials. Firstly, F-CPS possesses the highest surface area, which endows F-CPS with the highest ECSA, as manifested by the largest double-layer capacitance (C_{dl}). Secondly, F-CPS shows the fast electron transfer during CO₂RR than others, which was revealed by the lowest R_{ct} value measured by EIS (**Figure 17C**). Thirdly, F-CPC displays an enhanced electric field on the shell of hierarchically porous nanocage, which induces a high concentration of K⁺ cations and in turn leads to a high local concentration of CO₂ (**Figure 17D**). Lastly, the F-CPC electrode owns fast mass transport and lower diffusion resistance due to the highly porous networks (**Figure 17E**). The diffusion time of CO₂ molecules calculated by finite element simulations is 0.63 s on F-CPC, apparently smaller than that of 0.89 s on F-CS and 1.53 s on F-PC. These integrated advantages contribute to accelerating CO₂RR kinetics, as reflected by the lowest Tafel slope on the F-CPC electrode (**Figure 17F**). This design could be a guideline to prepare hierarchical porous nanocage copper and SnO₂ for further improving their activity to reduce CO₂ to C₂ and HCOOH products, respectively.

5.3.5 Crystalline porous frameworks

Crystalline porous frameworks, such as covalent organic frameworks (COFs) and metal-organic frameworks (MOFs), are one kind of highly ordered crystalline polymers assembled from organics ligands and/or metal nodes via reticular chemistry.^{212, 213} In recent years, they have been

emerging catalysts for CO₂ reduction thanks to the high manageability to decorate active sites by adjusting ligands or adding functional groups at a molecular level,²¹⁴⁻²¹⁷ which is difficult for other heterogeneous catalysts. However, there is an inherent drawback that COFs/MOFs commonly show low electrical conductivity due to the poor intermolecular electron transmission and/or lack the oriented electron transfer route.

Lan et al.²¹⁸ proposed an effective approach to address this drawback by combining electron donor and acceptor in one COFs based on metalloporphyrin-tetrathiafulvalene COFs (M-TTCOFs) (**Figure 18A**). In the system, tetrathiafulvalene (TTF), having high electron mobility, serves as the electron donor, and metalloporphyrin, possessing conjugated π -electron structure, functions as the electron acceptor and catalytically active site. Integrating TTF with metalloporphyrin thus constructs a smooth electron transmission pathway from TTF to metalloporphyrin (**Figure 18B**), enhancing the electron transfer efficiency to active center. It was found that Co-TTCOFs shows the highest charge transfer capability with a smaller R_{ct} (23.4 Ω) than Ni-TTCOF (191.5 Ω) and H₂-TTCOF (111.9 Ω). This results in more favorable kinetics on Co-TTCOF, showing a smaller Tafel slope of 237 mV dec⁻¹ as compared to Ni-TTCOF (629 mV dec⁻¹) and H₂ TTCOF (433 mV dec⁻¹). Note that, although the different intrinsic reactivity between Co and Ni sites may contribute to their performance difference,²¹⁸ the efficient charge transfer was believed to play a key role in promoting CO₂RR kinetics.

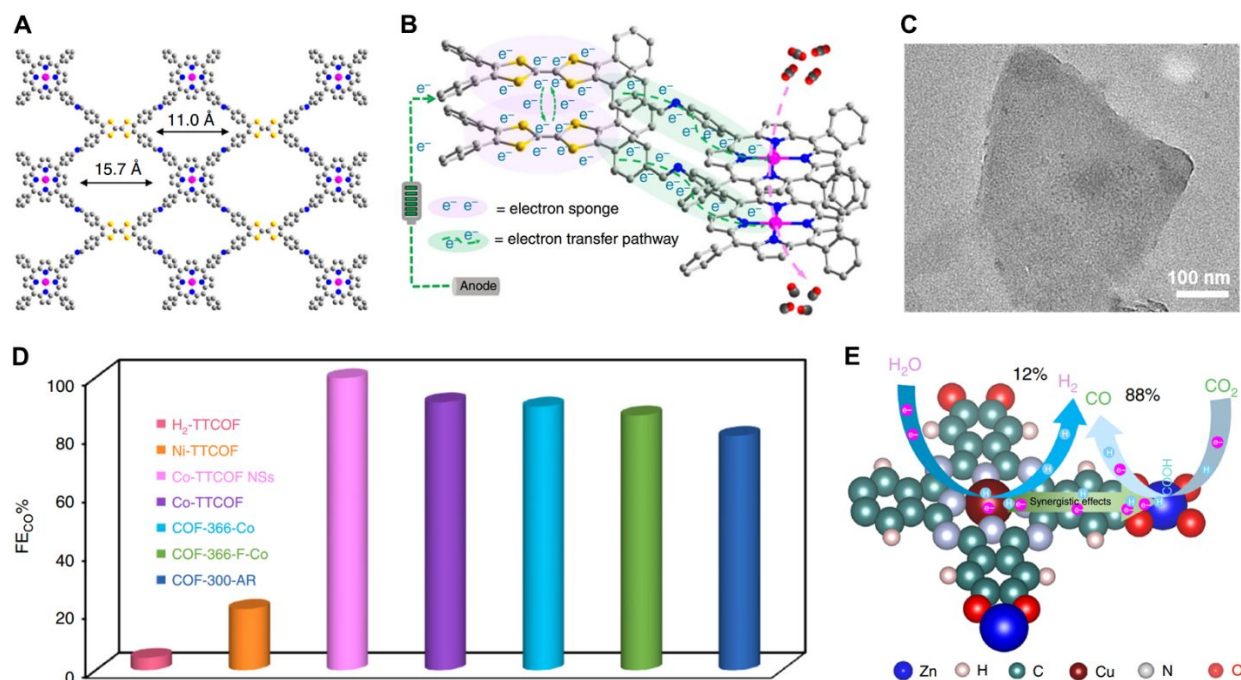


Figure 18. (A) Structure of Co-TTCOFs. (B) Schematic showing the electron transfer mechanism on Co-TTCOFs. (C) TEM image of exfoliated Co-TTCOFs NSs. (D) FEs comparison between Co-TTCOFs with ones reported in the literature. Adapted with permission from Ref.²¹⁸ Copyright 2020 Nature Publishing Group. (E) The proposed synergistic catalytic scheme on MOF CuN₄ and ZnO₄. Adapted with permission from Ref.²¹⁹ Copyright 2018 Nature Publishing Group.

COFs/MOFs, composed of organic molecules with small sizes, mostly have microporosity. In electrocatalysis, the micropore is generally not good for the transportation of reactant to active sites embedded in the bulk of closely packed COFs/MOFs, resulting in the low density of effective active sites. Exfoliation of original bulk crystals could potentially increase the exposure of catalytic centers and thus their utilization efficiency. As reflected by Lan et al.'s work,²¹⁸ Co-TTCOFs were transferred to 2D nanosheets through a high-frequency sonication approach, showing a size of

~500 nm and a thickness of around 6 nm (**Figure 18C**). The exfoliated Co-TTCOFs NSs delivered a maximum CO FE of 99.7% (**Figure 18D**), higher than the unexfoliated one (91.3%) and reported COFs, such as COF-366-Co (90%),²¹⁴ COF-366-F-Co (87%),²²⁰ and COF-300-AR (80%).²²¹ However, the overall current density on 2D nanosheets was not given, which is suggested to be further investigated to reveal the contribution of 2D sheets in increasing currents as compared to bulk crystals.

MOFs-based materials face the same issue as to COFs in electrocatalysis. To promote the charge and proton transfer in CO₂RR, Feng et al.²¹⁹ proposed a synergistic bimetallic conjugated MOFs, consisting of copper-phthalocyanine (CuN₄) as the ligand and zinc-bis (dihydroxy) complex (ZnO₄) as the linkage. As depicted in **Figure 18E**, the ZnO₄ complex serves as the catalytic site for CO₂RR while the CuN₄ unit boosts the transfer of proton and electron to ZnO₄. In specific, CuN₄ can attract numerous electrons and H₂O to produce abundant protons. The transfer of electrons and protons from CuN₄ to ZnO₄ thus accelerates the protonation of adsorbed CO₂ on the ZnO₂ site to *COOH. The subsequent PCET-assisted dissociation of *COOH results in the formation of *CO and final gaseous CO. The activity comparisons further manifest that a smaller charge transfer resistance gives rise to faster reaction kinetics.

Despite these advancements, grand challenges still exist for COFs/MOFs in CO₂RR. Firstly, future research should carefully evaluate the stability of COFs/MOFs,^{222, 223} and developing stable COFs/MOFs is imperative. A report shows that the coordination of Zn²⁺ (or Co²⁺, Cu²⁺) with 1,3,5-benzenetricarboxylic acid (H₃BTC) and 2-methylimidazole (HMIM) underwent the decomposition at a potential around -1.0 vs. RHE with the reduction of metal ions to metallic

particles in CO₂-saturated 0.5 M NaHCO₃ aqueous.²²³ This raises concerns about electrochemical stability under large overpotentials. Secondly, hierarchical porous COFs/MOFs with mesopores and/or macropores are recommended to be applied for CO₂RR to further improve their performance because of their premium merits to boost mass transportation that micropores could hardly offer. Many useful approaches to prepare mesoporous and macroporous MOFs have been developed, such as templating and post-treatment (hydrolysis, thermolysis),²²⁴ which are welcomed to be employed to prepare hierarchical MOFs/COFs for CO₂RR. Thirdly, COFs/MOFs-catalyzed CO₂RR is suggested go further to C₂₊ products. Currently, COFs/MOFs show high selectivity for C₁ products with FEs more than 90% for CO and HCOOH,^{214, 218, 219} while selectivity for C₂₊ products is still low, such as a FE of 19% for CH₃COOH on Cu₂(CuTCPP)²²⁵ and a FE of 45% for C₂H₄ on HKUST-1.²²⁶ The morphological engineering could offer bright future to achieve high selectivity for C₂₊ products on COFs/MOFs, such as constructing cavity and tuning pore shape which have been demonstrated to be able to promote C₂ generation on copper and carbon-based catalysts, as discussed in subsection 5.3.2 and 5.3.3.

5.3.6 Porous thin film

Porous thin film has gained attractive attention in electrocatalytic applications because of the unique free-standing merit that powder materials could not have, which avoids the use of polymer additive. The initial study using porous thin-film catalysts for CO₂RR focused on Cu foam with hierarchical porosity prepared by the electrodeposition methods. Palmore et al.²²⁷ found that Cu foam shows higher a FE for HCOOH and lower FEs for CO, CH₄, and C₂H₄ as compared to those

on smooth Cu. The catalytic difference was attributed to the exposure of (211) facet that shows a low free energy barrier for the formation of HCOO^* , a key intermediate to produce HCCOH . In another study, Broekmann et al.¹⁴⁷ discovered that Cu foam preferentially produces C_2H_4 and C_2H_6 instead of CO while flat Cu film has an overwhelming CO selectivity. The authors attributed the higher C_2 selectivity to the combination of the exposed (100) facet and the trapping of CO inside the pores of Cu foam. The (100) facet has enhanced inherent reactivity for C–C coupling, and the trapped CO increases CO coverage and in turn promotes the $^*\text{CO}$ dimerization. Note that, in these Cu foam cases, the catalytic performance was governed by both the electronic effect from exposed facets and the morphological contribution from the pores.

To study the exclusive effect of mass transport at the microscale in a porous thin film for CO_2RR , the film should be engineered to have the similar compositions, facet, and surface groups to preclude atomic and/or nano scale electronic structure's interference. Surendranath et al.¹³⁶ prepared a series of Ag inverse opal (Au-IO) films with ordered pores (200 nm size) and various thickness from 1.7 to 6.2 mm (**Figure 19A**), which have similar surface electronic properties and be ideal models to explore the effects of film thickness toward CO_2RR . Electrode roughness (RF), calculated by dividing ECSA by geometric area, was employed as an activity descriptor. Note that the values of ECSA and RF are dependent only on the thickness of the film as the surface composition and pore structure in thickness-different films are the same. Thereby, the RF presents the same meaning to that of the thickness of the film, and a larger RF presents a thicker film.

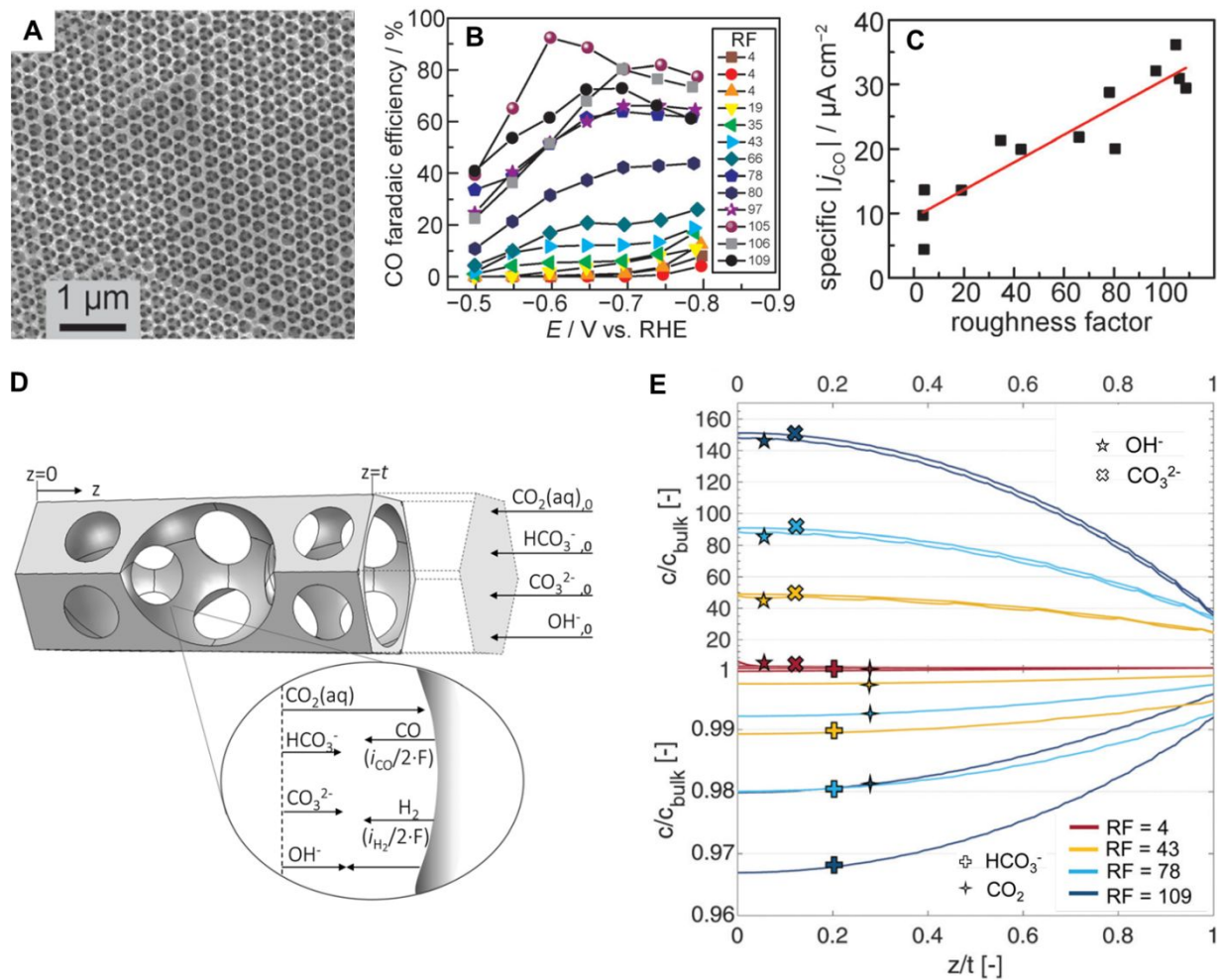


Figure 19. (A) SEM image of an Ag-IO film. (B) CO FEs and (C) ECSA-normalized CO current of Ag-IO film with varied RF. Adapted with permission from Ref.¹³⁶. Copyright 2016 Wiley. (D) Mass transport model on Ag-IO. (E) Calculated concentration profiles of different species along the z-axis vs their bulk concentration at a potential of -0.8 V vs. RHE. Adapted with permission from Ref.²²⁸. Copyright 2019 RSC.

Interestingly, it was discovered that there is a general increase tendency in CO selectivity (**Figure 19B**) and ECSA-normalized currents (**Figure 19C**) when gradually increasing electrode RF from 4 to 105, while the selectivity and specific current for HER decline. These results

demonstrate that adjusting the thickness of porous films can tune CO₂ reduction behaviors. Note that a thicker film does have a larger exposed density of active sites, but the enhancement in ECSA-normalized specific current manifests that the density of active site is not the reason for improved activity. The investigation of the susceptibility to mass transportation shows that HER is highly sensitive to the mass transport limitation than CO₂RR. Different to the flat electrode, the influences of mass transportation in the high-porosity electrode will be amplified due to the convective flow of reagents inside the porous electrode. It was thus postulated that the suppression of HER upon increasing thickness is resulted from the depletion of the local H⁺ (high pH) due to the poor mass transportation from the bulk solution to pores.

Although the observation of film thickness-induced activity modulation is inspiring, it is hard to experimentally measure the actual concentration of CO₂ and electrolyte ions inside the pore. Such a situation becomes more complex under the real CO₂RR condition as the change of local OH⁻ will lead to the dynamic shift of the equilibria between HCO₃⁻ and CO₃²⁻ in the buffer solution. Theoretical computation can provide information on mass transport taking place inside the pores at the microscale level. Haussener et al.²²⁸ developed a finite element numerical model to predict the concentration of various species involved in CO₂RR on an Au-IO film electrode. The electrode was constructed using the same parameters of Au-IO reported by Surendranath et al (**Figure 19D**).¹³⁶ The $z=0$ means the bottom of the film and the $z=t$ refers to the planar surface of the film. The predicated activity indicates that CO FEs and current densities increase with increasing RF (thickness), consistent with experimental findings.¹³⁶ The calculated distribution of species shows that the concentrations of OH⁻ and CO₃²⁻ in the deepest pores are substantially higher than those

towards the bulk electrolyte (**Figure 19E**); such a tendency is more obvious in the thicker film. However, the concentrations of both CO_2 and HCO_3^- are not significantly affected by the film thickness because the relatively low reaction rate will not cause the limitation of CO_2 transportation. The enhanced OH^- provides a favorable reaction environment with a low concentration of H^+ suppressing HER, and the increased local amount of CO_3^{2-} is also hypothesized to promote CO evolution.²²⁹ However, the correlation between CO_3^{2-} and CO generation remains not well-understood and needs to be further studied.

From the theoretical predication, one can assume that adding a diffusion layer on the top of Au-IO can boost CO evolution. Note that the additional layer could be inert materials but has the same porosity to the film. This knowledge is very important for practical application from a cost perspective. Nevertheless, the current research is limited to the CO-active catalysts, and whether this configuration can be applied to boost C_{2+} products on the Cu-based electrodes needs further investigation. In addition, how exactly the disordered pores could influence CO_2RR species in the film electrode is unclear, and the evolution and detachment of bubbles inside of pores remains unknown too. Moreover, the overall CO_2 electrolysis needs to consider the transportation of species between cathode, anode, membrane, and bulk electrolyte, therefore the macroscale mass transportation behaviors should be further studied to evaluate the porous thin film's benefits in the full electrolysis level.

5.3.7 Other morphology

Nanoparticles (NPs) are one kind of classic catalysts in various catalytic applications because of the high surface-to-volume ratio and tunable surface sites. Previous efforts on tailoring the CO₂RR activity of NPs mainly focused on exposing favorable facets and edge/corner sites. In a different way, Cuenya et al.¹⁹⁰ investigated the relationship between the interparticle distance of Cu NPs and CO₂RR activity. A short interparticle distance of large Cu NPs was found to play a crucial role in promoting the re-adsorption of CO intermediates from one NPs to a neighboring NPs and their further reduction to CH₄ and C₂H₄, while small Cu NPs suffer from active-site poisoning by CO. This finding uncovers a general principle to tailor NPs activity via adjusting distance between NPs.

Carbon nanotube (CNT), possessing high electrical conductivity, has been widely used as catalyst support to promote electron transfer. Taking cobalt phthalocyanine (CoPc) as an example, it was theoretically predicted to be a proper catalyst for the reduction of CO₂ to CH₃OH due to the moderate adsorption of *CO on the Co site, whereas this was scarcely realized experimentally. Surprisingly, anchoring CoPc on carbon nanotube was demonstrated to render CoPc a good catalyst for reducing CO₂ to CH₃OH with an FE of 40 % and a current density of 10 mA cm⁻² at -0.94 vs. RHE in the aqueous solution.¹²⁸ Because of the inert nature of pristine CNT, the enhanced activity was primarily ascribed to the benefit of highly conductive CNT, which enables a fast and continuous electron transfer to the active Co site and boosts the multiple electrons reduction of *CO into CH₃OH.

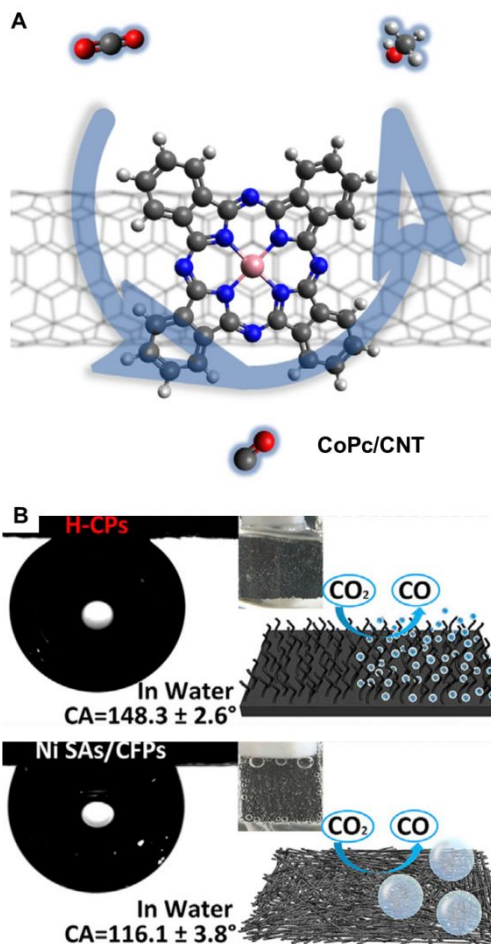


Figure 20. (A) CNT supported CoPc promotes CO₂-to-CH₃OH conversion. Dark grey, blue, light grey, and pink balls represent C, N, H, and Co atoms. Adapted with permission from Ref.¹²⁸. Copyright 2020 Springer Nature Group. (B) Underwater gas bubble contact angles and schematic illustration showing gas detachment behaviors on aligned H-CPs and random Ni SAs/CFPs. Adapted with permission from Ref.¹⁴⁰. Copyright 2019 Elsevier.

Materials surface wettability can also be adjusted by engineering their architecture. Vertically aligned carbon fiber arrays were found to show a superaerophobic surface.¹⁴⁰ As depicted in **Figure 20B**, supporting atomically dispersed Ni on aligned carbon fiber (H-CPs) shows a gas

contact angle around 148.3° under water, implying a superaerophobic property. This results in the generation of small CO bubbles and their facile detachment. By contrast, randomly distributed carbon fiber supported single-atom Ni (Ni SAs/CFPs) gives a gas contact angle of 116.1° , which is detrimental to the desorption of CO due to the gas accumulation to large bubbles. The benefit endows H-CPs with a CO current density of more than three times larger than that of H-CPs at -0.9 V vs. RHE.

6. Summary and perspectives

Electrochemical conversion of CO_2 into fuels and chemicals offers a promising route to mitigate global warming and energy crises caused by the extensive combustion of fossil fuels. The realization of efficient CO_2 electroreduction relies on the exploration of CO_2RR mechanisms and the development of advanced electrode materials and electrolyzers. Although modifying catalysts' electronic properties of catalytically active sites has been widely employed to regulate CO_2RR performance, the linear scaling relation limits the catalyst refinement to achieve the expected performance before it can be broken. Alternatively, CO_2RR is largely susceptible to the local microenvironments. In this Review, we provide fundamental interpretation, design principles, and recent advancements on fabricating electrode catalysts toward CO_2RR via tailoring their local morphology, surface hydrophobicity, and three-phase boundary. Despite the fruitful progresses have been made, there still exists grand challenges, requiring extensive efforts to further explore this new frontier to boost the practical implementation in CO_2 electrolysis technology. Herein, we will discuss the remaining challenges and recommend potential strategies in this research topic.

1) Uncover fundamental mechanisms. Understanding CO₂RR mechanisms could provide useful guidelines to design highly active and selective catalysts. However, the current knowledge remains ambiguous and under debate. For example, whether CO₂ is directly reduced or bicarbonate anion serves as the dominant source?^{230, 231} What is the exact role of metallic Cu and positively charged Cu in the C–C bond formation and hydrogenation process? What are the catalytically active sites of heteroatoms-doped carbon catalysts (dopants or defects)? The main experimental method used to explore CO₂RR mechanisms is the ex-situ characterization of catalysts before and after CO₂ reduction (TEM, XAS, XPS, etc.). These ex-situ approaches cannot catch important information in the real CO₂RR process, during which surface reconstruction, morphological transformation, and active sites evolution/annihilation usually happen.^{27, 232-235} *Operando* studies and isotopic labeling could catch exact changes in catalysts compositions, adsorbed intermediates, and reactant source in CO₂RR. Despite advances in using in-situ X-ray absorption spectroscopy,^{24, 235} infrared spectroscopy,²³⁶ and isotopic labeling²³¹ have been achieved, their use is still limited. We encourage to employ these advanced *in situ* characterization tools to probe CO₂RR mechanisms in future research.

2) Design special morphology for C₂₊ products. Compared to C₁ products, C₂₊ hydrocarbons (e.g. ethylene and propane) and oxygenates (e.g. ethanol, propanol, acetate, acetone) are more valuable due to their high energy density. As highlighted in this Review, morphology engineering can help to C₂₊ generation, such as Cu nanocavity for propanol,¹⁶⁷ ordered mesoporous carbon for ethanol,¹³⁴ and hierarchical Cu dendrites with the superhydrophobic surface for C₂H₄.¹⁵⁶ However, the current performance is still not satisfactory, which urges researchers to design advanced

architected electrodes for target products. Tandem catalysts could be promising models to achieve this goal, in which different morphology can be assembled with special sequence and geometric configuration to facilitate intermediate reactions. For instance, the catalysts with high CO₂-to-CO activity can be coupled with Cu nanocavity to boost the C–C bond formation by feeding more CO at the local Cu surface. Similarly, the catalysts with enhanced capability of hydrogenation and oxygenation can be assembled sequentially with Cu nanocavity to boost the generation of hydrocarbons and oxygenates, respectively.

3) Improve catalyst stability. Besides activity and selectivity, stability is another important descriptor determining the feasibility in practical application. Presently, most of the CO₂RR catalysts cannot maintain their initial activities for more than 200 h (**Table 2**), which is far away from the application requirements (> 1000 h at a high current density of more than 200 mA cm⁻²).³³ The catalyst deactivation mainly originates from the surface reduction/reconstruction, intermediates poisoning, and dissolution/aggregation of active components. Following situations may happen under the harsh CO₂RR condition at negative potentials, including the reduction of positively charged Cu^{δ+} to Cu⁰ in copper-based catalysts,⁹ the reduction of Fe³⁺ to Fe²⁺ in Fe-N/C,²⁴ the decomposition of MOFs/COFs,²²³ the protonation of pyridinic N,²³⁷ and the degradation of organic modifiers. Anchoring the active components on appropriate supports could be a solution to resolve these problems. With enhanced electronic interaction between active components and supports, the chemical states of active components could be retained with improved intrinsic reactivity. Core-shell architecture with active components as the core and stable protecting layer

as the shell could also be promising, in which the shell will not reduce the reactivity of the core catalyst but provide a stabilizing effect to prevent them from being damaged and leached.

4) Multiscale computational modeling. Theoretical computation is a powerful tool to unveil catalytic mechanisms and build efficient catalysts. Currently, DFT computation of CO₂RR mainly relies on the thermodynamic predictions, such as onset potentials, intermediates adsorption, Gibbs free energy. The existing experimental findings demonstrate that electrode topography, pH, and metal ions/solvents types and contents at the electrode-electrolyte interface can considerably impact intermediates distribution and their interaction with electrode surface, as well as mass transportation of intermediates and products. These aspects, however, have been largely overlooked. To gain better insight into CO₂RR from a simulation perspective, future works are encouraged to develop multiscale computation methods, in which the influences of morphology, solvents, and mass transportation can be considered collectively. In addition, electrokinetics modeling is welcomed to study the relationship between reaction current and types/coverage degree of active moieties at varied potentials. The multiscale modeling can help to explain some unusual phenomena (e.g., morphology-dependent selectivity) and offer comprehensive guidance for electrode materials refinements, electrolytes selection, and electrode-solution interface design.

5) Integrate morphological and electronic benefits in one catalyst system. Although the catalysts' electronic structure is not the focus of this Review, it plays very important roles in CO₂RR. Appropriate modification of electronic properties of active components (eg. edge, corner, terraces, interstice, facet, strain, alloying, and doping) could tune CO₂RR activity through adjusting adsorption/desorption of intermediates. Thereby, it is expected that combining

morphology and electronic merits in one system could build advanced catalysts for targeted products. For example, copper selenide has high selectivity for C_1 methanol production due to its favorable adsorption of $*CHO$,¹⁶⁷ and nanocavity morphology can promote C–C coupling.^{156, 167} There is a high chance that constructing copper selenide nanocavity can improve selectivity for C_2 ethanol and C_3 propanol production because it could possess the capability for both the adsorption of $*CHO$ intermediates and $*CO$ – $*CHO$ coupling. Following this idea, there exists a huge room to design unique catalysts for targeted products by combining suitable active components with desirable morphology.

6) Design advanced electrolyzers. In addition to catalysts, whether CO_2 electro-conversion can be successfully commercialized at a large scale depends strongly on the design of advanced reactors that are capable of achieving the high-rate production of pure products with high energy conversion efficiency. While H-type cells in the aqueous media are widely used to investigate catalytic mechanisms, the current density is largely limited by poor solubility CO_2 . GDE-assisted flow cells and fuel cells can efficiently deliver CO_2 to the electrode surface and thus be able to reduce CO_2 at an industrial current. We thus recommend that the CO_2RR performance should be evaluated in flow cells and fuel cells. However, the flooding and clogging of GDL need to be solved for long-term use. Instead of using modifiers that commonly undergo the degradation, constructing morphology-induced hydrophobic GDL could sustain surface hydrophobicity. In addition, designing reactors capable of producing high-purity products with controllable concentrations is urgently needed for the facile and cost-effective operation. The SSE-enabled electrolyzer has shown promises to directly produce high-purity liquids.¹⁷⁵ As compared to liquid

products, the synthesis of high-purity gaseous products is more challenging as the mixture of gas-phase products and unreacted CO₂ cannot be fully avoided. Using a membrane-based separation setup to recycle CO₂ may overcome this issue if the cost can be reduced to an acceptable level.

Conflict of Interests

The authors declare no conflict of interest.

Acknowledgments

This work was supported by the National Science Foundation under Grant No. CMMI-1851674 and the startup grant from the University of Central Florida. F.P. acknowledges the financial support from the Preeminent Postdoctoral Program (P3) at the University of Central Florida.

References

1. O. S. Bushuyev, P. De Luna, C. T. Dinh, L. Tao, G. Saur, J. van de Lagemaat, S. O. Kelley and E. H. Sargent, *Joule*, 2018, **2**, 825-832.
2. P. De Luna, C. Hahn, D. Higgins, S. A. Jaffer, T. F. Jaramillo and E. H. Sargent, *Science*, 2019, **364**, 3506.
3. P. Nugent, Y. Belmabkhout, S. D. Burd, A. J. Cairns, R. Luebke, K. Forrest, T. Pham, S. Ma, B. Space, L. Wojtas, M. Eddaoudi and M. J. Zaworotko, *Nature*, 2013, **495**, 80.
4. Q. Wang, J. Luo, Z. Zhong and A. Borgna, *Energy & Environmental Science*, 2011, **4**, 42-55.
5. X. Duan, J. Xu, Z. W. Seh, J. Ma, S. Guo, S. Wang, H. Liu and S. Dou, *Adv Mater*, 2017, **29**, 1701784.

6. W. Zhang, Q. Qin, L. Dai, R. Qin, X. Zhao, X. Chen, D. Ou, J. Chen, T. T. Chuong, B. Wu and N. Zheng, *Angewandte Chemie International Edition*, 2018, **57**, 9475-9479.
7. M. B. Ross, P. De Luna, Y. Li, C.-T. Dinh, D. Kim, P. Yang and E. H. Sargent, *Nature Catalysis*, 2019, **2**, 648–658.
8. C. Yan, H. Li, Y. Ye, H. Wu, F. Cai, R. Si, J. Xiao, S. Miao, S. Xie, F. Yang, Y. Li, G. Wang and X. Bao, *Energy & Environmental Science*, 2018, **11**, 1204-1210
9. D. Raciti and C. Wang, *ACS Energy Letters*, 2018, **3**, 1545-1556.
10. L. Guo, Z. Yang, K. Marcus, Z. Li, B. Luo, L. Zhou, X. Wang, Y. Du and Y. Yang, *Energy & Environmental Science*, 2018, **11**, 106-114.
11. J. Qiao, Y. Liu, F. Hong and J. Zhang, *Chem Soc Rev*, 2014, **43**, 631-675.
12. M. Aresta, A. Dibenedetto and A. Angelini, *Chem Rev*, 2014, **114**, 1709-1742.
13. M. G. Kibria, J. P. Edwards, C. M. Gabardo, C.-T. Dinh, A. Seifitokaldani, D. Sinton and E. H. Sargent, *Adv Mater*, **31**, 1807166.
14. T. Kåberger, *Global Energy Interconnection*, 2018, **1**, 48-52.
15. A. Hussain, S. M. Arif and M. Aslam, *Renewable and Sustainable Energy Reviews*, 2017, **71**, 12-28.
16. A. A. Peterson, F. Abild-Pedersen, F. Studt, J. Rossmeisl and J. K. Nørskov, *Energy & Environmental Science*, 2010, **3**, 1311-1315.
17. M. Schreier, F. Héroguel, L. Steier, S. Ahmad, J. S. Luterbacher, M. T. Mayer, J. Luo and M. Grätzel, *Nature Energy*, 2017, **2**, 17087.

18. F. Lei, W. Liu, Y. Sun, J. Xu, K. Liu, L. Liang, T. Yao, B. Pan, S. Wei and Y. Xie, *Nature Communications*, 2016, **7**, 12697.
19. N. Han, Y. Wang, H. Yang, J. Deng, J. Wu, Y. Li and Y. Li, *Nature Communications*, 2018, **9**, 1320.
20. J. T. Feaster, C. Shi, E. R. Cave, T. Hatsukade, D. N. Abram, K. P. Kuhl, C. Hahn, J. K. Nørskov and T. F. Jaramillo, *ACS Catalysis*, 2017, **7**, 4822-4827.
21. Y. Chen, C. W. Li and M. W. Kanan, *J Am Chem Soc*, 2012, **134**, 19969-19972.
22. W. Luo, J. Zhang, M. Li and A. Züttel, *ACS Catalysis*, 2019, **9**, 3783-3791.
23. H. B. Yang, S.-F. Hung, S. Liu, K. Yuan, S. Miao, L. Zhang, X. Huang, H.-Y. Wang, W. Cai, R. Chen, J. Gao, X. Yang, W. Chen, Y. Huang, H. M. Chen, C. M. Li, T. Zhang and B. Liu, *Nature Energy*, 2018, **3**, 140-147.
24. J. Gu, C.-S. Hsu, L. Bai, H. M. Chen and X. Hu, *Science*, 2019, **364**, 1091-1094.
25. T. T. H. Hoang, S. Verma, S. Ma, T. T. Fister, J. Timoshenko, A. I. Frenkel, P. J. A. Kenis and A. A. Gewirth, *J Am Chem Soc*, 2018, **140**, 5791-5797.
26. J. Kim, W. Choi, J. W. Park, C. Kim, M. Kim and H. Song, *J Am Chem Soc*, 2019, **141**, 6986-6994.
27. H. Jung, S. Y. Lee, C. W. Lee, M. K. Cho, D. H. Won, C. Kim, H.-S. Oh, B. K. Min and Y. J. Hwang, *J Am Chem Soc*, 2019, **141**, 4624-4633.
28. S. Ma, R. Luo, J. I. Gold, A. Z. Yu, B. Kim and P. J. A. Kenis, *Journal of Materials Chemistry A*, 2016, **4**, 8573-8578.

29. Q. Gong, P. Ding, M. Xu, X. Zhu, M. Wang, J. Deng, Q. Ma, N. Han, Y. Zhu, J. Lu, Z. Feng, Y. Li, W. Zhou and Y. Li, *Nature Communications*, 2019, **10**, 2807.
30. C.-T. Dinh, T. Burdyny, M. G. Kibria, A. Seifitokaldani, C. M. Gabardo, F. P. García de Arquer, A. Kiani, J. P. Edwards, P. De Luna, O. S. Bushuyev, C. Zou, R. Quintero-Bermudez, Y. Pang, D. Sinton and E. H. Sargent, *Science*, 2018, **360**, 783-787.
31. D. Yang, Q. Zhu, C. Chen, H. Liu, Z. Liu, Z. Zhao, X. Zhang, S. Liu and B. Han, *Nature Communications*, 2019, **10**, 677.
32. F. Li, Y. C. Li, Z. Wang, J. Li, D.-H. Nam, Y. Lum, M. Luo, X. Wang, A. Ozden, S.-F. Hung, B. Chen, Y. Wang, J. Wicks, Y. Xu, Y. Li, C. M. Gabardo, C.-T. Dinh, Y. Wang, T.-T. Zhuang, D. Sinton and E. H. Sargent, *Nature Catalysis*, 2020, **3**, 75–82.
33. J. Wu, T. Sharifi, Y. Gao, T. Zhang and P. M. Ajayan, *Adv Mater*, 2019, **31**, 1804257.
34. M. Jouny, W. Luc and F. Jiao, *Ind Eng Chem Res*, 2018, **57**, 2165-2177.
35. Y. Y. Birdja, E. Pérez-Gallent, M. C. Figueiredo, A. J. Göttle, F. Calle-Vallejo and M. T. M. Koper, *Nature Energy*, 2019, **4**, 732–745.
36. Z. W. Seh, J. Kibsgaard, C. F. Dickens, I. Chorkendorff, J. K. Nørskov and T. F. Jaramillo, *Science*, 2017, **355**, 1-12.
37. Y. Wang, P. Han, X. Lv, L. Zhang and G. Zheng, *Joule*, 2018, **2**, 2551-2582.
38. W. Wang, L. Shang, G. Chang, C. Yan, R. Shi, Y. Zhao, G. I. N. Waterhouse, D. Yang and T. Zhang, *Adv Mater*, 2019, **31**, 1808276.

39. Y. Zhou, F. Che, M. Liu, C. Zou, Z. Liang, P. De Luna, H. Yuan, J. Li, Z. Wang, H. Xie, H. Li, P. Chen, E. Bladt, R. Quintero-Bermudez, T.-K. Sham, S. Bals, J. Hofkens, D. Sinton, G. Chen and E. H. Sargent, *Nature Chemistry*, 2018, **10**, 974-980.
40. F. Pan, B. Li, E. Sarnello, S. Hwang, Y. Gang, X. Feng, X. Xiang, N. M. Adli, T. Li, D. Su, G. Wu, G. Wang and Y. Li, *Nano Energy*, 2019, DOI: <https://doi.org/10.1016/j.nanoen.2019.104384>, 104384.
41. F. Pan, Y. Duan, A. Liang, J. Zhang and Y. Li, *Electrochim Acta*, 2017, **238**, 375-383.
42. J. He, K. E. Dettelbach, A. Huang and C. P. Berlinguette, *Angewandte Chemie*, 2017, **129**, 16806-16809.
43. R. P. Jansonius, L. M. Reid, C. N. Virca and C. P. Berlinguette, *ACS Energy Letters*, 2019, **4**, 980-986.
44. E. L. Clark, C. Hahn, T. F. Jaramillo and A. T. Bell, *J Am Chem Soc*, 2017, **139**, 15848-15857.
45. Z. Yin, G. T. R. Palmore and S. Sun, *Trends in Chemistry*, 2019, **1**, 739-750.
46. C. W. Li, J. Ciston and M. W. Kanan, *Nature*, 2014, **508**, 504.
47. R. Chattot, O. Le Bacq, V. Beermann, S. Köhl, J. Herranz, S. Henning, L. Kühn, T. Asset, L. Guétaz, G. Renou, J. Drnec, P. Bordet, A. Pasturel, A. Eychmüller, T. J. Schmidt, P. Strasser, L. Dubau and F. Maillard, *Nature Materials*, 2018, **17**, 827-833.
48. D. Liu, X. Li, S. Chen, H. Yan, C. Wang, C. Wu, Y. A. Haleem, S. Duan, J. Lu, B. Ge, P. M. Ajayan, Y. Luo, J. Jiang and L. Song, *Nature Energy*, 2019, **4**, 512-518.

49. Z. Li, W. Niu, Z. Yang, N. Zaman, W. Samarakoon, M. Wang, A. Kara, M. Lucero, M. V. Vyas, H. Chao, H. Zhou, G. E. Sterbinsky, Z. Feng, Y. Du and Y. Yang, *Energy & Environmental Science*, 2019, **13**, 884-895.
50. H. Hashiba, S. Yotsuhashi, M. Deguchi and Y. Yamada, *ACS Combinatorial Science*, 2016, **18**, 203-208.
51. S. Nitopi, E. Bertheussen, S. B. Scott, X. Liu, A. K. Engstfeld, S. Horch, B. Seger, I. E. L. Stephens, K. Chan, C. Hahn, J. K. Nørskov, T. F. Jaramillo and I. Chorkendorff, *Chem Rev*, 2019, **119**, 7610-7672.
52. L. Wang, W. Chen, D. Zhang, Y. Du, R. Amal, S. Qiao, J. Wu and Z. Yin, *Chem Soc Rev*, 2019, **48**, 5310-5349.
53. Y. Zhu, W. Peng, Y. Li, G. Zhang, F. Zhang and X. Fan, *Small Methods*, 2019, **3**, 1800438.
54. Z. Sun, T. Ma, H. Tao, Q. Fan and B. Han, *Chem*, 2017, **3**, 560-587.
55. S. Lee, D. Kim and J. Lee, *Angewandte Chemie*, 2015, **127**, 14914-14918.
56. G. O. Larrazábal, A. J. Martín, F. Krumeich, R. Hauert and J. Pérez-Ramírez, *ChemSusChem*, 2017, **10**, 1255-1265.
57. S. Popović, M. Smiljanić, P. Jovanović, J. Vavra, R. Buonsanti and N. Hodnik, *Angewandte Chemie International Edition*, 2020, **n/a**.
58. F. Abild-Pedersen, J. Greeley, F. Studt, J. Rossmeisl, T. R. Munter, P. G. Moses, E. Skúlason, T. Bligaard and J. K. Nørskov, *Phys Rev Lett*, 2007, **99**, 016105.
59. X. Liu, J. Xiao, H. Peng, X. Hong, K. Chan and J. K. Nørskov, *Nature Communications*, 2017, **8**, 15438.

60. M. T. M. Koper, *J Electroanal Chem*, 2011, **660**, 254-260.
61. Y.-J. Zhang, V. Sethuraman, R. Michalsky and A. A. Peterson, *ACS Catalysis*, 2014, **4**, 3742-3748.
62. A. Bagger, W. Ju, A. S. Varela, P. Strasser and J. Rossmeisl, *Chemphyschem*, 2017, **18**, 3266-3273.
63. G. Park, S. Hong, M. Choi, S. Lee and J. Lee, *Catal Today*, 2019, DOI: <https://doi.org/10.1016/j.cattod.2019.06.066>.
64. A. S. Hall, Y. Yoon, A. Wuttig and Y. Surendranath, *J Am Chem Soc*, 2015, **137**, 14834-14837.
65. D. M. Weekes, D. A. Salvatore, A. Reyes, A. Huang and C. P. Berlinguette, *Accounts Chem Res*, 2018, **51**, 910-918.
66. Z. Geng, X. Kong, W. Chen, H. Su, Y. Liu, F. Cai, G. Wang and J. Zeng, *Angewandte Chemie International Edition*, 2018, **57**, 6054-6059.
67. T. Zheng, K. Jiang and H. Wang, *Adv Mater*, 2018, **30**, 1802066.
68. D. Gao, R. M. Arán-Ais, H. S. Jeon and B. Roldan Cuenya, *Nature Catalysis*, 2019, **2**, 198-210.
69. B. Kumar, M. Llorente, J. Froehlich, T. Dang, A. Sathrum and C. P. Kubiak, *Annu Rev Phys Chem*, 2012, **63**, 541-569.
70. X. Chang, T. Wang and J. Gong, *Energy & Environmental Science*, 2016, **9**, 2177-2196.
71. C. Song, *Catal Today*, 2006, **115**, 2-32.
72. J.-P. Jones, G. K. S. Prakash and G. A. Olah, *Israel J Chem*, 2014, **54**, 1451-1466.

73. T. Kai, M. Zhou, Z. Duan, G. A. Henkelman and A. J. Bard, *J Am Chem Soc*, 2017, **139**, 18552-18557.
74. B. Kumar, J. P. Brian, V. Atla, S. Kumari, K. A. Bertram, R. T. White and J. M. Spurgeon, *Catal Today*, 2016, **270**, 19-30.
75. Y. Hori, H. Wakebe, T. Tsukamoto and O. Koga, *Electrochim Acta*, 1994, **39**, 1833-1839.
76. H. A. Schwarz and R. W. Dodson, *The Journal of Physical Chemistry*, 1989, **93**, 409-414.
77. D. T. Whipple and P. J. A. Kenis, *The Journal of Physical Chemistry Letters*, 2010, **1**, 3451-3458.
78. B. A. Rosen, A. Salehi-Khojin, M. R. Thorson, W. Zhu, D. T. Whipple, P. J. A. Kenis and R. I. Masel, *Science*, 2011, **334**, 643-644.
79. Y. Matsubara, D. C. Grills and Y. Kuwahara, *ACS Catalysis*, 2015, **5**, 6440-6452.
80. S. N. Habisreutinger, L. Schmidt-Mende and J. K. Stolarczyk, *Angewandte Chemie International Edition*, 2013, **52**, 7372-7408.
81. T. Hatsukade, K. P. Kuhl, E. R. Cave, D. N. Abram and T. F. Jaramillo, *Phys Chem Chem Phys*, 2014, **16**, 13814-13819.
82. J. S. Yoo, R. Christensen, T. Vegge, J. K. Nørskov and F. Studt, *ChemSusChem*, 2016, **9**, 358-363.
83. A. J. Göttle and M. T. M. Koper, *J Am Chem Soc*, 2018, **140**, 4826-4834.
84. N. D. Loewen, T. V. Neelakantan and L. A. Berben, *Accounts Chem Res*, 2017, **50**, 2362-2370.
85. X. Min and M. W. Kanan, *J Am Chem Soc*, 2015, **137**, 4701-4708.

86. M. C. Groenenboom and J. A. Keith, *Chemphyschem*, 2017, **18**, 3090-3090.
87. A. J. Bard and L. R. Faulkner, 2001, **2nd ed.**, 100.
88. D. D. Zhu, J. L. Liu and S. Z. Qiao, *Adv Mater*, 2016, **28**, 3423-3452.
89. H. A. Hansen, C. Shi, A. C. Lausche, A. A. Peterson and J. K. Nørskov, *Phys Chem Chem Phys*, 2016, **18**, 9194-9201.
90. A. Vasileff, C. Xu, Y. Jiao, Y. Zheng and S.-Z. Qiao, *Chem*, 2018, **4**, 1809-1831.
91. C. W. Li, J. Ciston and M. W. Kanan, *Nature*, 2014, **508**, 504-507.
92. M. Jouny, W. Luc and F. Jiao, *Nature Catalysis*, 2018, **1**, 748-755.
93. J. Li, K. Chang, H. Zhang, M. He, W. A. Goddard, J. G. Chen, M.-J. Cheng and Q. Lu, *ACS Catalysis*, 2019, **9**, 4709-4718.
94. M. Asadi, K. Kim, C. Liu, A. V. Addepalli, P. Abbasi, P. Yasaei, P. Phillips, A. Behranginia, J. M. Cerrato, R. Haasch, P. Zapol, B. Kumar, R. F. Klie, J. Abiade, L. A. Curtiss and A. Salehi-Khojin, *Science*, 2016, **353**, 467-470.
95. N. Gupta, M. Gattrell and B. MacDougall, *J Appl Electrochem*, 2006, **36**, 161-172.
96. M. R. Singh, J. D. Goodpaster, A. Z. Weber, M. Head-Gordon and A. T. Bell, *Proceedings of the National Academy of Sciences*, 2017, **114**, E8812-E8821.
97. J. Rosen, G. S. Hutchings, Q. Lu, S. Rivera, Y. Zhou, D. G. Vlachos and F. Jiao, *ACS Catalysis*, 2015, **5**, 4293-4299.
98. Q. Lu, J. Rosen, Y. Zhou, G. S. Hutchings, Y. C. Kimmel, J. G. Chen and F. Jiao, *Nat. Commun.*, 2014, **5**, 3242.

99. M. Liu, Y. Pang, B. Zhang, P. De Luna, O. Voznyy, J. Xu, X. Zheng, C. T. Dinh, F. Fan, C. Cao, F. P. G. de Arquer, T. S. Safaei, A. Mepham, A. Klinkova, E. Kumacheva, T. Filleter, D. Sinton, S. O. Kelley and E. H. Sargent, *Nature*, 2016, **537**, 382.
100. N. Dubouis and A. Grimaud, *Chemical Science*, 2019, **10**, 9165-9181.
101. Q. Lu and F. Jiao, *Nano Energy*, 2016, **29**, 439-456.
102. X. Li, W. Bi, M. Chen, Y. Sun, H. Ju, W. Yan, J. Zhu, X. Wu, W. Chu, C. Wu and Y. Xie, *J Am Chem Soc*, 2017, **139**, 14889-14892.
103. F. Pan, H. Zhang, K. Liu, D. A. Cullen, K. L. More, M. Wang, Z. Feng, G. Wang, G. Wu and Y. Li, *ACS Catalysis*, 2018, **8**, 3116-3122.
104. T. Shinagawa, A. T. Garcia-Esparza and K. Takanebe, *Scientific Reports*, 2015, **5**, 13801.
105. K. Jiang, S. Siahrostami, A. J. Akey, Y. Li, Z. Lu, J. Lattimer, Y. Hu, C. Stokes, M. Gangishetty, G. Chen, Y. Zhou, W. Hill, W.-B. Cai, D. Bell, K. Chan, J. K. Nørskov, Y. Cui and H. Wang, *Chem*, 2017, **3**, 950-960.
106. F. Pan, W. Deng, C. Justiniano and Y. Li, *Appl. Catal. B: Environ.*, 2018, **226**, 463-472.
107. W. Ju, A. Bagger, G.-P. Hao, A. S. Varela, I. Sinev, V. Bon, B. Roldan Cuenya, S. Kaskel, J. Rossmeisl and P. Strasser, *Nature Communications*, 2017, **8**, 944.
108. X. Feng, K. Jiang, S. Fan and M. W. Kanan, *J Am Chem Soc*, 2015, **137**, 4606-4609.
109. R. G. Mariano, K. McKelvey, H. S. White and M. W. Kanan, *Science*, 2017, **358**, 1187-1192.
110. Y. Song, S. Wang, W. Chen, S. Li, G. Feng, W. Wei and Y. Sun, *ChemSusChem*, 2020, **13**, 293-297.

111. K. U. D. Calvinho, A. B. Laursen, K. M. K. Yap, T. A. Goetjen, S. Hwang, N. Murali, B. Mejia-Sosa, A. Lubarski, K. M. Teeluck, E. S. Hall, E. Garfunkel, M. Greenblatt and G. C. Dismukes, *Energy & Environmental Science*, 2018, **11**, 2550-2559.
112. S. A. Francis, J. M. Velazquez, I. M. Ferrer, D. A. Torelli, D. Guevarra, M. T. McDowell, K. Sun, X. Zhou, F. H. Saadi, J. John, M. H. Richter, F. P. Hyler, K. M. Papadantonakis, B. S. Brunshwig and N. S. Lewis, *Chem Mater*, 2018, **30**, 4902-4908.
113. M. Rahaman, A. Dutta, A. Zanetti and P. Broekmann, *ACS Catalysis*, 2017, **7**, 7946-7956.
114. J. B. Greenblatt, D. J. Miller, J. W. Ager, F. A. Houle and I. D. Sharp, *Joule*, 2018, **2**, 381-420.
115. M. Naghsh, M. Sadeghi, A. Moheb, M. P. Chenar and M. Mohagheghian, *J Membrane Sci*, 2012, **423-424**, 97-106.
116. H. Li, K. Wang, Y. Sun, C. T. Lollar, J. Li and H.-C. Zhou, *Materials Today*, 2018, **21**, 108-121.
117. C.-H. Lim, A. M. Holder, J. T. Hynes and C. B. Musgrave, *J Am Chem Soc*, 2014, **136**, 16081-16095.
118. K. P. Kuhl, T. Hatsukade, E. R. Cave, D. N. Abram, J. Kibsgaard and T. F. Jaramillo, *J Am Chem Soc*, 2014, **136**, 14107-14113.
119. D. H. Won, H. Shin, J. Koh, J. Chung, H. S. Lee, H. Kim and S. I. Woo, *Angewandte Chemie International Edition*, 2016, **55**, 9297-9300.

120. X. Wang, Z. Chen, X. Zhao, T. Yao, W. Chen, R. You, C. Zhao, G. Wu, J. Wang, W. Huang, J. Yang, X. Hong, S. Wei, Y. Wu and Y. Li, *Angewandte Chemie International Edition*, 2018, **57**, 1944-1948.
121. F. Pan, H. Zhao, W. Deng, X. Feng and Y. Li, *Electrochim Acta*, 2018, **273**, 154-161.
122. X. Zheng, P. De Luna, F. P. García de Arquer, B. Zhang, N. Becknell, M. B. Ross, Y. Li, M. N. Banis, Y. Li, M. Liu, O. Voznyy, C. T. Dinh, T. Zhuang, P. Stadler, Y. Cui, X. Du, P. Yang and E. H. Sargent, *Joule*, 2017, **1**, 794-805.
123. X. Zheng, Y. Ji, J. Tang, J. Wang, B. Liu, H.-G. Steinrück, K. Lim, Y. Li, M. F. Toney, K. Chan and Y. Cui, *Nature Catalysis*, 2019, **2**, 55-61.
124. S. Gao, Y. Lin, X. Jiao, Y. Sun, Q. Luo, W. Zhang, D. Li, J. Yang and Y. Xie, *Nature*, 2016, **529**, 68-71.
125. S. Gao, X. Jiao, Z. Sun, W. Zhang, Y. Sun, C. Wang, Q. Hu, X. Zu, F. Yang, S. Yang, L. Liang, J. Wu and Y. Xie, *Angewandte Chemie International Edition*, 2015, **128**, 708-712.
126. J. Hazarika and M. S. Manna, *Electrochim Acta*, 2019, **328**, 135053.
127. X. Sun, *Angewandte Chemie International Edition*, 2020, **7**, 758-762.
128. Y. Wu, Z. Jiang, X. Lu, Y. Liang and H. Wang, *Nature*, 2019, **575**, 639-642.
129. Y. Peng, T. Wu, L. Sun, J. M. V. Nsanzimana, A. C. Fisher and X. Wang, *ACS Applied Materials & Interfaces*, 2017, **9**, 32782-32789.
130. H. Mistry, A. S. Varela, C. S. Bonifacio, I. Zegkinoglou, I. Sinev, Y.-W. Choi, K. Kisslinger, E. A. Stach, J. C. Yang, P. Strasser and B. R. Cuenya, *Nature Communications*, 2016, **7**, 12123.

131. Z. Yin, C. Yu, Z. Zhao, X. Guo, M. Shen, N. Li, M. Muzzio, J. Li, H. Liu, H. Lin, J. Yin, G. Lu, D. Su and S. Sun, *Nano Letters*, 2019, **12**, 8658-8663.
132. K. P. Kuhl, E. R. Cave, D. N. Abram and T. F. Jaramillo, *Energy & Environmental Science*, 2012, **5**, 7050-7059.
133. D. Ren, Y. Deng, A. D. Handoko, C. S. Chen, S. Malkhandi and B. S. Yeo, *ACS Catalysis*, 2015, **5**, 2814-2821.
134. Y. Song, W. Chen, C. Zhao, S. Li, W. Wei and Y. Sun, *Angewandte Chemie International Edition*, 2017, **56**, 10840.
135. J. Li, G. Chen, Y. Zhu, Z. Liang, A. Pei, C.-L. Wu, H. Wang, H. R. Lee, K. Liu, S. Chu and Y. Cui, *Nature Catalysis*, 2018, **1**, 592–600.
136. Y. Yoon, A. S. Hall and Y. Surendranath, *Angewandte Chemie International Edition*, 2016, **55**, 15282-15286.
137. F. Pan, B. Li, X. Xiang, G. Wang and Y. Li, *ACS Catalysis*, 2019, **9**, 2124-2133.
138. D. Hursán, A. A. Samu, L. Janovák, K. Artyushkova, T. Asset, P. Atanassov and C. Janáky, *Joule*, 2019, **3**, 1719-1733.
139. W. Ni, Y. Xue, X. Zang, C. Li, H. Wang, Z. Yang and Y.-M. Yan, *ACS Nano*, 2020, **14**, 2014-2023.
140. C. Zhao, Y. Wang, Z. Li, W. Chen, Q. Xu, D. He, D. Xi, Q. Zhang, T. Yuan, Y. Qu, J. Yang, F. Zhou, Z. Yang, X. Wang, J. Wang, J. Luo, Y. Li, H. Duan, Y. Wu and Y. Li, *Joule*, 2018, **3**, 584-594.

141. A. K. Buckley, M. Lee, T. Cheng, R. V. Kazantsev, D. M. Larson, W. A. Goddard III, F. D. Toste and F. M. Toma, *J Am Chem Soc*, 2019, **141**, 7355-7364.
142. S. Verma, Y. Hamasaki, C. Kim, W. Huang, S. Lu, H.-R. M. Jhong, A. A. Gewirth, T. Fujigaya, N. Nakashima and P. J. A. Kenis, *ACS Energy Letters*, 2018, **3**, 193-198.
143. T. Zheng, K. Jiang, N. Ta, Y. Hu, J. Zeng, J. Liu and H. Wang, *Joule*, 2019, **3**, 265-278.
144. S. Ren, D. Joulié, D. Salvatore, K. Torbensen, M. Wang, M. Robert and C. P. Berlinguette, *Science*, 2019, **365**, 367-369.
145. N. Han, Y. Wang, J. Deng, J. Zhou, Y. Wu, H. Yang, P. Ding and Y. Li, *Journal of Materials Chemistry A*, 2019, **7**, 1267-1272.
146. L. Wonhee, K. Y. Eun, Y. M. Hye, J. S. Kwan and P. K. Tae, *Angewandte Chemie International Edition*, 2018, **57**, 6883-6887.
147. A. Dutta, M. Rahaman, N. C. Luedi, M. Mohos and P. Broekmann, *ACS Catalysis*, 2016, **6**, 3804-3814.
148. J.-J. Lv, M. Jouny, W. Luc, W. Zhu, J.-J. Zhu and F. Jiao, *Adv Mater*, 2018, **30**, 1803111.
149. Y. Xu, J. P. Edwards, J. Zhong, C. P. O'Brien, C. M. Gabardo, C. McCallum, J. Li, C.-T. Dinh, E. H. Sargent and D. Sinton, *Energy & Environmental Science*, 2020, **13**, 554-561.
150. C. M. Gabardo, C. P. O'Brien, J. P. Edwards, C. McCallum, Y. Xu, C.-T. Dinh, J. Li, E. H. Sargent and D. Sinton, *Joule*, 2019, **3**, 2777-2791.
151. J. Wu, S. Ma, J. Sun, J. I. Gold, C. Tiwary, B. Kim, L. Zhu, N. Chopra, I. N. Odeh, R. Vajtai, A. Z. Yu, R. Luo, J. Lou, G. Ding, P. J. A. Kenis and P. M. Ajayan, *Nature Communications*, 2016, **7**, 13869.

152. J. Choi, J. Kim, P. Wagner, S. Gambhir, R. Jalili, S. Byun, S. Sayyar, Y. M. Lee, D. R. MacFarlane, G. G. Wallace and D. L. Officer, *Energy & Environmental Science*, 2019, **12**, 747-755
153. D. Higgins, C. Hahn, C. Xiang, T. F. Jaramillo and A. Z. Weber, *ACS Energy Letters*, 2019, **4**, 317-324.
154. M. R. Singh, Y. Kwon, Y. Lum, J. W. Ager and A. T. Bell, *J Am Chem Soc*, 2016, **138**, 13006-13012.
155. M. E. Casco, M. Martínez-Escandell, J. Silvestre-Albero and F. Rodríguez-Reinoso, *Carbon*, 2014, **67**, 230-235.
156. D. Wakerley, S. Lamaison, F. Ozanam, N. Menguy, D. Mercier, P. Marcus, M. Fontecave and V. Mougel, *Nature Materials*, 2019, **18**, 1222-1227.
157. T. Burdyny and W. A. Smith, *Energy & Environmental Science*, 2019, **12**, 1442-1453.
158. K. Liu, W. A. Smith and T. Burdyny, *ACS Energy Letters*, 2019, **4**, 639-643.
159. X. Wang, J. F. de Araújo, W. Ju, A. Bagger, H. Schmies, S. Köhl, J. Rossmeisl and P. Strasser, *Nature Nanotechnology*, 2019, **14**, 1-8.
160. H. Yang, Q. Lin, Y. Wu, G. Li, Q. Hu, X. Chai, X. Ren, Q. Zhang, J. Liu and C. He, *Nano Energy*, 2020, **70**, 104454.
161. T.-N. Ye, L.-B. Lv, X.-H. Li, M. Xu and J.-S. Chen, *Angewandte Chemie*, 2014, **126**, 7025-7029.
162. Y. Hori, A. Murata and R. Takahashi, *Journal of the Chemical Society, Faraday Transactions 1: Physical Chemistry in Condensed Phases*, 1989, **85**, 2309-2326.

163. R. Kas, R. Kortlever, H. Yilmaz, M. T. M. Koper and G. Mul, *ChemElectroChem*, 2015, **2**, 354-358.
164. K. J. P. Schouten, Z. Qin, E. Pérez Gallent and M. T. M. Koper, *J Am Chem Soc*, 2012, **134**, 9864-9867.
165. T. Burdyny, P. J. Graham, Y. Pang, C.-T. Dinh, M. Liu, E. H. Sargent and D. Sinton, *ACS Sustainable Chemistry & Engineering*, 2017, **5**, 4031-4040.
166. Y. Li and P. Yang, *Nature Nanotechnology*, 2019, **11**, 1002-1003.
167. T.-T. Zhuang, Y. Pang, Z.-Q. Liang, Z. Wang, Y. Li, C.-S. Tan, J. Li, C. T. Dinh, P. De Luna, P.-L. Hsieh, T. Burdyny, H.-H. Li, M. Liu, Y. Wang, F. Li, A. Proppe, A. Johnston, D.-H. Nam, Z.-Y. Wu, Y.-R. Zheng, A. H. Ip, H. Tan, L.-J. Chen, S.-H. Yu, S. O. Kelley, D. Sinton and E. H. Sargent, *Nature Catalysis*, 2018, **1**, 946-951.
168. S. Yuan, J.-L. Shui, L. Grabstanowicz, C. Chen, S. Commet, B. Reprögle, T. Xu, L. Yu and D.-J. Liu, *Angewandte Chemie*, 2013, **125**, 8507-8511.
169. W. Bi, C. Wu and Y. Xie, *ACS Energy Letters*, 2018, **3**, 624-633.
170. H. Yang, Q. Lin, C. Zhang, X. Yu, Z. Cheng, G. Li, Q. Hu, X. Ren, Q. Zhang, J. Liu and C. He, *Nature Communications*, 2020, **11**, 593.
171. F. Li, L. Chen, G. P. Knowles, D. R. MacFarlane and J. Zhang, *Angewandte Chemie International Edition*, 2017, **56**, 505.
172. Y. Y. Birdja and M. T. M. Koper, *J Am Chem Soc*, 2017, **139**, 2030-2034.
173. V. R. Stamenkovic, D. Strmcnik, P. P. Lopes and N. M. Markovic, *Nat Mater*, 2017, **16**, 57-69.

174. S. Lee, H. Ju, R. Machunda, S. Uhm, J. K. Lee, H. J. Lee and J. Lee, *Journal of Materials Chemistry A*, 2015, **3**, 3029-3034.
175. C. Xia, P. Zhu, Q. Jiang, Y. Pan, W. Liang, E. Stavitsk, H. N. Alshareef and H. Wang, *Nature Energy*, 2019, **4**, 776–785.
176. C. Xia, Y. Xia, P. Zhu, L. Fan and H. Wang, *Science*, 2019, **366**, 226-231.
177. Y. C. Li, D. Zhou, Z. Yan, R. H. Gonçalves, D. A. Salvatore, C. P. Berlinguette and T. E. Mallouk, *ACS Energy Letters*, 2016, **1**, 1149-1153.
178. G. O. Larrazábal, P. Strøm-Hansen, J. P. Heli, K. Zeiter, K. T. Therkildsen, I. Chorkendorff and B. Seger, *ACS Applied Materials & Interfaces*, 2019, **11**, 41281-41288.
179. M. Ma, E. L. Clark, S. Dalsgaard, K. T. Therkildsen, I. Chorkendorff and B. J. Seger, *Energy & Environmental Science*, 2020, **13**, 977-985.
180. T. Cheng, L. Wang, B. V. Merinov and W. A. Goddard, *J Am Chem Soc*, 2018, **140**, 7787-7790.
181. T. Cheng, H. Xiao and W. A. Goddard, *J Am Chem Soc*, 2016, **138**, 13802-13805.
182. R. Kortlever, J. Shen, K. J. P. Schouten, F. Calle-Vallejo and M. T. M. Koper, *The Journal of Physical Chemistry Letters*, 2015, **6**, 4073-4082.
183. R. F. Service, *Science*, 2016, **354**, 1362-1363.
184. M. E. Boot-Handford, J. C. Abanades, E. J. Anthony, M. J. Blunt, S. Brandani, N. Mac Dowell, J. R. Fernández, M.-C. Ferrari, R. Gross, J. P. Hallett, R. S. Haszeldine, P. Heptonstall, A. Lyngfelt, Z. Makuch, E. Mangano, R. T. J. Porter, M. Pourkashanian, G.

- T. Rochelle, N. Shah, J. G. Yao and P. S. Fennell, *Energy & Environmental Science*, 2014, **7**, 130-189.
185. W. Luc, B. H. Ko, S. Kattel, S. Li, D. Su, J. G. Chen and F. Jiao, *J Am Chem Soc*, 2019, **141**, 9902-9909.
186. L.-P. Yang, J.-L. Mi, J.-H. Liang, Z.-Y. Zu and P. Zhang, *ACS Applied Energy Materials*, 2019, **2**, 6295-6301.
187. S. Zhang, P. Kang, S. Ubnoske, M. K. Brennaman, N. Song, R. L. House, J. T. Glass and T. J. Meyer, *J Am Chem Soc*, 2014, **136**, 7845-7848.
188. F. Pan, B. Li, W. Deng, Z. Du, Y. Gang, G. Wang and Y. Li, *Applied Catalysis B: Environmental*, 2019, **252**, 240-249.
189. X. Jiafang, Z. Xiaotao, W. Maoxiang, L. Qiaohong, W. Yaobing and Y. Jiannian, *Angewandte Chemie International Edition*, 2018, **57**, 1-6.
190. H. Mistry, F. Behafarid, R. Reske, A. S. Varela, P. Strasser and B. Roldan Cuenya, *ACS Catalysis*, 2016, **6**, 1075-1080.
191. S. S. Lathe, C. Terashima, K. Nakata and A. Fujishima, *Molecules*, 2014, **19**, 4256-4283.
192. J.-M. Lim, G.-R. Yi, J. H. Moon, C.-J. Heo and S.-M. Yang, *Langmuir*, 2007, **23**, 7981-7989.
193. R. Kas, K. K. Hummadi, R. Kortlever, P. de Wit, A. Milbrat, M. W. J. Luiten-Olieman, N. E. Benes, M. T. M. Koper and G. Mul, *Nat Commun*, 2016, **7**, 10748.
194. D. Raciti, M. Mao and C. Wang, *Nanotechnology*, 2017, **29**, 044001.
195. A. S. Varela, M. Kroschel, T. Reier and P. Strasser, *Catal Today*, 2016, **260**, 8-13.

196. B. Kokoszka, N. K. Jarrah, C. Liu, D. T. Moore and K. Landskron, *Angewandte Chemie International Edition*, 2014, **53**, 3698-3701.
197. M. Ma, K. Djanashvili and W. A. Smith, *Angewandte Chemie International Edition*, 2016, **55**, 6680-6684.
198. F. Pan, A. Liang, Y. Duan, Q. Liu, J. Zhang and Y. Li, *J. Mater. Chem. A* 2017, **5**, 13104-13111.
199. J. Liu, N. P. Wickramaratne, S. Z. Qiao and M. Jaroniec, *Nat Mater*, 2015, **14**, 763-774.
200. S. Chen and S.-Z. Qiao, *ACS Nano*, 2013, **7**, 10190-10196.
201. P. P. Sharma, J. Wu, R. M. Yadav, M. Liu, C. J. Wright, C. S. Tiwary, B. I. Yakobson, J. Lou, P. M. Ajayan and X.-D. Zhou, *Angewandte Chemie International Edition*, 2015, **54**, 13701-13705.
202. X. Cui, Z. Pan, L. Zhang, H. Peng and G. Zheng, *Advanced Energy Materials*, 2017, **7**, 1701456.
203. J. Wu, R. M. Yadav, M. Liu, P. P. Sharma, C. S. Tiwary, L. Ma, X. Zou, X.-D. Zhou, B. I. Yakobson, J. Lou and P. M. Ajayan, *ACS Nano*, 2015, **9**, 5364-5371.
204. D. Dutta, B. C. Wood, S. Y. Bhide, K. G. Ayappa and S. Narasimhan, *The Journal of Physical Chemistry C*, 2014, **118**, 7741-7750.
205. H. Wang, Y. Chen, X. Hou, C. Ma and T. Tan, *Green Chem*, 2016, **18**, 3250-3256.
206. J. Wu, M. Liu, P. P. Sharma, R. M. Yadav, L. Ma, Y. Yang, X. Zou, X.-D. Zhou, R. Vajtai, B. I. Yakobson, J. Lou and P. M. Ajayan, *Nano Lett.*, 2016, **16**, 466-470.

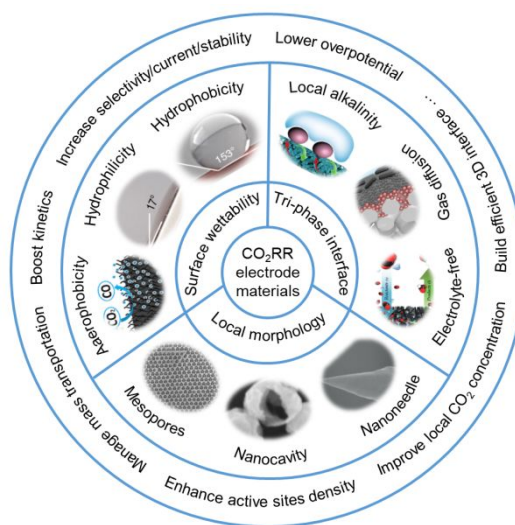
207. J. Xu, Y. Kan, R. Huang, B. Zhang, B. Wang, K.-H. Wu, Y. Lin, X. Sun, Q. Li, G. Centi and D. Su, *ChemSusChem*, 2016, **9**, 1085-1089.
208. B. Kumar, V. Atla, J. P. Brian, S. Kumari, T. Q. Nguyen, M. Sunkara and J. M. Spurgeon, *Angewandte Chemie International Edition*, 2017, **56**, 3645-3649.
209. W. Zhang, H. Lin, Z. Lin, J. Yin, H. Lu, D. Liu and M. Zhao, *ChemSusChem*, 2015, **8**, 2114-2122.
210. H.-W. Liang, X. Zhuang, S. Brüller, X. Feng and K. Müllen, *Nat Commun*, 2014, **5**, 4973.
211. F. Pan, B. Li, E. Sarnello, Y. Fei, Y. Gang, X. Xiang, Z. Du, P. Zhang, G. Wang, H. T. Nguyen, T. Li, Y. H. Hu, H.-C. Zhou and Y. Li, *ACS Nano*, 2020, DOI: 10.1021/acsnano.9b09658.
212. K. Geng, T. He, R. Liu, S. Dalapati, K. T. Tan, Z. Li, S. Tao, Y. Gong, Q. Jiang and D. Jiang, *Chem Rev*, 2020, DOI: 10.1021/acs.chemrev.9b00550.
213. L. Zhu, X.-Q. Liu, H.-L. Jiang and L.-B. Sun, *Chem Rev*, 2017, **117**, 8129-8176.
214. S. Lin, C. S. Diercks, Y.-B. Zhang, N. Kornienko, E. M. Nichols, Y. Zhao, A. R. Paris, D. Kim, P. Yang, O. M. Yaghi and C. J. Chang, *Science*, 2015, **349**, 1208-1213.
215. N. Kornienko, Y. Zhao, C. S. Kley, C. Zhu, D. Kim, S. Lin, C. J. Chang, O. M. Yaghi and P. Yang, *J Am Chem Soc*, 2015, **137**, 14129-14135.
216. X. Jiang, H. Li, J. Xiao, D. Gao, R. Si, F. Yang, Y. Li, G. Wang and X. Bao, *Nano Energy*, 2018, **52**, 345-350.
217. C. S. Diercks, Y. Liu, K. E. Cordova and O. M. Yaghi, *Nature Materials*, 2018, **17**, 301-307.

218. H.-J. Zhu, M. Lu, Y.-R. Wang, S.-J. Yao, M. Zhang, Y.-H. Kan, J. Liu, Y. Chen, S.-L. Li and Y.-Q. Lan, *Nature Communications*, 2020, **11**, 497.
219. H. Zhong, M. Ghorbani-Asl, K. H. Ly, J. Zhang, J. Ge, M. Wang, Z. Liao, D. Makarov, E. Zschech, E. Brunner, I. M. Weidinger, J. Zhang, A. V. Krashennnikov, S. Kaskel, R. Dong and X. Feng, *Nature Communications*, 2020, **11**, 1409.
220. C. S. Diercks, S. Lin, N. Kornienko, E. A. Kapustin, E. M. Nichols, C. Zhu, Y. Zhao, C. J. Chang and O. M. Yaghi, *J Am Chem Soc*, 2018, **140**, 1116-1122.
221. H. Liu, J. Chu, Z. Yin, X. Cai, L. Zhuang and H. Deng, *Chem*, 2018, **4**, 1696-1709.
222. R.-B. Lin and B. Chen, *Joule*, 2018, **2**, 1030-1032.
223. Y. Zhang, X. Zhang, Y. Zhu, B. Qian, A. M. Bond and J. Zhang, *ChemSusChem*, 2020, **n/a**.
224. L. Feng, K.-Y. Wang, X.-L. Lv, T.-H. Yan and H.-C. Zhou, *National Science Review*, 2019.
225. J.-X. Wu, S.-Z. Hou, X.-D. Zhang, M. Xu, H.-F. Yang, P.-S. Cao and Z.-Y. Gu, *Chemical Science*, 2019, **10**, 2199-2205.
226. D.-H. Nam, O. S. Bushuyev, J. Li, P. De Luna, A. Seifitokaldani, C.-T. Dinh, F. P. García de Arquer, Y. Wang, Z. Liang, A. H. Proppe, C. S. Tan, P. Todorović, O. Shekhah, C. M. Gabardo, J. W. Jo, J. Choi, M.-J. Choi, S.-W. Baek, J. Kim, D. Sinton, S. O. Kelley, M. Eddaoudi and E. H. Sargent, *J Am Chem Soc*, 2018, **140**, 11378-11386.
227. S. Sen, D. Liu and G. T. R. Palmore, *ACS Catalysis*, 2014, **4**, 3091-3095.
228. S. Suter and S. Haussener, *Energy & Environmental Science*, 2019, **12**, 1668.

229. S. Verma, X. Lu, S. Ma, R. I. Masel and P. J. A. Kenis, *Phys Chem Chem Phys*, 2016, **18**, 7075-7084.
230. Y. C. Li, G. Lee, T. Yuan, Y. Wang, D.-H. Nam, Z. Wang, F. P. García de Arquer, Y. Lum, C.-T. Dinh, O. Voznyy and E. H. Sargent, *ACS Energy Letters*, 2019, **4**, 1427-1431.
231. D. Hursán and C. Janáky, *ACS Energy Letters*, 2018, **3**, 722-723.
232. H. Jung, S. Y. Lee, C. W. Lee, M. K. Cho, D. H. Won, C. Kim, H.-S. Oh, B. K. Min and Y. J. Hwang, *J Am Chem Soc*, 2019, **141**, 4624-4633.
233. Y.-G. Kim, J. H. Baricuatro and M. P. Soriaga, *Electrocatalysis*, 2018, **9**, 526-530.
234. Z. Weng, Y. Wu, M. Wang, J. Jiang, K. Yang, S. Huo, X.-F. Wang, Q. Ma, G. W. Brudvig, V. S. Batista, Y. Liang, Z. Feng and H. Wang, *Nature Communications*, 2018, **9**, 415.
235. D. Karapinar, N. T. Huan, N. Ranjbar Sahraie, J. Li, D. Wakerley, N. Touati, S. Zanna, D. Taverna, L. H. Galvão Tizei, A. Zitolo, F. Jaouen, V. Mougel and M. Fontecave, *Angewandte Chemie International Edition*, 2019, **58**, 15098-15103.
236. S. Zhu, T. Li, W.-B. Cai and M. Shao, *ACS Energy Letters*, 2019, **4**, 682-689.
237. J. Jin, X. Fu, Q. Liu, Y. Liu, Z. Wei, K. Niu and J. Zhang, *ACS Nano*, 2013, **7**, 4764-4773.

Broader context

Producing value-added fuels and chemicals from CO₂ using electrochemical approaches is a promising way to recycle greenhouse gas and mitigate the dependence on fossil fuels. However, scaling up this technology to industry-level faces grand challenges due to the lack of highly active, stable, and cost-effective electrocatalysts for CO₂ reduction reaction (CO₂RR). While engineering the electronic structure of catalysts to tune CO₂RR behaviors has been investigated for decades, the linear scaling relation of the adsorption with multiple intermediates limits its applicability in regulating CO₂RR for generating desired products. Thanks to the high dependence of CO₂RR on the local environment and mass transportation near the gas-solid-liquid interface, modulating morphology and interface properties present an effective strategy to regulate CO₂ reduction. These modifications are not only insusceptible to linear scaling relation but also possess high resistance to the harsh reaction condition, showing great promises to achieve high-efficiency CO₂ conversion. In this Review, we summarize the most recent achievements in tuning CO₂RR through engineering electrode catalysts' morphology, surface wettability, three-phase interface. We provide the design principles and review typical approaches to fabricate engineered electrodes. Particularly, we discuss the relationship between electrode properties and CO₂RR performance to gain insight into the activity-governing parameters and catalytic mechanisms. Finally, we propose strategies to guide the further design of advanced electrode materials. We hope that this Review could gain the researcher's attention on this emerging direction and inspire more innovative strategies to propel the practical implementation of CO₂ electro-conversion.

Table of Contents Entry

This review discusses how morphology and interface engineering promote electrocatalytic CO₂ reduction, providing general design principles to fabricate advanced electrode catalysts.